Hydrodynamic analogues of quantum corrals and Friedel oscillations

by

Tudor Cristea-Platon

Submitted to the Department of Mathematics
in partial fulfillment of the requirements for the degree of

Doctor of Philosophy in Mathematics

at the

MASSACHUSETTS INSTITUTE OF TECHNOLOGY

June 2019

Signature redacted

Author .....
Department of Mathematics
May 3, 2019

Signature redacted

Certified by .....
John W. M. Bush
Professor of Applied Mathematics
Thesis Supervisor

Signature redacted

Accepted by .....
Jonathan Kelner
Chairman, Department Committee on Graduate Theses

Hydrodynamic analogues of quantum corrals and Friedel oscillations

by

Tudor Cristea-Platon

Submitted to the Department of Mathematics
on May 3, 2019, in partial fulfillment of the
requirements for the degree of
Doctor of Philosophy in Mathematics

Abstract

We consider the walking droplet (or 'walker') system discovered in 2005 by Yves Couder and coworkers. We investigate experimentally and theoretically the behaviour of this hydrodynamic pilot-wave system in both closed and open geometries. First, we consider the dynamics and statistics of walkers confined to corrals. In the elliptical corral, we demonstrate that by introducing a submerged topographical defect, one can create statistical projection effects analogous to the quantum mirage effect arising in quantum corrals. We also report a link between the droplet's statistics and the mean wave field. In the circular corral, we investigate a parameter regime marked by periodic and weakly aperiodic orbits, then characterise the emergence and breakdown of double quantisation, reminiscent of that arising for walker motion in a harmonic potential. In the chaotic regime, we test the theoretical result of Durey et al. relating the walker statistics to the mean wave-field. We also rationalise the striking similarity between this mean wave-field and the circular corral's dominant azimuthally-symmetric Faraday mode. Our corral studies underscore the compatibly of the notion of quantum eigenstates and particle trajectories in closed geometries. We proceed by exploring a new hydrodynamic quantum analogue of the Friedel oscillations arising when a walker interacts with a submerged circular well, which acts as a localised region of high excitability. In so doing, we report the first successful realisation of an open hydrodynamic quantum analogue. We conclude by comparing the hydrodynamic systems to their quantum counterparts. Our work illustrates how, in the closed and open settings considered herein, a pilot-wave dynamics of the form envisaged by de Broglie may lead naturally to emergent statistics similar in form to those predicted by standard quantum mechanics.

Thesis Supervisor: John W. M. Bush
Title: Professor of Applied Mathematics

Acknowledgments

I would like to thank my Pam for always supporting me throughout my graduate studies and for always showing me patience and understanding. I would like to thank my family for all their constant help and love. I would like to thank Professor Bush for his professional mentorship and Professor Rosales for his personal guidance. Finally, I would like to thank Professor Sáenz for his behind-the-scenes kindness and for always putting in the good word.

Contents

List of Figures

A-16 Walker dynamics in the vicinity of a circular well. **(a)** Oblique view of a walking drop self-propelling above a submerged circular well (dashed line). Supplementary Movie 1. **(b)** Top view of the experimental setup. A submerged well of diameter $D = 13 \pm 0.1$ mm is located at the centre of a circular liquid bath vibrated vertically at frequency $f = 70$ Hz and maximum acceleration $\gamma/\gamma_F = 0.990 \pm 0.002$. The corner geometry serves to automatically redirect the walker towards the well. **(c)** Schematic cross section. The submerged well of depth $H = 6.2 \pm 0.03$ mm is located at the bottom of a relatively shallow liquid layer of depth $h = 1.6 \pm 0.03$ mm. **(d)** Walker trajectories with $\gamma/\gamma_F = 0.990$, drop radius $R = 0.39 \pm 0.01$ mm and free-walking speed $v_0 = 0.039$. The arrows denote the direction of motion and trajectories are colour-coded according to speed. A total of 449 trajectories were collected. **(e)** Experimental trajectories coloured according to their impact parameter y_i. These trajectories are obtained by rotating those shown in **d-iv** until the drop's initial motion is parallel to the x-axis. α then denotes the scattering angle at which the walker exits the well. **(f)** Simulated trajectories with uniformly-distributed impact parameters y_i for a drop with $v_0 = 0.024$ at $\gamma/\gamma_F = 0.990$. **(g)** Scattering angle versus impact parameters y_i for experimental (yellow dots) and simulated (solid lines) trajectories with walkers of different size (speed) at $\gamma/\gamma_F = 0.990$. The dotted magenta line corresponds to the same drop as the blue solid line but at a lower memory, $\gamma/\gamma_F = 0.970$. Space is non-dimensionalised by the Faraday wavelength $X_0 = \lambda_F$ in the shallow region and speed by $V_0 = X_0/T_F$, where $T_F = 2/f$ is the Faraday period.121

List of Tables

Chapter 1

Introduction

And it is entirely possible that future generations will look back, from the vantage point of a more sophisticated theory, and wonder how we could have been so gullible.
- David J. Griffiths [56]

More than a decade ago, Yves Couder and co-workers [23, 107] discovered that small liquid droplets can walk on the surface of a vibrating liquid bath, accompanied by their Faraday wave fields [43]. Owing to its quantum-like behaviour arising in a variety of different settings and its relation to the double-solution pilot-wave theory of de Broglie [31, 32], this walking droplet system has received considerable recent attention and has given rise to the field of hydrodynamic quantum analogues [14]. One goal of hydrodynamic pilot-wave theory is to answer the thought-provoking question posed by Bush *et al.* [15]: *Might deterministic chaotic pilot-wave dynamics underlie quantum statistics?*

In the walking droplet system, the quantum-like aspects emerge as the bath's vibrational acceleration γ approaches the Faraday threshold γ_F, the critical value above which the fluid bath spontaneously destabilises into a field of standing subharmonic waves with wavelength λ_F provided by the standard water-wave dispersion relation [70, 88]. Hence, when the bath's oscillatory motion has frequency f, the Faraday waves oscillate at frequency $f/2$. The key control parameter in the walker system, henceforth referred to as 'memory' and defined as γ/γ_F, provides a measure of the

vicinity of the vibrational acceleration to the Faraday threshold and so determines the longevity of the waves excited by the bouncing drop at each impact [39]. The memory time, or the characteristic decay time of the Faraday waves, is given by $T_M = T_d/(1-\gamma/\gamma_F)$, where $T_d \simeq \lambda_F^2/(4\pi^2\nu)$ is the wave decay time in the absence of vibrational forcing and ν is the liquid's kinematic viscosity [93, 14]. The memory parameter is a key ingredient to the dynamics of the walking droplets, as it prescribes the extent to which the droplet's past motion will affect its future. The system memory renders the system non-Markovian, an example of hereditary mechanics [11, 129, 72].

Hydrodynamic quantum analogues can be categorised according to whether they are closed or open [15]. Closed systems are those in which the droplet's motion is constrained, either by borders or confining potentials, to a domain of size D such that $T_M > T_c$, where $T_c \sim D/v$ is the droplet's crossing time and v its characteristic speed. The drop is thus continuously navigating its monochromatic wave field [114, 81, 24]. A number of robust hydrodynamic quantum analogues have been drawn from closed systems and are reviewed at length by Bush *et al.* [14, 16, 15]. These include orbital quantisation and Zeeman splitting in a rotating frame [49, 38, 62, 100, 102], double quantisation in angular momentum and orbital radius for motion in harmonic potentials [104, 103, 36, 81], as well as quantum-like statistics in circular corrals [65]. In all such closed systems, the physical picture is one of the droplet riding a wave-field (or effective potential) of its own making. Quantisation arises naturally from the fact that this wave field is effectively monochromatic, a feature ensured by the resonance between the bouncing drop and its pilot-wave. The walker system has some limitations as a quantum analog in open systems; in particular, the studies of walker diffraction from single and double slits show behaviour that is neither quantum mechanical nor purely classical [21, 3, 108]. We proceed by providing a brief overview of the relevant closed hydrodynamic quantum analogues.

The discovery of orbital quantisation of walkers in a rotating frame represented a pivotal early triumph. It was the first robust macroscopic realisation of phenomena previously thought to belong exclusively to the quantum realm. Fort *et al.* [49] demonstrated that, at low memory, the orbital radius of the walker varies continuously

with the rotation rate, as expected for a classical system. However, in the intermediate memory regime, they observed discrete bands of allowed orbital radii, with spacing between the adjacent bands being approximately equal to $\lambda_F/2$. The quantisation was rationalised in terms of the walker's interaction with its own previously generated wave fields. As the speed of the droplet remained approximately constant along each of its circular trajectories, it lead to an orbital angular momentum quantisation evoking the Bohr-Sommerfeld quantisation of electron orbits within an atom [19].

Harris *et al.* [62] built upon this work by providing a more thorough characterisation of the emergence of orbital quantisation in a rotating frame with increasing memory. They reported similar results to Fort *et al.* [49] for the low and intermediate memory regimes, finding in addition that the quantised orbits do not all appear at a single memory value. Specifically the number of quantised orbits increases with memory, with each orbit only being stable within a finite memory range. In the high-memory regime, they found that the circular orbits destabilise into wobbling orbits with stationary centres, which can drift and leap if the memory is further increased. For very high-memories, the droplet's trajectory is rendered more complex, being characterised by erratic switching between arcs corresponding to unstable circular orbits. The experimental observations of Fort *et al.* [49] and Harris *et al.* [62] have since been rationalised through the theoretical works of Oza *et al.* [100, 102], who also predicted the existence of even more exotic orbital states, only some of which have been observed in the laboratory.

A richer orbital quantisation arises for walker motion in a simple harmonic potential. Perrard *et al.* [104, 103] performed experiments with ferro-fluid suspended within a walking droplet and subjected this walker to a vertical magnetic field with a radial gradient, leading to an effective confining harmonic potential. They reported the existence of periodic and quasi-periodic trajectories, in the low and intermediate memory regime, respectively. This lead to the emergence of a double quantisation in orbital radius and angular momentum, demonstrating a classical analog of that arising in quantum mechanics. In the high memory limit, the authors observed chaotic motion and erratic switching between unstable partial orbits, similar to that reported

by Harris *et al.* [62] in the rotating frame.

A number of theoretical investigations have since explored walker motion in a simple harmonic potential. Labousse *et al.* [82] analysed the stability of the circular orbits arising at low memory and rationalised the corresponding quantisation of orbital radius. Durey *et al.* [36] created a robust method of analysing the droplet's trajectory as a build-up of stable sub-trajectories, allowing them to prove that the double quantisation occurs even in the high memory regime. Kurianski *et al.* [81] further explored numerically the walker dynamics and uncovered a number of periodic, quasi-periodic, and chaotic trajectories not yet observed experimentally. They also demonstrated that the system being closed is a requirement for double quantisation in the simple harmonic potential.

Quantum corrals are two-dimensional structures built atom by atom on an atomically clean metallic surface using a scanning tunnelling microscope (STM) [40, 47]. These formations confine electrons in the surface states of noble metals which lead to standing wave patterns in the electron density inside the quantum corral [47]. Crommie *et al.* [25] built the first corrals using iron atoms on a copper surface and imaged the standing patterns of the electron density inside them. The standard theoretical descriptions of the quantum corral will be reviewed in chapter 2. Of specific interest to our study is the quantum mirage, a geometrical resonance effect whereby placing a magnetic impurity at one focus of an elliptical corral induces an influence with comparable strength at both foci.

A successful analogy has been drawn between the droplets walking in confined geometries and electrons in quantum corrals [25]. Harris *et al.* [65] found that in the high memory limit, a coherent wavelike statistical behaviour, reminiscent of that of electrons in quantum corrals, emerges from the chaotic underlying dynamics of walkers in circular corrals. The modulation patterns observed in the particle location histogram and associated speed map resembled the dominant Faraday mode of the cavity. The study suggests that particle trajectories are not inconsistent with quantum-like statistics in corrals. Despite several attempts, [121, 52, 53], a conclusive theoretical demonstration of this robust statistical behaviour remains a challenge.

We will contribute to this discussion in chapters 3 and 6, when we revisit the hydrodynamic corrals and present the hydrodynamic analog of the quantum mirage.

Early investigations have also hinted at orbital quantisation in circular corrals. Harris *et al.* [65] found that at low and intermediate memories, walking droplets in the circular corral display periodic and quasi-periodic orbits reminiscent of those arising in the simple harmonic oscillator [104, 103]. In chapter 4 we will extend the work of Harris *et al.* through investigating experimentally the influence of memory on the dynamics of a walker in a circular corral.

While the similar form of the drop histogram and the Faraday wave mode of the circular corrals was noted by Harris *et al.* [65], until recently the mathematical link between the statistical behaviour and pilot-wave field of the walking droplet was not clear. Durey *et al.* [37] proved that for open walker systems, the mean wave field created by a walking droplet is equal to the convolution between the wave field of a stationary bouncing droplet and the position histogram of the droplet. A numerical investigation of the result of Durey *et al.* was undertaken by Tambasco and Bush [124] for a walker trajectory confined by a Bessel-like potential. They observed a good agreement between the numerically computed mean wave field and the convolution wave field, finding that the convergence time of one to the other is on the order of $\sim 34\ T_M$. Convergence to the statistically steady state took substantially longer $\sim 300\ T_M$. In chapter 6 we will present the first experimental test of Durey *et al.*'s convolution result for the hydrodynamic circular corral, and deduce the associated convergence times.

When the adatoms that make up the border of quantum corrals are placed in isolation on the surface of a metal, they produce modulations in the nearby electron sea. These wave-like patterns are the so-called Friedel oscillations [51] imaged by Crommie *et al.* [25] and Kanisawa *et al.* [77]. The quantum mechanical description of this phenomena, based on scattering theory, is reviewed in chapter 2. In chapter 5, we study the interaction of a walker with a submerged circular well, thus exploring a hydrodynamic analogue of Friedel oscillations, the first successful hydrodynamic quantum analogue in an open geometry.

In this thesis, we present a comparative study of the quantum corral [25, 27, 87, 47, 94], Friedel oscillations from an impurity [51, 25, 77], and their hydrodynamic analogues. We begin in chapter 2 with a broad discussion of classical and quantum mechanics, and a review of the standard quantum treatments of quantum corrals and Friedel oscillations. Chapter 3 focuses on the statistical projection effects in hydrodynamic elliptical corrals, the results of which are published in *Statistical projection effects in a hydrodynamic pilot-wave system*, P. J. Sáenz, T. Cristea-Platon and J. W. M. Bush, Nature Physics, 2017 [114]. The double quantisation of the fundamental trajectories in circular corrals, as well as the emergence of chaos, is described in chapter 4, the results of which are published in *Walking Droplets in a Circular Corral: Quantisation and Chaos*, T. Cristea-Platon, P. J. Sáenz and J. W. M. Bush, Chaos, 2018 [24]. The hydrodynamic analogue of Friedel oscillations from a localised topographic impurity is presented in chapter 5, and soon to be submitted as *Localized hydrodynamic pilot-wave statistics around a defect*, P. J. Sáenz, T. Cristea-Platon and J. W. M. Bush [115]. In chapter 6 we revisit the circular corral, providing an experimental test of the theoretical link between the mean wave field and the droplet position histogram developed by Durey *et al.* [37] and elucidating the origins of the emergent statistics. Finally, in chapter 7 we draw conclusions and discuss future research directions suggested by this work.

Chapter 2

Classical, Pilot-Wave and Quantum Mechanics

In this chapter we summarise the key distinguishing features between classical and quantum mechanics as well as pilot-wave theories that now arise in both the classical and quantum realms. We provide an overview of a number of the most prevalent interpretations of quantum mechanics. Finally, we will review in turn the *particle-in-a-box* description of electrons in quantum corrals and the scattering theory used to model both Friedel oscillations and quantum corrals.

2.1 Classical physics

People build their notions of reality on the basis of their interactions with the natural world. The subject of classical physics typically represents an umbrella for classical mechanics (be it either the Newtonian, Lagrangian or Hamiltonian formalisms) [55], classical electrodynamics (as laid out by Maxwell) [75], and classical thermodynamics (initially defined by Kelvin) [118]. These theories share the characteristic of being deterministic and until the advent of quantum mechanics many believed that classical physics was a complete theory, able to describe all the observable phenomena around us. With the formulation of the special and general theory of relativity, bizarre effects such as length contraction, time dilation, and the loss of simultaneity seemed

to contradict our classical intuition [130]. Nevertheless, upon closer inspection it lead to even *better* agreement between classical theory and experimental data, for example, through explaining the anomalous precession rate of the perihelion of Mercury's orbit [120].

Planetary motion was historically central to both general relativity and the development of another aspect of classical physics. Around 1890, Henri Poincaré discovered that for the motion of three gravitationally-interacting bodies, some trajectories are neither periodic, divergent, nor approaching a fixed point [106]. This dynamical behaviour would be known as chaotic motion.

2.1.1 Chaos

Chaos theory focuses on deterministic dynamical systems whose behaviour can in principle be predicted from evolution equations, for example, Newton's laws of motions. However, chaotic systems are highly sensitive to initial conditions and have constrained solutions, which places practical limits on predictability [122]. Thus, an arbitrarily small change, or perturbation, of a chaotic system may lead to significantly different future behaviour. The result, commonly known as the *butterfly effect* [84], is characterised mathematically by an exponential divergence with time of two nearby points in phase space at a rate given by the Lyapunov exponent [122].

Jacques Hadamard studied one of the first examples of *chaotic billiards*, specifically the chaotic motion of a free particle gliding frictionlessly on a surface of constant negative curvature [59]. He showed that they all diverge exponentially from one another, with a positive Lyapunov exponent. Although the foundations of chaos theory were laid out more than a century ago, its implications have only become widely recognised in the last 50 years [119]. In the early 1960's, Edward Lorenz was working on weather prediction models. He discovered that small changes in initial conditions could lead to divergent predictions in the long-term outcome, an effect amplified by the limited working precision of early computers. A famous quote attributed to Lorenz eloquently summarises chaos theory: *When the present determines the future, but the approximate present does not approximately determine the future.*

2.1.2 Pilot-wave hydrodynamics

Pilot-wave hydrodynamics describes the dynamics of walking droplets. The trajectory equation for the walker's horizontal motion was derived by Moláček and Bush [93]:

$$m\ddot{\mathbf{x}}_d + D\dot{\mathbf{x}}_d = -mg\nabla\eta(\mathbf{x}_d, t) \tag{2.1}$$

where $\mathbf{x}_d$ is the walker position and $\eta(\mathbf{x}_d, t)$ is the amplitude of its pilot-wave field. The droplet experiences a drag term proportional to its speed and an instantaneous force prescribed by the local gradient of the instantaneous wave field beneath it, $\nabla\eta(\mathbf{x}_d, t)$. The system variables are defined in table 2.1. As the droplets considered in the present thesis are resonant walkers, bouncing in synchrony with their accompanying Faraday wave field, the amplitude of the wave field can be written as a discrete sum of circularly symmetric standing waves centred at each impact's location:

$$\eta(\mathbf{x}_d, t) = \sum_{n=-\infty}^{\lfloor t/T_F \rfloor} AJ_0\left(k_F\left|\mathbf{x}(t) - \mathbf{x}_d\left(nT_F\right)\right|\right) e^{-(t-nT_F)/(T_F M_e)} \tag{2.2}$$

Oza *et al.* [101] approximated this sum as an integral and so obtained an integro-differential equation for the horizontal trajectory of a free walking droplet:

$$\eta(\mathbf{x}_d, t) = \frac{F}{T_F}\int_{-\infty}^{t} \frac{J_1\left(k_F\left|\mathbf{x}_d(t) - \mathbf{x}_d(s)\right|\right)}{\left|\mathbf{x}_d(t) - \mathbf{x}_d(s)\right|}\left(\mathbf{x}_d(t) - \mathbf{x}_d(s)\right) e^{-(t-s)/(T_F M_e)} ds \tag{2.3}$$

This approximation is valid when the timescale of vertical motion T_F is much smaller than the timescale of horizontal motion $T_H = \lambda_F/\left|\dot{\mathbf{x}}_d\right|$. From equations (2.2) or (2.3), it is apparent that the instantaneous force on the droplet depends on both the particle's previous path and the system 'memory', $M_e = T_d/\left(T_F\left(1 - \gamma/\gamma_F\right)\right)$, a measure of the extent to which the past affects its future. Owing to the influence of its wave field, the future of a droplet is affected by both its present and its past, rendering the walking droplet system non-Markovian, an example of hereditary mechanics [129]. In order to predict the system's future, one must know both its present and its

Dimensional variables	Definition
m	drop mass
R_D	drop radius
ν	fluid kinematic viscosity
σ	fluid surface tension
ρ	fluid density
μ_a	air dynamic viscosity
ρ_a	air density
f	forcing frequency
γ	forcing acceleration
γ_F	Faraday instability threshold
g	gravitational acceleration
$T_F = 2/f$	Faraday period
T_d	decay time of waves without forcing
$k_F = 2\pi/\lambda_F$	Faraday wavenumber, wavelength
Φ	mean phase of wave during contact
$D = 0.17mg\sqrt{\frac{\rho R_D}{\sigma}} + 6\pi\nu_a R_D\left(1 + \frac{\rho_a g R_D}{12\mu_a f}\right)$	drag coefficient
$A = \sqrt{\frac{1.5795\nu}{2\pi T_F}}\frac{mgk_F^3}{3k_F^2\sigma+\rho g}T_F \sin\Phi$	amplitude of wave force
$F = \sqrt{\frac{1.5795\nu}{2\pi T_F}}\frac{mgk_F^4}{3k_F^2\sigma+\rho g}mgT_F \sin\Phi$	wave force coefficient

Table 2.1: The variables in the trajectory equations (2.1), (2.2), and (2.3).

past. Chaotic dynamics in hereditary systems is a relatively new subject [72] and our hydrodynamic pilot-wave studies are expected to significantly contribute to its development [15].

A number of walker experiments have demonstrated how non-locality can be misinferred from local hereditary mechanics. For example, Harris *et al.* [60] investigated the interaction between a walking droplet and a submerged pillar. They inferred that a lift-type force was applied to the walker by the pillar, demonstrating that pilot-wave-mediated local forces can give rise to apparent action at a distance.

2.2 Quantum physics

The description of nature at the smallest scales, such as the electrons of an atom, is provided through the peculiar laws of quantum mechanics. One such law, which is as central to quantum mechanics as Newton's second law of motion to classical mechanics, is the Schrödinger equation (2.4) [116].

$$i\hbar\frac{\partial}{\partial t}\Psi(\mathbf{r},t) = \left[\frac{-\hbar^2}{2m}\nabla^2 + V(\mathbf{r},t)\right]\Psi(\mathbf{r},t) \tag{2.4}$$

where $\hbar$ is the reduced Planck constant, t is time, $\mathbf{r}$ is the position vector, m is the mass of the particle, and V is the external potential. Ψ represents the wave function, a mathematical description of a state of an isolated quantum system thought to encode *all the statistical* information of the system. The wave function, also called the state function, is a complex-valued probability amplitude that prescribes the probabilities for all the possible results of a measurement made on the system. In other words, this definition implies that if Ψ defines a fair coin that has been flipped and is about to land, Ψ only contains the information that there is a $50-50$ chance of obtaining heads or tails, but not the actual result of the coin flip. The Born rule [12] expresses that the probability density of finding the particle at a given point is proportional to the square of the magnitude of the particle's wave function at that point; if ψ is the wave function of the particle, then its probability density function is given by $|\psi|^2$. Notably, the linear Schrödinger equation provides no description of particle paths.

The semi-classical approach to quantum mechanics, founded on the Bohr-Sommerfeld quantisation condition [19], remained largely dormant until Gutzwiller developed the theory of periodic orbits [58]. He demonstrated that the quantum particle statistics occurring in confining geometries, such as quantum corrals, could be understood as emerging from localised wave packets moving along a superposition of classical billiard trajectories [79]. The periodic trajectories naturally lead to a dynamical time scale [112], $\tau_p \sim D/v_0$, corresponding to successive wall reflections of a localised wave packet of average speed v_0, propagating in a domain of size D. The dispersion of the initially localised wave packet with momentum uncertainty $\delta p = m\delta v$ over the area

of the confining geometry, gives rise to a second time scale [112], $\tau_s \sim D/\delta v$, after which the typical quantum statistics emerge. In chapter 6, we will investigate the periodic, weakly aperiodic and chaotic trajectories in the hydrodynamic corral and characterise the analogous timescales.

2.2.1 Quantum treatment of a particle in a circular corral

Consider an electron placed in a circular corral. This particle is initially well localised, but with time would explore the confining geometry and its wave function would be time-dependent, obeying (2.4). In fact, the initial purpose of the quantum corral, a physical realisation of a quantum box, was to explore precisely this evolution [47]. Early experimental investigations used stadium-shaped quantum corrals [25, 27, 28, 68, 69], however, the wave patterns observed were always time-independent, a result mainly attributed to leakage of electrons through the corral's walls [47].

We review here the standard, time-independent, quantum mechanical description of a particle inside a circular domain, whose walls act as an infinitely tall potential. The circular geometry is most relevant to our work on the hydrodynamic corral. For a circular well, we consider a potential

$$V(r,\theta) = \begin{cases} 0 & \text{if } r \leq L \\ \infty & \text{otherwise} \end{cases} \tag{2.5}$$

We seek a statistically steady state, hence (2.4) reduces to:

$$\left[\frac{-\hbar^2}{2m}\nabla^2 + V(\mathbf{r})\right]\Psi(\mathbf{r}) = E\Psi(\mathbf{r}) \tag{2.6}$$

where E is the energy of the particle. Outside the confining region, $\psi(r,\theta) = 0$. Inside, (2.6) requires that

$$-\frac{\hbar^2}{2m}\left(\frac{\partial^2\psi}{\partial r^2} + \frac{1}{r}\frac{\partial\psi}{\partial r} + \frac{1}{r^2}\frac{\partial^2\psi}{\partial\theta^2}\right) = E\psi \tag{2.7}$$

The boundary condition to be satisfied is $\psi(L,\theta) = 0$, for $\theta \in [0, 2\pi)$. The

normalisation condition requires that $\int_0^{2\pi}\int_0^L |\psi(r,\theta)|^2\, r dr d\theta = 1$. Hence, the possible wave functions of our system are

$$\psi_{n_\theta,n_r}(r,\theta) = \frac{1}{\sqrt{\pi}\left|J_{|n_\theta|+1}\left(k_{|n_\theta|n_r}\right)\right|} J_{|n_\theta|}\left(k_{|n_\theta|n_r} r\right) e^{in_\theta\theta} \tag{2.8}$$

$$E_{n_\theta,n_r} = \frac{\hbar^2 k^2_{|n_\theta|n_r}}{2m} \tag{2.9}$$

where ψ_{n_θ,n_r} is the stationary state with quantum numbers $n_\theta \in \mathbb{Z}$ and $n_r \in \mathbb{N}^*$, with associated energy E_{n_θ,n_r}, and r,θ are the radial and azimuthal coordinates, respectively. $J_{|n_\theta|}$ is the Bessel function of the first kind of order $|n_\theta|$ and $k_{|n_\theta|n_r}$ is the n_r-th positive root of $J_{|n_\theta|}$ divided by L. Notice an infinite set of modes with the lowest energy, corresponding to $n_\theta = 0$ and $n_r = 1$, and referred to as the *ground* state. Furthermore, n_θ plays the role of the quantised angular momentum of the particle and this sheds light on the physical intuition behind its allowed values. The particle can travel clockwise or counter-clockwise around the cavity, with the magnitude of angular momentum given by half the number of azimuthal nodes of the wave function. However, one cannot determine the sign of n_θ by inspection of (2.8) alone since, in this equation, the sign only appears in the phase term. Examples of various eigenmodes given by (2.8) are shown in figure A-1.

The closest approximation to domains with infinitely tall walls arise in microscopic structures known as quantum corrals. These are created by placing a series of identical imperfections, such as adatoms, on the surface of a conductor arranged to form a closed geometry, such as a circle (see figure A-2a [25]) or an ellipse (see figure A-2b-e [87]). The surface electrons inside this enclosure are largely confined or *corraled*, and their particle statistics display visually striking standing wave patterns. In the *particle-in-a-box* framework of quantum corrals, (2.6) is solved using Dirichlet boundary conditions to obtain a complete set of energy-dependent eigenstates for the electrons. The electron energies are assumed to follow a Gaussian distribution centred on the system's Fermi energy. Finally, one computes a weighted sum over a subset of eigenstates, typically those with energies within two-to-three Gaussian widths of the

Fermi energy, yielding the total eigenstate of the system. The normalised weights used in the aforementioned sum, are Gaussian-distributed values for the specific eigenstate energy [94]; however, their exact values are not specified by the theory and hence have to be calculated by fitting data from experiments. The incompleteness of the linear Schrödinger equation in describing quantum corral experiments is readily apparent.

Quantum corrals typically have ~ 30 particles within their confining walls. As the electrons do not interact, the single-particle analysis developed thus far is appropriate. Notably, in the hydrodynamic analogues described in chapters 3-6, the droplets do interact; consequently, we limit our experimental investigation to single particle systems, which are not yet experimentally feasible in quantum mechanics [47].

While the electron density patterns observed in the quantum corrals are time-independent, it is useful for our discussions of hydrodynamic corrals in chapters 3 and 6 to illustrate the simplest conceptual image of time-dependent quantum mechanics in a circular box. Consider a particle whose quantum state, Ψ, represents the equal superposition of two distinct solutions to (2.8), ψ_1 and ψ_2, respectively, with associated energies given by (2.9), $E_1 = \hbar\omega_1$ and $E_2 = \hbar\omega_2$, respectively. The time dependent state function of the particle, $\Psi(t)$, is then obtained by solving (2.4)

$$\Psi(t) = \frac{\sqrt{2}}{2} e^{\frac{-iE_1 t}{\hbar}} \psi_1 + \frac{\sqrt{2}}{2} e^{\frac{-iE_2 t}{\hbar}} \psi_2 \tag{2.10}$$

We see that the particle's state oscillates with time between the two fundamental eigenstates. Similar oscillations occur throughout quantum mechanics and are characteristic of the so-called *two-level Hamiltonian* systems. Examples include spin precessions in magnetic fields [19] and qubits, the building blocks of quantum computing [99]. More generally, multi-level Hamiltonian systems are those characterises by a broad spectrum of eigenstates, such as lasers, with the mathematical formulation extending naturally from (2.10).

2.2.2 Friedel oscillations

We proceed by reviewing the quantum mechanical description of electrons interacting with localised impurities. Assume that an atom or impurity is placed on the surface of a conductor. The two-dimensional electron gas (2DEG) nearby will respond to its presence by a redistribution of charge. We model this electron sea as an ideal ground-state Fermi gas, with Fermi-momentum $\hbar k_{Fermi}$, and assume that the impurity is electrically charged and can be modelled by a localised potential.

Friedel oscillations [51] are described in terms of standing waves formed from the interference between incoming and backscattered electron waves. They have been observed to arise around single impurities (see figure A-3a) [26, 77], from steps on a material's surface (see figure A-3b) [26, 66] as well as from a discrete arrangement of multiple impurities (see figure A-2) [25, 68, 28, 47]. Figure A-3b illustrates many of the features of this *quantum landscape*, including a fundamental wavelength $\sim \lambda_{Fermi}/2$, corresponding to half the Fermi wavelength. The following discussion will assume for simplicity that the system has a temperature of $0K$, such that there are no states with wavenumber greater than k_{Fermi} and the number density of states is constant across the allowed wave-numbers. Since $p = \hbar k$, this is equivalent to assuming a maximum particle momentum. To investigate the occurrence of Friedel oscillations, let us consider a geometry relevant to the hydrodynamic quantum analogues presented in chapter 5.

Suppose that at the origin, there is an infinitely tall barrier. The potential of this system is

$$V(r,\theta) = \begin{cases} \infty & \text{if } r = 0 \\ 0 & \text{otherwise} \end{cases} \tag{2.11}$$

Away from the origin, (2.6) yields

$$-\frac{\hbar^2}{2m}\left(\frac{\partial^2\psi}{\partial r^2} + \frac{1}{r}\frac{\partial\psi}{\partial r} + \frac{1}{r^2}\frac{\partial^2\psi}{\partial\theta^2}\right) = E\psi \tag{2.12}$$

This equation can be solved via separation of variables. The azimuthal part of

the wave function is given by $e^{in_\theta\theta}$, where n_θ is once again the azimuthal quantum number. The radial part of wave function is a linear combination of solutions to the ordinary Bessel equation, i.e. the regular Bessel $J_{n_\theta}(kr)$ and irregular Neumann $N_{n_\theta}(kr)$ functions, where k is the wavenumber of the solution. These represent the free solutions of the system in the absence of the scattering impurity. To account for the perturbation induced by the infinitely tall barrier at the origin, we look for a radial solution that is regular at $r = 0$ with asymptotic form similar to the free solution away from the impurity [98]:

$$J_{n_\theta}(kr) \to \sqrt{\frac{2}{\pi kr}} \cos\left(kr - \frac{n_\theta \pi}{2} - \frac{\pi}{4}\right) \tag{2.13}$$

$$N_{n_\theta}(kr) \to \sqrt{\frac{2}{\pi kr}} \sin\left(kr - \frac{n_\theta \pi}{2} - \frac{\pi}{4}\right) \tag{2.14}$$

The solution to our system is a linear combination of the above two asymptotes, multiplied by $e^{in_\theta\theta}$,

$$\psi_k(r,\theta) = A\sqrt{\frac{1}{kr}} \sin\left(kr - \frac{n_\theta \pi}{2} - \frac{\pi}{4} + \frac{\eta}{2}\right) e^{in_\theta\theta} \tag{2.15}$$

where A is the normalisation constant and η the scattering phase shift [1]. This solution is appropriate for $k_{Fermi}r >> 1$, which is valid in most experimental settings of relevance to us since the typical impurity size is comparable to the Fermi wavelength, λ_{Fermi} [48]. For symmetry, we require $n_\theta = 0$.

The electron sea density is given by the sum (or integral) over the probability distribution of all states below the Fermi energy:

$$n(r,\theta) = \sum_k |\psi_k(r,\theta)|^2 = \int_0^{k_{Fermi}} |\psi_k(r,\theta)|^2 \, kdk \tag{2.16}$$

$$n(r) = A^2 \int_0^{k_{Fermi}} \frac{1}{kr} \sin\left(kr - \frac{\pi}{4} + \frac{\eta}{2}\right)^2 kdk \tag{2.17}$$

$$n(r) = A^2 \frac{\cos(2k_{Fermi}r + \delta) + 2k_{Fermi}r - \cos\eta}{4r^2} \tag{2.18}$$

Hence the Friedel oscillation term in the electron density is

$$\delta n(r) \propto \frac{\cos(2k_{Fermi}r + \eta)}{r^2} \tag{2.19}$$

We note that the oscillations are sinusoidal, with wavelength half of the Fermi wavelength, and that they decay with the inverse of the distance squared (see figure A-4a).

Friedel oscillations also provide an alternative framework for treating the quantum corral. Specifically, the quantum corral can be understood in terms of either a *particle-in-a-box* system [25, 94], as seen in section 2.2.1, or as an array of interfering Friedel oscillators [47]. The former interpretation has the advantage of being a more intuitive model, based on cavity wave mode superposition; however, it has limitations in that the walls are not infinitely tall, so that electrons can leak out of the corral. The latter provides a more quantitatively accurate explanation and has extensions to even semi-closed geometries, such as arc-segment barriers. Nevertheless, the mathematical machinery of this formulation employs scattering theory and can obfuscate understanding. We note that both the *particle-in-a-box* and the scattering descriptions treat the particles as waves and their fundamental approaches are similar given that standing wave patterns can be decomposed into incoming and outgoing waves.

In the scattering picture of quantum corrals, electrons in the conduction band are free to move along the surface of the metal, and form the two-dimensional electron gas. For each adatom in the corral's wall, one solves (2.6) with a periodic potential modelling the atomic lattice of the substrate and a localised potential modelling the impurity [47], and proceeds to compute the associated Friedel oscillations. The collective interference of each adatom's Friedel oscillation leads to the typical standing wave pattern inside the corral (see figure A-2a). In chapter 6, we will discuss a new mechanism for the emergent statistics occurring in hydrodynamic corrals, inspired by insights from our study of the analogue Friedel system.

2.3 Quantum Interpretations

While Newton's laws of motion describe the *deterministic dynamics* of a macroscopic system, the Schrödinger equation describes the statistical behaviour of a microscopic system. What might underlie these statistics is a point of ongoing debate among physicists. The various philosophical viewpoints, espoused across the physics community, on how quantum mechanics corresponds to reality are referred to as the *interpretations of quantum mechanics.* We now outline the most prevalent. The Copenhagen interpretation renounces many of the general properties of a particle, including fundamental notions such as particle trajectory, in favour of a purely probabilistic depiction [56]. The insistence on the completeness of quantum mechanics in its purely statistical description of microscopic systems was lampooned by Einstein and Schrödinger in the form of Schrödinger's cat [41, 117].

Such is the philosophical extravagance of the Copenhagen interpretation that it has invited a proliferation of even more extravagant interpretations. While a Copenhagenist chooses to disregard particle trajectories, a subscriber to the Many-Worlds interpretation [42] prefers to violate energy conservation. According to the Many-Worlds interpretation, the act of observation causes the Universe to bifurcate into copies of itself, the only difference being the result of the observation. Even more bizarre and occult are the Consciousness Cause collapse [131] or the Many-Minds interpretations [2]. The Consciousness Cause collapse is similar to the Copenhagen interpretation, however it assumes that human consciousness is the cause of the wave function collapse. The Many-Minds interpretation represents a variant on the Many-worlds interpretation, the distinction being that it is the observer's mind that branches off with every probabilistic measurement performed.

Fortunately, there has been a recent shift towards more sensible interpretations, for which the present thesis provides further support. Many graduate level quantum mechanics courses have begun to focus on the Ensemble Interpretation. This interpretation describes the evolution of the wave function obeying the linear Schrödinger equation as that of a statistical average of similarly prepared states [6]. While the En-

semble interpretation does not deny the existence of a quantum dynamics underlying quantum statistics, it provides no insight into what that dynamics might be. Notably, all attempts to formulate a realist quantum dynamics have taken a pilot-wave form, in which a particle is guided by a wave.

2.3.1 Bohmian mechanics

A deterministic interpretation of quantum mechanics that attempted to restore trajectories to quantum particles was proposed by Bohm [9, 10]. Typically referred to as Bohmian mechanics, it asserts that quantum particles, such as electrons, obey Newtonian-like laws of motion and move in response to a pilot-wave field satisfying Schrödinger's equation (2.4). The theory represents a reformulation of quantum mechanics, a mix of dynamics and statistics, whereby the dynamics are driven by the statistics. We here provide a brief overview of the theory with a view to later distinguishing it from the pilot-wave dynamics proposed by de Broglie in the 1920's [31] and suggested by the walker system.

We introduce the Madelung transformation [85, 86] of the wave function:

$$\Psi(\mathbf{r},t) = Re^{iS/\hbar} \tag{2.20}$$

where $R(\mathbf{r},t)$ and $S(\mathbf{r},t)$ are real amplitude and phase functions, respectively. Inserting (2.20) into (2.4), we obtain the two coupled equations

$$\frac{\partial S}{\partial t} + \frac{(\nabla S)^2}{2m} - \frac{\hbar^2}{2m}\frac{\nabla^2 R}{R} + V = 0 \tag{2.21}$$

$$\frac{\partial R^2}{\partial t} + \nabla \cdot \left(\frac{R^2 \nabla S}{m}\right) = 0, \tag{2.22}$$

that represent a hydrodynamic formulation of quantum mechanics. The latter equation can be seen as the continuity equation for the probability distribution, $R^2 = |\Psi|^2$, associated with the system, while the former is an energetic equation. First, we will

make some associations pertinent to the terms in (2.21). In time-dependent quantum mechanics, the location with maximal probability of finding a particle may vary with time. This flow of probability (or the probability flux) is written as

$$\mathbf{j}(\mathbf{r},t) = \frac{\hbar}{2mi}\left(\Psi^*\nabla\Psi - \Psi\nabla\Psi^*\right) \tag{2.23}$$

In classical mechanics the flow of probability would represent a particle moving from one position to another. Bohmian mechanics equates the quantum velocity of probability with the particle velocity:

$$\mathbf{v}(\mathbf{r},t) = \frac{\mathbf{j}}{R^2} = \frac{\nabla S}{m} \tag{2.24}$$

Notably, the *quantum potential* [73],

$$Q(\mathbf{r},t) = -\frac{\hbar^2}{2m}\frac{\nabla^2 R}{R} \tag{2.25}$$

is the only term in eq.(2.21) containing $\hbar$. By taking the gradient of (2.22) and combining it with (2.24) and (2.25), one obtains an equation similar to Newton's second law of motion [9].

$$\frac{d}{dt}(m\mathbf{v}) = -\nabla\left(V + Q\right) \tag{2.26}$$

where

$$\frac{d}{dt} = \frac{\partial}{\partial t} + \mathbf{v}\cdot\nabla \tag{2.27}$$

is the Lagrangian derivative. The quantum potential, Q, is central to Bohm's theory as it is the source of non-locality: it represents a potential acting at all times on the particle and spanning all space. At a fundamental level, it is what makes a particle behave quantum-like. Note that the quantum potential plays a peculiar role in Bohmian mechanics: it is defined in terms of the system's statistics (through R), but has a dynamical influence on the particle. We will revisit the quantum potential in chapter 6, where we discuss its similarities to the mean wave field of walkers in the

hydrodynamic corral.

Einstein criticised Bohm's theory on the grounds that it predicts that no particle motion occurs in a closed geometry, such as a corral, if the system is described by a single eigenstate [73]. We highlight this shortcoming by considering the time-dependent wave-function of such a system, $\Psi(\mathbf{x}, t)$, the solution to the Schrödinger equation (2.4):

$$\Psi(\mathbf{x}, t) = \psi(\mathbf{x}) e^{iEt/\hbar} \tag{2.28}$$

where $\psi(\mathbf{x})$ is the single eigenstate and E its associated energy. Comparing (2.28) with (2.20), one obtains $S = E$. As $\nabla S = 0$, (2.24) implies that $\mathbf{v}(\mathbf{r}, t) = 0$ and that the particle remains motionless at its initial position.

Recent studies of Bohmian dynamics in circular corrals have assumed the presence of multiple eigenstates, hence a multi-level governing Hamiltonian, [30]. While chaotic trajectories were reported, no associated converged statistics were reported. A more general criticism of Bohmian mechanics is that it does not provide a mechanism for wave generation. Moreover, Bohmian mechanics is effectively kinematic: the Bohmian particle rides its pilot-wave without altering it.

2.3.2 de Broglie's double-solution pilot-wave theory

A much richer and less contrived portrayal of quantum particle dynamics is de Broglie's original formulation of pilot-wave theory [31], as was formulated in the 1920's in an attempt to reconcile quantum mechanics and relativity. De Broglie envisioned a particle with an internal oscillation at the Compton frequency, $\omega_c = mc^2/\hbar$. This particle vibration, or *zitterbewegung*, is characteristic of an exchange between rest-mass energy and wave energy as suggested by the de Broglie-Einstein relation, $mc^2 = \hbar\omega_c$ [14].

The culmination of de Broglie's work was his double-solution pilot-wave theory, which requires two distinct waves: the statistical wave of standard quantum mechan-

ics, ψ, and the pilot wave, u. A crucial aspect of the theory stressed by de Broglie is the "harmony of phases" or resonance between the particle's vibration and its pilot wave [32]. De Broglie defined the pilot wave, $u(\mathbf{x}, t)$, as a solution to the Klein-Gordon equation (2.29) [19]:

$$\frac{1}{c^2}\frac{\partial^2}{\partial t^2}u - \nabla^2 u + \frac{m^2c^2}{\hbar^2}u = 0 \tag{2.29}$$

and

$$u(\mathbf{x}, t) = Ae^{iS(\mathbf{x},t)/\hbar} \tag{2.30}$$

where A is a normalisation constant, and $S(\mathbf{x}, t)$ is a real function determining the phase of the wave. Substituting eq. (2.30) into eq. (2.29) yields the coupled equations

$$-\frac{1}{c^2}\frac{\partial^2 S}{\partial t^2} + \nabla^2 S = 0 \tag{2.31}$$

$$\frac{1}{c^2}\left(\frac{\partial S}{\partial t}\right)^2 - (\nabla S)^2 = m^2c^2 \tag{2.32}$$

A solution to eq. (2.31) that leads to a monochromatic pilot wave in the particle's frame of reference with de Broglie wavelength, $\lambda_{dB} = 2\pi/k$, is

$$S(\mathbf{x}, t) = \hbar(\mathbf{k}\cdot\mathbf{x} - \omega t) \tag{2.33}$$

Eq. (2.32) can be rearranged as

$$c^2\left(\frac{\nabla S}{\partial S/\partial t}\right)^2 = 1 - \frac{m^2c^4}{(\partial S/\partial t)^2} \tag{2.34}$$

The relativistic de Broglie-Einstein relation [32] for a particle of rest-mass m moving with constant speed v expresses the particle's energy as

$$E = \hbar\omega = mc^2/\sqrt{1 - v^2/c^2} \tag{2.35}$$

Using eq. 2.35 and $\partial S/\partial t = -\hbar\omega$, eq. 2.34 becomes

$$c^2\left(\frac{\nabla S}{\partial S/\partial t}\right)^2 = 1 - \frac{\hbar^2\omega^2\left(1 - v^2/c^2\right)}{\hbar^2\omega^2} \tag{2.36}$$

from which "the guidance formula", that governs the particle motion [32], is obtained:

$$\mathbf{v} = -c^2\frac{\nabla S}{\partial S/\partial t} \tag{2.37}$$

The relativistic momentum is defined as $\mathbf{p} = m\mathbf{v}/\sqrt{1 - v^2/c^2}$, and by substituting eq. 2.33 into eq. 2.37 we obtain the particle's associated momentum $\mathbf{p} = \hbar\mathbf{k}$. Thus the particle rides the wave field along a line of constant phase and has a constant speed. The physical picture of a particle riding its pilot-wave along a line of constant phase is clearly evident in the strobed videos of walking drops [61].

An important difference arises between de Broglie's pilot-wave theory and Bohmian mechanics. The former contains two waves: the statistical wave, ψ, predicted by quantum mechanics and a pilot-wave, u, centred on the particle. This contrasts with the Bohmian formulation, where the statistical wave coincides with the pilot-wave. As we will demonstrate throughout the present thesis, the walking droplet system captures all the critical aspects of de Broglie's mechanics and suggests the shortcomings of Bohmian mechanics. Specifically, it contains particle vibration in the form of vertical bouncing and the droplet walks via a resonant interaction with its associated monochromatic wave. Furthermore, there are two wave fields, a pilot-wave centred on the droplet and a statistical form prescribed by the system's geometry [14]. The walking droplet system provides the first classical platform for exploring pilot-wave dynamics, and speaks in favour of de Broglie's rather than Bohm's pilot-wave theory [14, 15].

Chapter 3

Statistical projection effects in a hydrodynamic pilot-wave system

Millimetric liquid droplets can walk across the surface of a vibrating fluid bath, self-propelled through a resonant interaction with their own guiding or 'pilot' wave fields. These walking droplets, or 'walkers', exhibit several features previously thought to be peculiar to the microscopic, quantum realm. In particular, walkers confined to circular corrals manifest a wave-like statistical behaviour reminiscent of that of electrons in quantum corrals. In this chapter, we demonstrate that localised topographical inhomogeneities in an elliptical corral may lead to resonant projection effects in the walker's statistics similar to those reported in quantum corrals. Specifically, we show that a submerged circular well may drive the walker to excite specific eigenmodes in the bath that result in drastic changes in the particle's statistical behaviour. The well tends to attract the walker, leading to a local peak in the walker's position histogram. By placing the well at one of the foci, a mode with maxima near the foci is preferentially excited, leading to a projection effect in the walker's position histogram towards the empty focus, an effect strongly reminiscent of the quantum mirage. Finally, we demonstrate that the mean pilot-wave field has the same form as the histogram describing the walker's statistics.

3.1 Introduction

Since the groundbreaking experiments of Yves Couder, Emmanuel Fort and co-workers [23, 107], significant effort has been devoted to examining the potential and limitations [3] of walking droplets as a hydrodynamic quantum analogue system [14]. Harris *et al.* demonstrated that the chaotic motion of a walker confined to a circular cavity, or 'corral', may lead to the emergence of a wave-like statistical behaviour, with the droplet's position histogram being prescribed by the eigenmode of the cavity [65], reminiscent of the probability distribution of a two-dimensional electron gas confined to a circular quantum corral [25]. Despite several attempts [121, 52, 53], a conclusive theoretical demonstration of this robust statistical behaviour remains an open challenge. The results in the circular corral [65] suggest the possibility of establishing deeper connections between these two markedly different systems.

The Kondo effect [78, 47] is the suppression in the local differential conductance of a metallic substrate due to the presence of magnetic impurities. In a remarkable recent set of experiments, Manoharan and co-workers [94] exploited this effect to demonstrate that, due to the special resonant properties of elliptical corrals, an individual atom (magnetic impurity) inside a quantum corral can be used to control the relative importance of specific cavity modes, thus allowing for the production of arbitrary superpositions of spatial quantum states [94]. When the magnetic impurity is placed at one focus, a particular elliptical eigenmode with extrema near the foci is preferentially excited, leading to a heightened statistical response in the electron density near the empty focus. Owing to the acute sensitivity of the differential conductance to the statistical response, the result is the projection of a pronounced minimum in the differential conductance from the occupied focus to the empty one, the so-called quantum mirage [87]. Here, we demonstrate that similar mode superposition and projection effects can be induced and manipulated in the walking droplet system by using a submerged circular well in the role of the magnetic impurity.

3.2 Experiments

A schematic of the experimental set-up is shown in Fig. A-5. An elliptical corral made of stainless steel was filled with 20 cSt silicon oil with density $\rho = 950$ kgm^{-3}, viscosity $\nu = 20.9$ cSt and surface tension $\sigma = 20.6$ mN m^{-1}. The eccentricity of the ellipse is $e = 0.5$ and the length of its semi-major axis is$a = 14.25$ mm. The corral was filled to a height $h = 1.70 \pm 0.05$ mm such that a very thin liquid film of depth $h_1 = 0.05 \pm 0.03$ mm overlays the border of the cavity, serving as a wave damper. The bath was mounted on an optical table and vibrated vertically by an electromagnetic shaker with acceleration $\Gamma(t) = \gamma \cos(\omega t)$, where γ and $f = \omega/2\pi$ are the prescribed maximum acceleration and frequency, respectively. Unless otherwise noted, the driving frequency was fixed at $f = 72$ Hz. The shaker was connected to the bath by a thin steel rod coupled with a linear air bearing to ensure a spatially uniform vibration to within 0.1% (ref. [63]). The forcing was monitored by two accelerometers, attached to the bath on opposite sides of the drive shaft, and a closed-loop feedback ensured a constant acceleration amplitude to within ± 0.002g (ref. [63]). A droplet of the same silicon oil with diameter $d = 0.79 \pm 0.01$ mm was generated with a piezoelectric droplet-on- demand generator and placed on the vibrating bath with the help of a removable slide [64]. Provided the driving acceleration was in the appropriate range, the drop could survive indefinitely by bouncing on the surface of the bath [22]. To ensure that ambient air currents did not affect the results, the corral was sealed with a transparent acrylic lid. We note that, although previous studies of walking droplets have considered the deep-water regime ($h > 4$ mm for the vibrational frequencies typically examined), we considered a relatively shallow layer in order to exploit variable bottom topography as a means of altering the drop's statistical behaviour.

The walker motion was recorded at 20 frames per second with a charge-coupled device (CCD) camera mounted directly above the bath and tracked with an in-house particle-tracking algorithm. The bath was illuminated with a light-emitting diode (LED) light ring to increase the contrast between the drop and the black background.

This visualisation set-up is optimal for droplet tracking but does not allow for observation of the wave field. The simplest method to capture the wave form is to view the normal reflection of light at the free surface [34]. To that end, a semi-reflective mirror at 45° was placed between the CCD camera and the bath, and the light ring was replaced by a diffuse-light lamp facing the mirror horizontally. Images can then be observed with bright regions corresponding to horizontal parts of the surface, extrema or saddle points [34] (Fig. A-6a,b). The wave field was recorded at frequency $f/4$.

When the driving acceleration exceeds the Faraday threshold γ_F, which depends on f, h, the fluid properties and cavity size, the bath spontaneously becomes unstable to a standing field of subharmonic Faraday waves [43, 88]. A critical parameter of the system is the so-called 'memory', γ/γ_F, which indicates the proximity of the driving acceleration to the Faraday threshold and so prescribes the longevity of the waves excited by the drop at each impact [39]. In the high-memory regime ($\gamma \to \gamma_F^-$), the waves are more persistent, so the droplet is more strongly influenced by its history [39].

For the range of parameters considered, $\gamma_F = 4.022$ g. We focus on the statistical behaviour of a walker in the high-memory regime, specifically $\gamma/\gamma_F = 0.998$, thereby ensuring that, as in the original corral experiment [65], the characteristic decay time of the subharmonic Faraday waves, or 'memory' time $T_M = T_d/(1 - \gamma/\gamma_F) \sim 7.8$ s, exceeds the droplet's characteristic crossing time $T_c = a/u \sim 1.6$ s. Here, $T_d = \lambda_F^2/(8\pi^2\nu)$ is the wave decay time in the absence of vibrational forcing [92], λ_F is the Faraday wavelength as prescribed by the standard water-wave dispersion relation, and $u \sim 6-9$ mms^{-1} is the characteristic speed of the droplet. If $T_M < T_c$, the waves decay faster than the droplet crosses the cavity and dissipation precludes the persistent wave field necessary for the emergence of the quantum-like statistical behaviour. The droplet motion was recorded for 3.5 h in 30 min intervals to maintain the prescribed memory, which may drift slowly owing to variations in viscosity and surface tension resulting from ambient temperature changes. γ_F was measured before and after each acquisition period and only data sets for which $|\delta\gamma_F|/\gamma_F < 0.001$ were retained, where

$\delta\gamma_F$ represents the variation in the Faraday threshold over a 30 min segment. The Faraday threshold is never crossed: the bath surface would remain flat in the absence of the droplet.

In this high-memory regime, the droplet motion is highly irregular. Its trajectory is characterised by frequent and abrupt changes in direction and speed prompted by impacts on its complex pilot wave field. Figure A-6a,b illustrate the spatio-temporal complexity of the instantaneous wave field and the associated droplet trajectory. Note that the instantaneous wave field inside the corral is markedly different from both the distinct horseshoe shape arising for a free walker [39] and from the corral's most unstable Faraday mode, whose form is evident in Fig. A-7c. Figure A-6c shows the drop trajectory, colour-coded according to speed, for paths of increasing length. Eventually, a well-defined pattern emerges, revealing a correlation between drop position and speed (Fig. A-6d). The histogram of the walker position (Fig. A-6e) reveals sharply defined regions that the walker visits more frequently, including two small circular regions near the centre of the ellipse and enclosing elliptical rings whose intensity decreases outwards. The average speed map presented in Fig. A-6f shows that peaks in the histogram correspond to regions of lower speed, as is also indicated in Fig. A-6d. Figure A-6f shows an overlay of the average velocity (arrows), which is effectively zero in the centre of the corral, indicating that the droplet visits each point there with some characteristic speed but with a random direction. Conversely, near the borders of the corral, an apparent quadrupole stream emerges in the mean velocity field. Specifically, the walker has a tendency to move along the border from the ends of the major axis towards the ends of the minor axis, where it then recirculates towards the corral centre.

Averaging the highly irregular instantaneous wave field (Fig. A-6a,b) over 30 min reveals a well-defined mean wave field (Fig. A-7a) with features strikingly similar to those characterising the position histogram and average speed map (Fig. A-6e,f). The brighter areas in the mean wave field represent regions whose average slope is zero and coincide with high-density and low-speed regions in the position histogram and speed map, respectively. This correspondence indicates that the walker's statistical response

is slaved to the mean wave field through the relatively incoherent, particle-centred, instantaneous pilot wave.

To rationalise this correspondence, we turn our attention to the Faraday waves emerging inside the corral, in the vicinity of the driving frequency, just above the Faraday threshold. It is important to distinguish these standing Faraday wave modes, which appear above threshold in the absence of the walker, from the instantaneous wave fields (for example Fig. A-6a,b) excited at $\gamma < \gamma_F$ by the walking drop, which decay both in time and space. Figure A-7c,e shows the Faraday waves observed at threshold $\gamma = \gamma_F$ with $f =$ 72and 70 Hz, respectively, which are well approximated by particular solutions of the Helmholtz equation for an elliptical membrane with Dirichlet boundary conditions. Specifically, the waves observed at $f = 72$ Hz (Fig. A-7c) correspond to the odd $(1, 5)$ elliptical eigenfunction (Fig. A-7d), while those found at $f = 70$ Hz correspond to the even $(4, 4)$ mode [57]. We note that Dirichlet boundary conditions are the most appropriate given the minimal thickness of the fluid film surrounding the cavity and the resulting tendency of surface tension and viscosity to minimise the wave amplitude there [8].

By superposing the $(1, 5)$ and $(4, 4)$ wave modes in equal weight as a first approximation, we find the pattern presented in Fig. A-7b, whose main features correspond closely to those of the mean wave field shown in Fig. A-7a and consequently to the walker's position histogram and speed map in Fig. A-6e,f. This correspondence indicates that the walker's seemingly chaotic motion is actually being dictated by the resonant Faraday modes of the cavity, some combination of which is subcritically $(\gamma < \gamma_F)$ excited at each impact. In this particular case, the walker appears to be exciting not only the Faraday mode at the driving frequency ($f = 72$ Hz) but also a second mode that is dominant at a nearby frequency ($f = 70$ Hz). The presence of other modes with relatively small weights cannot be discounted. We note that each drop impact must excite other eigenmodes in order to give rise to the intricate instantaneous wave field observed experimentally (Fig. A-6a,b). It is only in some exceptional occasions, when the walker happens to move along one of the main crests or troughs of one of the two fundamental cavity modes for an extended period, that

the instantaneous wave resembles either of these two modes (Fig. A-6). At each impact, the walker is thus exciting some collection of modes, two of which (the $(1,5)$ and $(4,4)$ modes) are predominant, their relative weight depending on the drop position and recent trajectory. The remaining rapidly decaying modes evidently have no significant effect on the mean wave field or the droplet statistics. The mean wave field also indicates that, on average, the dominant modes are being excited equally. We note that it has been shown that averaging chaotic Faraday waves well above threshold ($\gamma >> \gamma_F$), in the absence of a walker, also yields a mean field related to the linear wave modes of the cavity [54].

We now focus on demonstrating how localised topographic features in the form of submerged circular wells can vary the mode balance by diminishing or enhancing the resonance of specific cavity eigenmodes and so alter drastically the statistical response of the walking droplet. We machined a cylindrical well of diameter $D = 5.5$ mm and depth $H = 4.5$ mm on the bottom of the elliptical corral (Fig. A-5c) and repeated the experiment under precisely the same conditions as those in Fig. A-6. Because γ_F decreases for increasing liquid depth, the well is essentially generating a spatially varying memory distribution, and the effective local memory above the well is larger than elsewhere. Although we ensure that $\gamma < \gamma_F$ everywhere, drop-induced surface disturbances are larger in amplitude and more persistent above the well due to the local diminution of the rate of viscous dissipation. The submerged well can thus be thought of as playing the role of the impurity in the quantum corral: by encouraging the emergence of localised high-amplitude perturbations in the underlying wave field through topographically induced changes in the local memory γ/γ_F, it enhances the resonance of specific cavity modes.

Two distinct configuration are considered: (1) the well is located at the midpoint of the upper semi-minor axis; (2) the well is placed at the left focus (Fig. A-5d,e). The position histogram for the first configuration is presented in Fig. A-9a. In this case, we find that the impurity substantially diminishes the resonance of the dominant fundamental modes. By comparing Fig. A-9a with Fig. A-6e, we observe a drastic decrease in the definition of the histogram: only weak traces of the fundamental

modes are visible, along with localised high-density regions near the well. The latter indicate that the sub-merged well acts to attract the walker. The presence of the well also has noticeable effects in the walker's kinetics (Fig. A-9c). Specifically, the speed map depicts a brighter area at the well's position, indicating that the droplet speed is higher in the deeper region, as is consistent with drop speed increasing with memory [39, 92]. The average velocity map also underscores the attractive nature of the well. The direction of the arrows has changed in the upper half of the corral relative to the homogeneous corral (Fig. A-9c), indicating that the walker now has a heightened tendency to move from the centre of the corral towards the well, along the upper semi-minor axis, then recirculate back towards the extremities of the major axis along the border of the corral. The mean wave field, now with reinforced horizontal bands in the centre, is presented in Fig. A-9e. These features can be understood by examining the associated Faraday wave mode (Fig. A-9g), which cannot be represented by a single eigenfunction. Placing the well at the midpoint of the semi-minor axis evidently induces more than one cavity mode. We note that placing the well in a relatively low-symmetry position, for example on a diagonal, has a similar effect: a relatively incoherent mixture of cavity modes is induced.

A markedly different response is observed when the well is located at a focus of the elliptical corral. In this case, the well enhances the resonance of a particular mode with maxima near the foci. Specifically, the presence of the well results in the $(4, 4)$ mode, found at 70 Hz in the homogeneous corral, becoming resonant at 72 Hz (Fig. A-9h). This topographically induced effect has a drastic impact on the statistical behaviour of the droplet, which becomes slaved to the new dominant $(4, 4)$ wave mode. As a consequence, the histogram of the droplet presented in Fig. A-9b shows a markedly stronger signal, in which high-density vertical bands appear to be projected from focus to focus. The height of the histogram peaks above the foci is the same for the homogeneous corral (Fig. A-6e), but adding the submerged well at one focus (Fig. A-9b) causes the overlying peak to be roughly twice that of its counterpart over the empty focus. The intensified resonance of the $(4, 4)$ mode is also evident in the mean velocity field (Fig. A-9d), where new preferred paths emerge, including a

motion along the boundary from the left to the right side of the corral. The mean wave field (Fig. A-9f) also shows reinforced vertical bands, providing further evidence of the enhanced weight of the $(4,4)$ mode.

3.3 Discussion

It is constructive to discuss the similarities with and differences between our experimental results and the controlled mode superposition and projection effects arising in elliptical quantum corrals [94, 87]. The most striking difference is the vast disparity in scales between these macroscopic and microscopic systems. In the quantum experiment, the characteristic corral size and electron speed are $a \sim 75\,\text{Å}$ and $u = h/(m\lambda_{dB}) \sim 2.5 \times 10^5$ ms^{-1}, respectively [47], while the equivalent parameters are $a \sim 15$ mm and $u \sim 9$ mms^{-1} in the walking droplet experiment. The walking droplet system is a driven dissipative classical system for which the spatial decay rate of the waves imposes an upper bound on the size of the cavity. Although 84 electrons were bounded within the quantum corral in the experiments of Manoharan *et al.* [87], the theoretical modelling of the quantum corrals is based on a single-particle description [47]. Our experiments demonstrate how a similar behaviour may emerge from a single-particle hydrodynamic pilot-wave system. Another similarity between the hydrodynamic and quantum corrals has been brought to light by our study. The statistics in a topographically homogeneous corral at 72 Hz are prescribed by the superposition of two fundamental cavity modes. One might thus surmise that this particular bouncing droplet experiment is essentially a mixed-state system characterised by a two-level Hamiltonian [19].

We have demonstrated striking new similarities between hydro-dynamic and quantum corrals. We have shown that the statistical behaviour of the walker in a homogeneous elliptical corral can be described in terms of the superposition of a number of statistical states, a fundamental feature of quantum mechanics. Furthermore, we have demonstrated that a localised irregularity in the medium can drastically change the relative weight of the resonant modes and thus the statistical response of the

confined droplet. As in the quantum corral experiments [94, 87], we have shown that the position of the irregularity plays a critical role in the resulting statistical behaviour. High-symmetry configurations (specifically, with the well at the midpoint of the semi-minor axis) do not necessarily enhance the resonance of a particular cavity mode. However, when the impurity is placed at a focus, the walker induces a specific mode with maxima near the foci, leading to drastic changes in the statistical behaviour, including resonant projection towards the empty focus. Although these projection effects are directly evident in our hydro-dynamic system, they only become apparent in quantum corrals by subtracting the standing waves that arise with and without the impurity [47]. The quantum mirage, a projection effect in the differential conductance, results directly from the sensitivity of the local conductivity to the altered statistical response. New challenges posed by our study include the determination of analogues in the walking droplet system of electric current and differential conductance in quantum corrals.

In the context of hydrodynamic quantum analogues [14], our study represents a significant advance. In previous studies, the fluid depth was sufficiently large that the pilot waves could be described in terms of deep-water waves. Here, we have demonstrated that hydro- dynamic pilot-wave dynamics is viable in relatively shallow water, where the lower boundary influences the walking droplet's dynamics without entirely suppressing the Faraday waves [80]. Variations in topography may thus be used to generate spatial gradients in memory, effectively allowing for topographically induced potentials. Finally, we have characterised the mean pilot-wave field within the corral and demonstrated that its form is equivalent to the position histogram of the droplet and so also related to the fundamental modes of the cavity. While the focus of this study has been on effects akin to quantum superposition and projection, our results motivate consideration of hydrodynamic corrals of different geometries that will allow for quantitative comparative studies with quantum chaos in corrals [67] and quantum-mechanical pilot-wave theories [14].

Chapter 4

Walking Droplets in a Circular Corral: Quantisation and Chaos

A millimetric liquid droplet may walk across the surface of a vibrating liquid bath through a resonant interaction with its self-generated wavefield. Such walking droplets, or 'walkers', have attracted considerable recent interest because they exhibit certain features previously believed to be exclusive to the microscopic, quantum realm. In particular, the intricate motion of a walker confined to a closed geometry is known to give rise to a coherent wave-like statistical behaviour similar to that of electrons confined to quantum corrals. In this chapter, we examine experimentally the dynamics of a walker inside a circular corral. We first illustrate the emergence of a variety of stable dynamical states for relatively low vibrational accelerations, which lead to a double quantisation in angular momentum and orbital radius. We then characterise the system's transition to chaos for increasing vibrational acceleration and illustrate the resulting breakdown of the double quantisation. Finally, we discuss the similarities and differences between the dynamics and statistics of a walker inside a circular corral and that of a walker subject to a simple harmonic potential.

4.1 Introduction

Yves Couder and co-workers [23, 107] discovered that a small liquid droplet can walk above the free surface of a vibrating liquid bath, self-propelled via a resonant interaction with its own wavefield. Since their discovery more than a decade ago, these walking droplets have received considerable attention owing to their ability to exhibit behaviours analogous to those observed in a number of quantum systems (see review of Bush [14]). The quantum-like behaviour in the walking droplet system typically emerges as the bath's vibrational acceleration γ approaches the Faraday threshold γ_F, the critical vibrational acceleration above which the fluid bath destabilises into a field of standing subharmonic waves [88]. A crucial parameter in the walker system is the so-called 'memory', defined as γ/γ_F, which provides a measure of the proximity to the Faraday threshold and so the longevity of the waves excited by the bouncing drop at each impact [39]. In the high-memory regime, the waves generated by each impact are relatively persistent; consequently, the walker's motion is more strongly influenced by its past.

Harris *et al.* [65] investigated the motion of a walker confined to a circular cavity, or 'corral'. They found that at low and intermediate memories ($0.82 < \gamma/\gamma_F < 0.94$), the walker may display simple periodic trajectories. They focused their study on the emergence of a wave-like statistical behaviour in the high-memory limit. Specifically, they found that the seemingly chaotic motion of the drop eventually leads to a probability distribution related to the most unstable wave mode of the cavity, which is reminiscent of the probability distribution of a two-dimensional electron gas confined to a circular quantum corral [25]. Reproducing this robust statistical behaviour with theoretical models [121, 52, 53, 8] has proven to be challenging, owing largely to the subtleties of walker-boundary interactions [109].

Sáenz *et al.* [114] recently considered the dynamics of a walking drop in a relatively shallow elliptical corral. Owing to the special properties of this geometry, the authors demonstrated that a localised topographical inhomogeneity inside the corral may lead to resonant projection effects in the walker's statistics analogous to those observed

in elliptical quantum corrals [87, 47, 94]. In particular, the authors found that an inhomogeneity in the corral, in the form of a submerged circular well, may drive the walker to excite specific elliptical eigenmodes that result in drastic changes in the particle's statistical behaviour, as do magnetic impurities in the quantum corral. Finally, they demonstrated the emergence of a coherent mean (time-averaged) wave field with a form similar to the droplet's position histogram.

While the corral experiments sought to elucidate the statistical behaviour of walking drops confined by solid boundaries, other investigations have characterised and rationalised the dynamics of walkers confined by central forces. Perrard *et al.* [104, 103] performed experiments with ferro-fluid suspended within a droplet. By subjecting this walker to a vertical magnetic field with a radial gradient, they studied the effects of a confining simple harmonic potential on a walking droplet. The authors reported the existence of both stable and chaotic trajectories, and the emergence of a double quantisation in orbital radius and angular momentum over a certain span of memories. Their experiments thus demonstrate a classical analogue of the quantum mechanical eigenstates of the simple harmonic potential, as are defined in terms of their quantised energy and angular momentum.

The original experiments by Perrard *et al.* [104, 103] have motivated a number of theoretical developments. Labousse *et al.* [83] analysed the motion of a walker in an attractive potential and argued that the horizontal motion may be characterised in terms of three distinct time scales at high memory, associated with droplet propulsion on a straight-line, motion along a pivot with a preferred radius of curvatures, and self-organisation into a global wave structure associated with a periodic or quasi-periodic orbit. Labousse *et al.* [82] investigated the stability of the circular orbits arising at low memory and so rationalised the corresponding quantisation of orbital radius. Durey *et al.* [36] developed a relatively sophisticated method to analyse the drop's trajectory in terms of stable sub-trajectories, which allowed the authors to demonstrate that the double quantisation of orbital radius and angular momentum occurs even in the high-memory regime, where the dynamics are dominated by erratic switching between unstable periodic and quasi-periodic sub-trajectories. Kurianski

et al. [81] revisited this system theoretically with the stroboscopic model of Oza *et al.* [101] and captured a number of periodic, quasi-periodic, and chaotic walker trajectories, including a number that were not reported experimentally. Kurianski *et al.* also demonstrated that a requirement for double quantisation in the simple harmonic potential system is that the memory time (the characteristic decay time of the Faraday waves) exceeds the crossing time (the characteristic time taken for the drop to span its maximum range). Their study concludes with the observation that the specific details of the double quantisation identified in the hydrodynamic pilot-wave system are weakly sensitive to the specifics of the wave model used.

A common feature of walker motion in corrals and a simple harmonic potential is the presence of chaos. Tambasco *et al.* [125] were the first to characterise theoretically the onset of chaos in orbital pilot-wave dynamics. The authors considered the dynamics of walking droplets acted upon by external forces such as Coriolis, Coulomb, and linear spring forces. They demonstrated that the route to chaos followed in the destabilisation of circular orbits depends on the form of the external force. For the case of Coulomb and Coriolis forces, chaos sets in via a classic period-doubling cascade [105, 92]. In the case of a central harmonic potential, the route to chaos is reminiscent of the Ruelle-Takens-Newhouse scenario [113, 97].

Gilet developed a discrete theoretical model [52, 53] of walkers in circular corrals that captures the family of stable circular orbits arising at low memory reported by Harris *et al.* [65], as well as chaotic behaviour at higher memory. The transition to chaos with increasing memory was also characterised in terms of a supercritical Neimark-Sacker bifurcation. Rahman and Blackmore [110] build upon these model results for the special case of one-dimensional motion, and demonstrated that both supercritical and subcritical Neimark-Sacker bifurcations may arise. In the high memory limit, Gilet's model [52, 53] predicts trajectories with cusps at which the walker stops then restarts in a different direction. These sharp turning events occur at radii corresponding to the extrema of the axially symmetric wave eigenmode and so are separated by approximately half of the Faraday wavelength.

While walking drops in corrals [65, 52, 53, 110, 114] and harmonic potentials

[104, 103, 83, 82, 36, 81] are two of the more robust and rich examples of hydrodynamic quantum analogs, to date these two systems have been treated separately. Thinking of the circular corral walls as an alternative means of inducing a radial potential on a walking droplet allows one to place these systems on equal footing. Building upon the works of Harris *et al.* [65] and Sáenz *et al.* [114], we thus revisit the circular corral experiments to illustrate the emergence of a variety of dynamical states, stable at low memory and unstable at high, that lead to a double quantisation in the angular momentum and orbital radius reminiscent of that reported in the simple harmonic potential [104]. In addition, we characterise the system's transition to chaos with increasing vibrational acceleration, and discuss the concomitant disappearance of the double quantisation.

4.2 Experiments

A schematic of the experimental set-up is shown in figure A-10a. A circular corral made out of acrylic is filled with silicon oil with density $\rho = 950$ kg m^{-3}, viscosity $\nu = 20.9$ cSt, and surface tension $\sigma = 20.6$ mN m^{-1}. The bath is mounted on an optical table and vibrated vertically by an electromagnetic shaker with acceleration $\Gamma(t) = \gamma\cos(\omega t)$, where γ and $f = \omega/2\pi = 80$ Hz are the prescribed maximum acceleration and frequency, respectively. The circular corral of diameter $D = 20.2$ mm is filled to a height $h = 5.92 \pm 0.05$ mm such that a very thin liquid film of depth $h_1 = 0.22 \pm 0.03$ mm overlays its border, serving as a wave damper. The ratio of the cavity diameter to the Faraday wavelength is 4.25.

The shaker was connected to the bath by a thin steel rod coupled to a linear air bearing in order to ensure a spatially uniform vibration to within 0.1% [63]. The forcing was monitored by two accelerometers, attached to the bath on opposite sides of the drive shaft, and a closed-loop feedback ensured a constant acceleration amplitude to within ± 0.002 g [63]. A droplet of the same silicon oil of diameter $d = 0.70 \pm 0.01$ mm was generated with a piezoelectric droplet-on-demand generator and placed on the vibrating bath with the help of a removable slide [64]. To ensure that ambient air

currents did not affect the results, the corral was sealed with a transparent acrylic lid [108]. The image acquisition was done using a charge-coupled device (CCD) camera mounted directly above the bath operating at 20 frames per second. The bath was illuminated with a light-emitting diode (LED) light ring to increase the contrast between the drop and the black background. The walker's location was extracted using an in-house particle-tracking algorithm.

For γ just above the Faraday threshold γ_F (which depends on f, h, the fluid properties and cavity size), the bath displays the wave pattern shown in figure A-10b, corresponding to the most unstable Faraday wave mode of the cavity. This wave form is visualised using the normal reflection of light from the free surface [34], measurement of which required a semi-reflective mirror angled at 45° between the CCD camera and the bath, and a diffuse-light lamp facing the mirror and illuminating the bath [114]. The same technique was used to compute the instantaneous wave fields (e.g. figure A-10c,d), the averaging of which yielded the mean wave fields (figure A-10e,f).

Figure A-10c,d illustrate the instantaneous wave form and the associated droplet trajectory for two different memory values. At $\gamma/\gamma_F = 0.91$, the droplet follows a circular orbit centred on the corral (figure A-10c). At $\gamma/\gamma_F = 0.99$, the motion is irregular, with many abrupt changes in direction and speed (figure A-10d). The instantaneous wave form generally becomes more complex as the memory is increased. Figure A-10e,f illustrates the mean wave forms obtained by superposing with equal weights the instantaneous wave forms over a 15 minute interval [114]. Despite the drastically different walker behaviour, we note the striking similarity between both of these wave forms and the most unstable Faraday wave-mode of the cavity (figure A-10b). The features of the mean wave form become more pronounced at higher memories, as is consistent with the droplet dynamics being more strongly influenced by the mean wave field at higher memory [37].

We study the walker's dynamics exclusively for $\gamma < \gamma_F$, so that no waves would exist in the absence of the droplet. For the range of parameters considered, $\gamma_F = 4.732 \pm 0.004g$. We increased the memory of the system from $\gamma/\gamma_F = 0.87$ to 0.99

in steps of $\delta\gamma/\gamma_F = 0.005$. Each experiment was recorded for a period of 5 min. The characteristic decay time of the subharmonic Faraday waves, or memory time $T_M = T_d/(1-\gamma/\gamma_F) \sim 0.1-2$ s, where $T_d \sim \lambda_F^2/(8\pi^2\nu)$ is the wave decay time in the absence of vibrational forcing, and λ_F is the Faraday wavelength as prescribed by the standard water-wave dispersion relation [14]. The droplet's characteristic orbital or crossing time $T_c = D/(2u) \sim 2-4$ s, where $u \sim 4.2-5.7$ mm s^{-1} is the characteristic droplet speed in the range of memory under consideration. We note that these two timescales are comparable, indicating that we are in the memory-dominated regime in which the entirety of the bath surface is generally excited at all times [81].

4.2.1 Fundamental Trajectories and Double Quantisation

We proceed by detailing the evolution of the system with increasing memory for our small corral geometry. In relatively large domains, as γ is increased beyond the walking threshold, the stationary bouncing state gives way to rectilinear walking at a constant speed [23, 107, 92, 93]. In our small circular corral, the onset of motion is decidedly different. Just above the walking threshold, $\gamma/\gamma_F = 0.85$, the droplet executes rectilinear oscillations of amplitude comparable to its diameter. At slightly higher memories, specifically $\gamma/\gamma_F = 0.87$ (figure A-11a), the walker reaches its first stable trajectory, the centred circle of radius $\sim 0.32\lambda_F$ shown in figure A-10c. Progressively increasing γ/γ_F to 0.90 leads to the continuous expansion of the orbital radius to a value of $\sim 0.44\lambda_F$. At $\gamma/\gamma_F = 0.91$ the circle begins to wobble and destabilise, with the droplet describing a deformed circular orbit of maximum radial extent $\sim 0.7\lambda_F$ (figure A-11b). The second stable trajectory is reached at $\gamma/\gamma_F = 0.92$, when the walker describes a centred circular orbit with radius $\sim 0.7\lambda_F$ (figure A-11c). We note that the small and large circular trajectories (figure A-11a,c) roughly coincide, respectively, with the innermost and second innermost dark rings of the mean wave field evident in figure A-10e,f. Increasing the memory to $\gamma/\gamma_F = 0.93$ destabilises the larger circular orbits, leading to wobbling (figure A-11d).

Following the destabilisation of the large orbit, relatively complex trajectories arise, of the form illustrated in figures A-11e,f,g. As shown by Perrard *et al.* [104]

however, one may identify a variety of periodic and quasi-periodic sub-trajectories embedded within these complex trajectories, henceforth referred to as "fundamental trajectories", whose form depends on memory. At $\gamma/\gamma_F = 0.935$, we note the emergence of two fundamental trajectories, ovals and lemniscates (figure A-11e). Further increasing γ/γ_F leads to trefoils (figure A-11f) and papillons (figure A-11g). We note that in the range $\gamma/\gamma_F = 0.935 - 0.95$, multiple fundamental orbits may coexist at the same memory, with the dominant three being lemniscates, trefoils, and papillons. The orbits of figure A-11 are similar to those reported for walkers in the simple harmonic potential [104, 36, 81].

At the highest memories considered, $\gamma/\gamma_F = 0.98 - 0.99$, the droplet displays an erratic trajectory similar to that shown in figure A-11h, with sudden and seemingly unpredictable variations in speed. At this memory, the motion is characterised by trapped states, in which the droplet bounces in the place for a time ranging from 2 to 30 seconds. These trapping locations can be identified in figure A-11h by their corresponding zero speed. We note that trapped states have also been predicted by Oza *et al.* [100] for motion in a rotating frame at high memory and by Tambasco *et al.* [126] for walkers above the Faraday threshold. Such wave-induced trapping was not reported in the experiments of Perrard *et al.* [104, 103], but was evident in the numerical models of Gilet [52, 53].

In order to provide a more quantitative description of the fundamental trajectories arising for $\gamma/\gamma_F \leq 0.95$, we define the non-dimensional radial distance from the corral centre,

$$R(t) = \frac{r(t)}{\lambda_F},$$

and the non-dimensional angular momentum about the centre,

$$L_z(t) = \frac{\boldsymbol{r}(t)}{\lambda_F} \times \frac{\boldsymbol{V}(t)}{V_0},$$

where $\boldsymbol{r}(t)$ and $\boldsymbol{V}(t)$ are the walker's position and velocity. To be consistent with Perrard *et al.* [104], we define V_0 as the walker's speed along the first stable trajectory, specifically the small circle shown in figure A-11a.

Figure A-12 shows the time series of R and L_z over a complete orbital period for the lemniscate, trefoil, and papillon fundamental trajectories evident in figure A-11e,f,g. We note that, while the orbital periods for these 3 fundamental trajectories are different, the time difference between successive radial maxima is comparable. The angular momentum of the lemniscate (figure A-12b) displays a pair of positive and negative peaks of equal magnitude. The angular momenta of the trefoils (figure A-12d) and the papillons (figure A-12f) have either completely positive or negative angular momenta. The time between successive extrema of the angular momenta is approximately the same for lemniscates, trefoils, and papillons, and corresponds to the time between consecutive radial maxima. This common timescale can be understood by noting that the basic unit of time is that of a single loop, with the lemniscate containing 2 loops, the trefoil 3, and the papillon 4.

Following Perrard *et al.* [104], we characterise the walker's motion by its mean non-dimensional radial distance to the corral centre, $\overline{R}$:

$$\overline{R} = \frac{\sqrt{\langle R^2 \rangle}}{\lambda_F} = \frac{1}{\sqrt{N}} \sqrt{\sum_{k=1}^{N} \frac{r_k^2(t)}{\lambda_F^2}} \tag{4.1}$$

and its mean non-dimensional angular momentum about the centre, $\overline{L_z}$:

$$\overline{L_z} = \frac{\sqrt{\langle L_z \rangle}}{m \lambda_F V_0} = \frac{1}{N} \sum_{k=1}^{N} \frac{\boldsymbol{r_k}(t)}{\lambda_F} \times \frac{\boldsymbol{V_k}(t)}{V_0} \tag{4.2}$$

where $\boldsymbol{r_k}(t)$ and $\boldsymbol{V_k}(t)$ are the walker's position and velocity at the k-th point along the trajectory, N is the total number of points, and m the droplet mass.

Following the method developed by Durey *et al.* [36], we analyse the motion of the droplet in terms of periodic sub-trajectories by segmenting long trajectories between successive radial maxima. The values of $\overline{R}$ and $\overline{L_z}$ for each such segment are represented by a point in the $\overline{R} - \overline{L_z}$ plane. The next step leverages the use of K-means clustering to calculate the centroids of the global clusters in the $\overline{R} - \overline{L_z}$ space, in order to highlight the double-quantisation in the chaotic regime. We proceed in a similar fashion.

For $0.87 \leq \gamma/\gamma_F \leq 0.95$ (figure A-13a), identifiable clusters representative of double-quantisation are formed by the fundamental trajectories shown figure A-11. We note that $\overline{R}$ generally grows with increasing γ/γ_F. While qualitatively similar to the double-quantisation reported for the simple harmonic potential, there are a number of notable differences. For the circular corral, the quantisation in $\overline{R}$ occurs over the range 0.3−0.9, while that in $|\overline{L_z}|$ over the range 0−1.7. By way of comparison, in the simple harmonic potential, the double-quantisation occurs over the ranges $\overline{R} = 0.4 - 2.5$ and $|\overline{L_z}| = 0 - 1.9$ [81]. Hence, a radial compression is apparent: the fundamental orbits arise at lower $\overline{R}$. Furthermore, the lemniscates in the circular corral do not appear in two distinct clusters, resulting in an empty region in the centre of figure A-13a. Another difference is that the trefoils in the circular corral are defined by half the value of $\overline{L_z}$ reported for those in the simple harmonic potential. These differences presumably arise owing to the relatively sharp increase in the wall-induced effective potential close to the corral's edges.

For $0.95 < \gamma/\gamma_F < 0.98$, the disappearance of previously identified clusters occurs as the memory is increased, particularly the clusters corresponding to circles and ovals. Some remnants of the lemniscate, trefoil, and papillon clusters are apparent around $\overline{R} = 0.7$ for $|\overline{L_z}| < 0.5$. We notice the emergence of clusters with $\overline{L_z} \approx 0$ having a wide spread in $\overline{R}$.

For $0.98 \leq \gamma/\gamma_F \leq 0.99$, no noticeable double-quantisation is apparent (figure A-13b). Most trajectories are characterised by $\overline{L_z} \approx 0$, an effect due in part to the walker being trapped for extended periods, as is evident in figure A-11h. In addition, the erratic trajectories do not typically execute loops, but instead move along straight lines. We note the preponderance of trapped states at $\overline{L_z} = 0$ and $\overline{R} = 0.7$, denoted by blue circles, indicating the walker's propensity to be trapped [123] at the radius of the unstable large orbit (figure A-11c).

4.2.2 Chaos in the Corral

We proceed by characterising the system's transition to chaos that arises as the memory is increased progressively, and stable circular orbits give way to more complex

trajectories. Fourier analysis provides a means of characterising the onset of chaos using power spectra [46, 45]. A periodic trajectory is defined by a sharply peaked spectrum at one particular frequency as well as a number of higher harmonics [128]. A quasi-periodic trajectory is defined by a sharply peaked spectrum at multiple irrationally related frequencies as well as a number of higher harmonics [128]. A chaotic trajectory is characterised by a broad spectral form [128].

In figure A-14, we characterise the evolution with increasing memory of the power spectral form of the droplet radial position $R(t)$ as the circular orbit of radius $R_0 = 0.7$ destabilises into chaos (see figures A-11c,d). We note that the circular orbits found in the range $\gamma/\gamma_F = 0.87 - 0.93$ are stable. Whatever the droplet's initial position, it will eventually converge to such a circular orbit. The left column of figure A-14 illustrates the time-series of $R(t) - R_0$, where R_0 is the mean radius. The right column shows the associated power spectrum. The black circles highlight sharp peaks in the power spectra. At $\gamma/\gamma_F = 0.93$ the wobbling circles (figure A-14a) give rise to a power spectrum with one sharp peak (figures A-14b).

Figure A-14c shows the relatively complex time series corresponding to the trajectory in figure A-11g at $\gamma/\gamma_F = 0.95$. The associated spectrum (figure A-14d) shows multiple relatively broad peaks. The dominant peak corresponds to the orbital frequency of a droplet performing a loop, which represents half of a lemniscate, a third of a trefoil, and a quarter of a papillon. The other noticeable peaks are consecutive integer multiples of this dominant loop frequency. Similar plots are obtained for the memory range $\gamma/\gamma_F = 0.935 - 0.95$. In this range the walker's motion is characterised by chaotic switching between stable subtrajectories, as was also observed in the simple harmonic potential by Perrard *et al.* [104].

Figure A-14e shows the time-series of a droplet at $\gamma/\gamma_F = 0.98$ with trapped states present and no clear periodic structure. The associated frequency spectrum (figure A-14f) is broad with no distinct peaks. Similar spectral forms arose for larger memories as $\gamma \to \gamma_F$. Our power spectral analysis shows the transition of our system from periodic, to quasi-periodic, to chaotic trajectories as the memory is increased progressively. We note that numerical investigations of the routes to chaos in orbital

pilot-wave dynamics indicated that the transition to chaos happens over an extremely narrow range of γ [125]. For example, in the case of a walker in a simple harmonic potential, the transition arose over a span of $\Delta\gamma = 0.004$. Given the limitations in our experimental precision, a detailed characterisation of the route to chaos in corrals was thus impractical. Nevertheless, we have traced the evolution from periodic to quasi-periodic to chaotic trajectories with increasing γ.

Finally, figure A-15 illustrates the chaotic switching between fundamental trajectories observed at intermediate memories, specifically $\gamma/\gamma_F = 0.95$. Notice the appearance of lemniscates, trefoils, and papillons, as may be identified by their signature time series shown in figure A-12. Multiple switches between precessing fundamental orbits are a defining feature of the trajectories observed at $\gamma/\gamma_F = 0.95$. This behaviour is reminiscent of that reported by Perrard *et al.* [104], who showed that the chaotic trajectories found experimentally for the simple harmonic potential are characterised by transitions between unstable periodic orbits.

4.3 Discussion

Our study serves to connect two hydrodynamic quantum analogs previously considered to be disparate, walker dynamics in a circular corral and in a simple harmonic potential. Both systems are characterised by periodic and quasi-periodic orbits at low memory, and complex chaotic trajectories at high memory. Both systems are characterised by trajectories with preferred radii and angular momenta that lead to a double-quantisation reminiscent of that arising in the quantum simple harmonic oscillator. We have highlighted the similarities and differences between the double quantisation arising here and that reported by Perrard *et al.* [104], Durey *et al.* [36], and Kurianski *et al.* [81] for walker motion in a simple harmonic potential. The similarities may be rationalised on the grounds that the corral walls play the role of a relatively sharp confining potential. However in the high memory regime, the dynamics in the two system are markedly different: the walker in the corral moves erratically between trapped states, presumably owing to the interactions between its

pilot-wave and the boundary walls.

Through their influence on the walker wave field, the corral walls act to repel the drop from its edges [109]. One thus expects that the influence of the corral boundaries may be described crudely in terms of a steeply increasing effective radial potential, with a form lying somewhere between a two-dimensional simple harmonic potential and an infinite circular step potential.

Finally, we have examined via power spectra analysis the emergence of chaotic behaviour in our system as the memory is increased progressively. Specifically, we tracked the evolution from periodic to quasi-periodic to chaotic behaviour. A more detailed characterisation of the route to chaos would be possible by following an approach similar to that of Tambasco *et al.* [125, 124] or by building upon the theoretical results of Gilet [52, 53] and Rahman and Blackmore [110]. The relation between routes to chaos in the walker system and the pure Faraday wave system [18, 71] is also the subject of current interest. We were able to track the evolution from periodic to quasi-periodic to chaotic behaviour. A more detailed characterisation of the route to chaos would be possible if one was able to theoretically model the motion of walkers in circular corrals following an analysis similar to that of Tambasco *et al.* [125].

Chapter 5

Localised hydrodynamic pilot-wave statistics around a topographical defect

Impurities on the surface of a metal may modify its transport properties [17] and lead to the emergence of wavelike statistical patterns in the surrounding electron sea known as Friedel oscillations [50, 25]. In this chapter, we demonstrate that, despite its vast difference in scale, a classical hydrodynamic pilot-wave system [14] may exhibit strikingly similar statistical behaviour. Through experiments and simulations, we study the wave-mediated interaction between a liquid drop self-propelling on the surface of a vibrating fluid bath [23] and a submerged circular well, as plays the role of an impurity, or topographical defect, in the medium. The well induces a self-excited attractive force that draws the drop inwards along an Archimedean spiral, before it crosses over the well and departs along a straight radial path. The drop is thus scattered relative to the incoming direction. Oscillations in the drop speed emerge in its outgoing trajectory due to the waves induced by the drop's resonant interaction with the well. By considering an ensemble of particle trajectories, we demonstrate the emergence of localised wavelike statistics in the otherwise uniform histogram of the particle position, an effect strongly reminiscent of Friedel oscillations. The emergent statistical behaviour is rationalised in terms of a wave-mediated interaction

mechanism, which motivates similar mechanistic explorations of localisation effects from a particle within disordered media [4] or in particle-particle interactions [74].

5.1 Introduction

Motivated by both fundamental and technological reasons, the role played by defects on charge-carrier mobility has been one of the most exhaustively studied phenomena in modern condensed-matter physics [76]. A collection of disordered impurities may cause an electron to become immobile in a semiconductor through Anderson localisation [4]. A single magnetic impurity embedded within the electron sea on the surface of a metal may lead to an increase in the electrical resistivity at low temperatures, the so-called Kondo effect [78]. A region of localised Mott screening [95] typically adjoins such an isolated impurity, beyond which decaying Friedel oscillations arise [50, 25, 77]. By placing an array of such impurities in specific geometrical patterns, such as circles or ellipses [25, 87], the oscillations may interfere constructively and display standing-wave patterns in the enclosed electron sea that can be interpreted in terms of eigenmodes of the bounding cavities [47], or so-called quantum corrals. Remarkably, wavelike statistics [25] and mode superposition effects [87] similar to those emerging in quantum corrals have been recently reproduced with a classical hydrodynamic pilot-wave system [65, 114].

A millimetric liquid drop may self-propel along the surface of a vibrated liquid bath through a resonant interaction with its own wave field [23, 107]. This coupled wave-particle object, henceforth termed a Faraday 'walker', extends the range of classical mechanics to include certain features previously thought to be exclusive to quantum systems [14]. Quantum-like behaviours have been reported primarily in effectively 'closed' systems, wherein the drop's spatial domain is limited by either applied forces [49, 38, 103, 37] or solid boundaries [65, 114, 24]. A requirement for the emergence of quantisation and quantum-like statistics is that the 'memory' time [39], as dictates the longevity of the drop's guiding or 'pilot' wave field, exceed the time taken for the drop to cross its domain; thus, the drop continually navigates its self-excited wave

field. Wavelike statistics emerge in these settings when the drop dynamics becomes chaotic, and the drop switches between unstable periodic orbital states [15].

The distinction between closed and open systems is also fundamental at the quantum level: 'particle-in-a-box' models [25, 87] may qualitatively rationalise the observed resonance energies of closed structures, but they have no predictive power for resonance widths or standing-wave patterns in open systems [47]. Friedel oscillations [50, 25, 77], an effectively open phenomenon, result from single electron-impurity scattering interactions, and are manifest as localised, spatially-decaying, wavelike modulations in the free electron sea surrounding the atomic impurity. Sufficiently far from the impurity, the charge carriers are undisturbed by screening effects, and the electron sea is homogeneous. Here, we combine experiments and simulations to demonstrate that hydrodynamic pilot-wave dynamics around a topographical defect may lead to a statistical behaviour analogous to Friedel oscillations. The localised wavelike statistics are rationalised in terms of a wave-mediated scattering mechanism that is markedly different from that arising in closed hydrodynamic analogs [65, 114, 49, 38, 103]. Notably, no such interaction mechanism has been elucidated in the related quantum systems [50, 25, 77], where microscopic impurities are simply modelled in terms of scattering potentials [47].

5.2 Experiments

We consider the interaction between a walking drop and a topographical defect in the form of a submerged circular well at the bottom of the vibrating liquid bath (Fig. A-16a). The plan view and schematic cross section of the bath are shown in Fig. A-16b,c. The drop and bath are both composed of 20 cSt silicon oil with density $\rho = 950$ kgm^{-3} viscosity $\nu = 20.9$ cSt and surface tension $\sigma = 20.6$ mN m^{-1}. The bath is vibrated vertically with an electromagnetic shaker operating at forcing acceleration $\Gamma(t) = \cos(2\pi ft)$, where $f = 70$ Hz is the prescribed oscillation frequency. A spatially uniform vibration with an acceleration amplitude γ that is constant to within $\pm 0.002g$, where g is the gravitational acceleration, is achieved by using the

vibrating setup detailed elsewhere [63]. We define the Faraday threshold γ_F as the critical vibrational acceleration above which a standing field of Faraday waves [43] is excited in the vicinity of the well. In all experiments, $\gamma < \gamma_F$, so no waves exist in the absence of the drop. The bath depth beyond the well $h = 1.6 \pm 0.03$ mm is chosen as to ensure that the walker responds to variations in bottom topography [114]. The well diameter $D = 13 \pm 0.1$ mm is chosen so that the Faraday waves emerging at threshold $\gamma = \gamma_F$ are concentric (Fig. 3c). The well depth $H = 6.2 \pm 0.03$ mm is sufficiently large with respect to the Faraday wavenumber k_F that the well corresponds to the so-called deep-fluid regime, i.e. $\tanh k_F H \simeq 1$.

The experiment is performed at a forcing acceleration $\gamma/\gamma_F = 0.990$, where $\gamma_F \simeq 3.820g$. Notably, $\gamma_F^H < \gamma_F < \gamma_F^h$, where $\gamma_F^H \simeq 3.325g$ and $\gamma_F^h \simeq 4.050g$ are the Faraday thresholds of uniform baths of depth H, and h, respectively. Decaying monochromatic Faraday waves with wavelength $\lambda_F = 2\pi/k_F$, prescribed by the standard capillary-gravity dispersion relation $\omega_F^2 = (gk_F + \sigma k_F^3/\rho)\tanh k_F h$, are excited by the impacting drop, where $\omega_F = \pi f$ is the Faraday frequency. Note that the Faraday wavelengths corresponding to the shallow $\lambda_F^h = 5.19$ mm and deep $\lambda_F^H = 5.27$ mm regions are only marginally different. The wave-induced lateral force on the drop is $\mathbf{F}(\mathbf{x}_p, t) \sim mg\nabla\eta|_{\mathbf{x}=\mathbf{x}_p}$ where m is the drop mass and $\nabla\eta|_{\mathbf{x}=\mathbf{x}_p}$ the surface height gradient evaluated at the point of impact $\mathbf{x}_p(t)$ [107, 93]. The waves decay exponentially $\sim e^{-t/T_M}$ with a characteristic timescale $T_M = T_d/(1 - \gamma/\gamma_F)$, as dictates the memory time of the system [39]. Here, T_d is the local wave decay time in the absence of vibration [39, 93], and γ_F the local Faraday threshold. Owing to its influence on both the Faraday threshold and wave-decay rate, the well may be seen to act as a region of high excitability.

A drop with radius $R = 0.39 \pm 0.01$ mm is created using an on-demand piezoelectric drop generator [64]. The resulting walker motion is characterised by the synchronous $(2, 1)$ walking mode [132] in both the deep and shallow regions. In the absence of the well and boundary interactions, the drop executes rectilinear motion at the free-walking speed $v_0 = 7.1$ mm s^{-1}. A submerged star-shaped wave damper around the border of the bath serves as a passive launcher that continuously redirects the drop

towards the well (Fig. A-16b). The liquid height above the damper is 0.2 ± 0.1 mm. The distance between the region of interest around the well and the innermost part of the launcher is sufficiently large ($\sim 6\lambda_F^h$) that boundary effects play a negligible role on the walker-well interactions. The time that the drop takes to revisit the well, typically $\sim 50 \pm 20$ s, is much longer than the relevant memory time $T_M \sim 2.5$ s; thus, only memory effects related to the current interaction are significant. The bath is sealed with a transparent acrylic lid to shield the system from air currents. The walker motion is recorded from above with a CCD camera at 20 frames per second and tracked with an in-house particle-tracking algorithm. The wave field (Fig. A-19a) is visualised by placing a semi-reflective mirror at 45 ° between the camera and the bath, and lighting horizontally with a diffuse-light lamp. Bright regions then correspond to horizontal portions of the surface, dark regions to areas of large slope [34].

A total of six hours of experimental data was recorded, acquired in one-hour intervals to minimise temperature-induced drifts in γ_F, which were limited to $\pm 0.01g$. Fig. A-16d shows the walker trajectories in the vicinity of the submerged well. Initially, the drop approaches the well along a straight path with some offset relative to the well centre, the so-called impact parameter y_i. The drop then spirals in towards the well as if acted upon by an attractive force. After passing through the well, the drop departs radially along a rectilinear path off set by an angle α relative to its incident path, henceforth the scattering angle. The walker accelerates significantly when passing above the well due to the local generation of relatively high-amplitude waves; however its vertical motion is largely unaffected. A total of 449 trajectories were collected, the superposition of which reveals a striking pattern of evenly-spaced, concentric speed modulations (Fig. A-16d-iv). Before discussing the statistical implications of such a spatially-dependent speed distribution, we rationalise its origins by examining the drop trajectories in greater detail.

The experimental trajectories are characterised in terms of y_i and α in Fig. A-16e. The well evidently acts as a scatterer. In order to explore further such walker-well interactions (as are limited experimentally by the finite bath size), we complement our experiments with simulations based on the quasi-potential model of Faria [44],

according to which the influence of step-wise variable bottom topography is captured through its effect on the local wave speed (See the Appendix B for a detailed description of the model and associated numerics). In all the simulations presented, a uniform distribution of impact parameters y_i is considered, with resolution $\delta y_i/\lambda_F^h = 0.25$. The resulting trajectories (Fig. A-16f) are virtually identical to those arising in our experiments. Fig. A-16g shows the relation between y_i and α in both the experiment and simulations. Excellent quantitative agreement is observed. The simulations further demonstrate that the well-induced attraction is spatially limited: α increases monotonically with y_i, up to a critical tethering length y_T beyond which the walker is not drawn into the well (Fig. A-16g). We use the simulations to examine the influence of γ/γ_F, and drop size $0.353 \leq R \leq 0.425$ mm, the latter correspond to drop speeds in the range $0.024 \leq v_0 \leq 0.055$ at $\gamma/\gamma_F = 0.990$ (see Appendix B, Numerical Simulations section). For a given γ/γ_F, smaller (slower) drops lead to larger y_T and α. For a given drop speed, decreasing γ/γ_F reduces y_T but α is virtually unaffected (Fig. A-16g).

By rotating clockwise the walker trajectories (Fig. A-16f) by their corresponding scattering angles α, all collapse onto an Archimedean spiral, of the form $r = a + b\theta$ (Fig. A-17a). Note the nearly linear relationship in $r(\theta)$ (Fig. A-17b) and the satisfactory fit to a pure Archimedean spiral (Fig. A-17c). The impact parameter y_i determines when the walker locks onto the spiral. The spiral slope $b = dr/d\theta$, which along with y_i determines the scattering angle $\alpha \sim y_i/b$, is largely unaffected by γ/γ_F but decreases in magnitude with increasing drop speed v_0 (Fig. A-17b). An expression for the effective well-induced force on the drop during the incoming phase may then be inferred [60]. Using the spiral parametric equation $r(\theta)$ with constant the speed v, as is the case for $r \geq 2.5\lambda_F$ (Fig. A-17b), one may substitute into $md\mathbf{v}/dt = \mathbf{F}_w$ to deduce (see Appendix B, Effective Force section) the effective well-induced force $\mathbf{F}_w$,

$$\mathbf{F}_w = m\left(1 + \frac{\dot{r}^2}{v^2}\right)\dot{\mathbf{\Theta}} \times \mathbf{v} \tag{5.1}$$

where $\dot{\theta} = (v_\theta/r)\hat{\mathbf{e}}_\mathbf{z}$ is the instantaneous angular velocity of the drop around the

well centre and $\hat{\mathbf{e}}_\mathbf{z}$ the vertical unit vector. Note that $\mathbf{F}_w$ is a lift force, orthogonal to the direction of drop motion. Our experiments indicate that this effective well-induced force may be tuned through the outer fluid depth h. Specifically, decreasing h may lead to trapped states in which the drop is unable to escape the well (Fig. A-17d), as are known to arise for $\gamma > \gamma_F$ [123, 126, 124].

We now turn our attention to the walker's statistical behaviour in the vicinity of the well (Fig. A-16d-iv). We split the trajectories at their point of nearest approach to the well centre into incoming (Fig. A-18a) and outgoing (Fig. A-18b) phases. While the speed along the incoming spiral phase is constant and equal to v_0 beyond the well (Fig. A-18a), the straight outgoing trajectories display speed oscillations (Fig. A-18b). These outgoing speed modulations are also evident in the simulations (Fig. A-18d,e). Comparing the speed pattern (Fig. A-18b) with the Faraday wave mode of the well (Fig. A-18c) reveals their spatial correlation; specifically, the wavelength of the speed modulations is λ_F. Note that these speed modulations are not the result of the walker moving over externally imposed Faraday waves; rather, they reflect self-excited wave-mediated forces generated by the resonant interaction between the walker and the well. Figs. A-18f,g demonstrate that, for a given drop, the instantaneous speed data $v(r)$ for all the trajectories collapses onto the same curve, indicating the insensitivity of the statistical behaviour to the initial conditions. Note that the relative amplitude of the speed modulations increases for smaller drops. Fig. A-18d-e shows the trajectories for the smallest drop simulated (previously shown in Fig. A-16f), in which speed oscillations are enhanced relative to the experiments.

The localised wavelike statistical behaviour in the vicinity of the well is most clearly manifest in the histogram of the walker position. The data shown in Fig. A-18f,g results in the position histograms presented in Fig. A-18h-i. The statistical modulations, only evident in the histograms of the outgoing phase (Fig. A-18i), have the same spacing, λ_F, as the speed oscillations but are out of phase. Speed minima thus correspond to peaks in the histogram. The relative size of the statistical modulations is thus prescribed by the amplitude of the speed oscillations; hence, slower drops have more pronounced statistical modulations. The different decay rates apparent in

Fig. A-18h are simply the result of the well having a larger range of influence on smaller drops. A 2D rendering of the experimental and simulated histograms is presented in Fig. A-18j-k, which bears a striking resemblance to the Friedel oscillations around a magnetic impurity [50, 25, 77]. Moreover, we note that the amplitude of the walker's histogram modulations, relative to the histogram height at the centre of the well, is $\sim 0.8\%$ (Fig. A-18k), comparable to that in the quantum experiment, $\sim 1.5\%$ [25].

Having described the scattering and statistical behaviour emerging from the wave-mediated drop-well interaction, our hydrodynamic system allows us to take a step further and detail the underlying mechanisms. We thus examine the wave field $\eta(\mathbf{x}, t)$ through which the drop interacts with the well (Fig. A-19a,b). Of particular interest is the well-induced, or 'anomalous', wave field $\zeta(\mathbf{x}, t) = \eta - \bar{\eta}$ (Fig. A-19c), which is obtained by subtracting from the simulated wave field $\eta(\mathbf{x}, t)$ (Fig. A-19b) that of the same drop following the same path in the absence of the well $\bar{\eta}(\mathbf{x}, t)$ (as may be computed via simulation).

The scattering properties of the well are related to the emergence of a beam-like [90] structure in the anomalous wave field during the incoming phase (Fig. A-19c-ii). This beam, whose origin lies in the resonant reflection of subharmonic waves between regions of different depth, spans the drop and the well, rotating around the well while sliding in the radial direction. Note that the drop is always in one of the beam troughs, which is consistent with the constancy of the drop speed during the incoming phase. Decreasing γ/γ_F reduces the tethering length y_T by reducing the characteristic extent of the wave field [93]. The dependence of the scattering angle on drop size (Fig. A-16g) may be rationalised in terms of the fundamental wave slopes at the drop position as $\alpha \sim y_i/b \sim y_i(d\theta/dr) \sim (y_c/r)(v_\theta/v_r) \sim \nabla_\theta\eta/\nabla_r\eta$. By noting the negligible contribution to the azimuthal gradient from the well-induced wave field $\nabla_\theta\bar{\eta} >> \nabla_\theta\zeta$, one may readily show that $\alpha \sim \nabla_\theta\bar{\eta}/\nabla_r\eta$. Moreover, v_0 is proportional to $\nabla_\theta\bar{\eta}$, from which it follows that faster drops scatter more.

The mechanism responsible for the localised wavelike statistics is rooted in the enhanced (up to 30% in amplitude) concentric waves resonantly excited when the

drop crosses over the well (Fig. A-19c-iii). These resonant waves are spatially fixed and have a decay time $T_M^H \sim 2.5$ s signiffcantly larger than that of the waves in the shallow region $T_M^h \sim 0.6$ s, and also larger than the characteristic crossing time $\lambda_F/v_0 \sim 0.7$ s. The speed oscillations described in Fig. 3 are thus the result of the drop navigating this relatively persistent localised wave pattern as it exits the well (Fig. A-19c-iv,v). A 3D visualisation of the anomalous wave field is presented Fig. A-19d-f, including the complete time series of the perturbation at the drop location.

5.3 Discussion

The differences between the quantum [50, 25, 77, 87] and hydrodynamic [14] systems are vast: the typical defect size and particle speed in the macroscopic experiment are $\sim 10^8$ larger and $\sim 10^7$ slower than those in their microscopic counterpart. Nevertheless, we have demonstrated striking similarities. We have shown that a self-propelling walking drop interacting with a submerged well, a topographical defect in the medium, may lead to particle scattering and localised wavelike statistics. These two effects may be rationalised in terms of the markedly distinct dynamics arising as the particle approaches, and exits the well. The scattering angle is set during the incoming trajectory, in which the drop is deviated by a wave-mediated lift force induced by the well. While distant walkers are only weakly deviated, those sufficiently close are drawn into the well along an Archimedean spiral. The scattering mechanism is related to the emergence of a shifting beam-like wave perturbation between the drop and well. The drop speed along the incoming spiral trajectory is virtually constant; consequently, this phase does not contribute to the emergent wavelike statistics. As the walking drop crosses the well, it resonates with the wave-mode of the well, generating a standing wave field. These well-centred waves persist as the walker exits the well, leading to modulations in the drop speed responsible for the axially symmetric statistical signature. Our hydrodynamic pilot-wave system thus displays localised wavelike statistics strongly reminiscent of Friedel oscillations [50, 25, 77]. The decaying oscillations have half the Fermi wavelength in the quantum system,

and the Faraday wavelength λ_F in the hydrodynamic system, as corresponds to the wavelength of the drop's pilot wave.

The wavelike statistics reported here are fundamentally different from those previously observed in hydrodynamic corrals [65, 114]. The undulating statistical behaviour revealed in this study is localised to a finite region within an otherwise effectively open domain. Conversely, the wavelike statistics in corrals span the entire cavity, a closed domain. The underlying mechanisms are also markedly different. While the mechanism responsible for the emergence of quantum-like statistics in corrals is not yet entirely clear, it is thought to require chaotic pilot-wave dynamics rooted in the complex drop-wave-boundary interactions. Our study provides a clear mechanism for the emergent statistical behaviour: the oscillatory pattern emerges from speed modulations associated with the anomalously large waves excited due to a resonant interaction between the drop and the well, which acts as a localised region of high excitability. Our investigation thus demonstrates that chaos is not an indispensable ingredient for the emergence of wavelike statistics from hydrodynamic pilot-wave dynamics. In the context of hydrodynamic quantum analogs [14], our study constitutes an open system displaying wavelike statistical behaviour, thereby providing an alternative route for emergent quantum like behaviour in classical systems [65, 114, 49, 38, 103, 37, 24].

More broadly, our work has elucidated a wave-mediated interaction mechanism between a classical pilot-wave system and a topographical defect that gives rise to a modulated statistical signature surprisingly similar to that of an electron sea interacting with an atomic impurity [50, 25, 77]. An equivalent mechanism is unknown in the counterpart quantum system, where impurities are modelled as effective scattering potentials [47]. This work thus invites further mechanistic investigations and interpretations of other wave-mediated phenomena dealing with carrier mobility, such as localisation effects resulting from particle-impurity interactions within a collection of disordered defects [4] or particle-particle interactions such as those involved in metal-insulator transitions [74, 95].

Chapter 6

The walkers in a circular corral

In this chapter, we present the results of an experimental study of the dynamics and statistics of a walking droplet inside a circular bath, thereby deepening the connections between our system and quantum corrals. Particular attention is given to measuring the walker's instantaneous wave field using the free-surface synthetic Schlieren (FSSS) technique developed by Moisy *et al.* [91]. First, we measure the mean wave fields associated with the fundamental trajectories in the circular corral reported in chapter 4, noting their resemblance to the eigenstates of a quantum particle in a circular domain. Next, the influence of the of liquid height at the boundary of the cavity on its most unstable Faraday modes are investigated. We then present a technique for decomposing the wave field generated by a walking droplet into the normal modes of the cavity. This allows us to demonstrate that, just below the Faraday threshold, the instantaneous walker wave field is primarily characterised by two dominant modes, reminiscent of a two-level quantum system [19]. The first direct measurement of the system's mean wave field [114] is reported, and found to resemble the corral's most unstable Faraday mode. Our measurement of the mean wave field allows us to provide the first experimental test of a recently derived theoretical result [37] linking the mean wave field to the histogram of the drop's position. The main dynamical and statistical timescales associated with the motion of confined walking droplets are characterised and the effects of the droplet's bouncing phase on the emergent statistics discussed. Finally, we discuss a new dynamical mechanism for the emergent

statistics in the circular corral, rooted in modulations in the droplet speed along its path.

6.1 Introduction

The quantisation of orbits is prevalent in closed hydrodynamic quantum analogues owing to the dynamic constraint imposed on the droplet by its monochromatic wave field [81, 24]. Quantised orbits were first reported in experiments with a rotating bath as an analog of Landau levels [49, 62, 100, 102]. Droplets confined by a simple harmonic potential may lead to double quantisation in orbital radius and angular momentum, resembling the quantum eigenstates of quantum particles moving in the same potential [104, 103, 82, 36, 81].

A particularly robust hydrodynamic quantum analog has been drawn between droplets walking in confined geometries and electrons in quantum corrals, the details of which were discussed in chapter 2. At relatively low memories, periodic and quasi-periodic orbits arose [65]. At high memory Harris *et al.* [65] found that a coherent wavelike statistical behaviour, reminiscent of that of electrons in quantum corrals, emerges from the chaotic motion of walkers in a circular corral. The droplet's speed map showed concentric circular modulations with wavelength $\lambda_F/2$. The authors inferred that the histogram of the particle's location is related to the dominant Faraday mode of the cavity. The average speed map of the droplet showed that peaks in the histogram correspond to regions of lower speed. Harris *et al.* [65] proposed a dynamical mechanism for the emergent statistics in terms of chaotic switching between unstable periodic orbits, similar to that at play in orbital pilot-wave dynamics [49, 62, 100, 102, 104, 103, 36, 81].

Sáenz *et al.* [114] extended the study of Harris *et al.* [65] to the case of elliptical corrals. By averaging over grey-scale images (normal reflection of light) of the instantaneous droplet wave field, they obtained a qualitative measure of the form of the cavity's mean wave field. They demonstrated that this mean could be represented as the superposition of two dominant cavity modes; the most unstable Faraday mode

of the cavity and another mode arising at a slightly lower driving frequency. The weights in the superposition vary transiently: the wave field is generally a complex superposition of modes but in some instances resembles one of the two dominant Faraday modes. Finally, Sáenz *et al.* observed that the walker's position histogram is more strongly correlated with the mean wave field than with the dominant Faraday mode of the corral.

Cristea-Platon *et al.* [24] extended the work of Harris *et al.* [65], by investigating the dynamics of a walker inside a circular corral at relatively low memory. They reported a variety of stable dynamical states. The observed trajectories exhibited a double quantisation in angular momentum and orbital radius, reminiscent of that arising for walker motion in a harmonic potential [104]. In section 6.2.1 we calculate the mean wave fields associated with these periodic orbits.

Despite several attempts [121, 52, 53], a conclusive theoretical demonstration of the robust statistical behaviour of walkers inside corrals remains a challenge, owing in part to uncertainties in the outer boundary conditions [35]. The theoretical model of the hydrodynamic corral by Gilet [53] assumed Neumann boundary conditions. However, Blanchette [8] argued in favour of Dirichlet boundary conditions. Harris *et al.* [65] and Sáenz *et al.* [114] also assumed Dirichlet conditions in interpreting their experimental results. The influence of boundary conditions, specifically the outer layer depth, on the most unstable Faraday mode of a circular corral will be considered in section 6.2.2.

We proceed by revisiting the original experimental setup of Harris *et al.* [65] through quantitative measurement of the walker wave field. We perform the mode decomposition of the walker's instantaneous wave field in section 6.2.3. In section 6.2.4, we compute the mean wave field and evaluate the rate of convergence to this mean. The statistics of the droplet motion and their dependence on bouncing phase are explored in section 6.2.5. We provide the first experimental test of the convolution wave field result of Durey *et al.* [37] in section 6.2.6. In section 6.2.7, the mechanism responsible for the emergent quantum-like statistics is discussed.

6.2 Experiments

A schematic of the experimental set-up is shown in figure A-20. An acrylic circular cavity of diameter $D = 20.2$ mm and depth $H = 5.90 \pm 0.05$ mm is filled with 20 cSt silicon oil with density $\rho = 950$ kg m^{-3}, viscosity $\nu = 20.9$ cSt, and surface tension $\sigma = 20.6$ mN m^{-1}. A thin liquid film of depth $h = 0.22 \pm 0.03$ mm overlays the border of the cavity, acting as a wave damper [34]. The bath is vibrated vertically by a shaker with acceleration $\Gamma(t) = \gamma \cos(\omega t)$, where γ and $f = \omega/2\pi$ are the prescribed maximum acceleration and frequency, respectively. The experimental set-up is detailed in Harris *et al.* [63].

For all our experiments involving walkers, a droplet of the same silicon oil of diameter $d = 0.69 \pm 0.01$ mm was generated with a piezoelectric droplet-on-demand generator and placed on the vibrating bath with the help of a removable slide [64]. The droplet's position was acquired at 20 fps using a charge-coupled device (CCD) camera mounted directly above the bath in conjunction with an in-house particle location tracking algorithm [114]. To measure the wave field, we employed the free-surface synthetic Schlieren technique (FSSS), developed by Moisy *et al.* [91] and previously used by Eddi *et al.* [39] and Damiano *et al.* [29] to measure the surface deformations generated by a bouncer and a walker. The image acquisition was done at 19 frames per second with the same CCD camera arrangement.

6.2.1 Fundamental trajectories and their mean wave fields

We first compute the wave fields associated with the periodic trajectories reported by Harris *et al.* [65] and Cristea-Platon *et al.* [24]. The vibrational frequency was set to $f = 80$ Hz. The resulting Faraday threshold was $\gamma_F = 4.732 \pm 0.004$ g. Figure A-21a-e illustrates the periodic and weakly aperiodic droplet trajectories considered. We employed two different wave imaging techniques. The first is the qualitative grey-scale method (figure A-21f-j) developed by Douady [34] and employed by Sáenz *et al.* [114]. The second (figure A-21k-o) is the FSSS [91], which yields a direct quantitative measurement of the wave amplitude throughout the corral [29]. Using

both methods, we compute the mean wave fields by averaging over one period of the periodic trajectories.

The circular trajectories in figures A-21a,b have associated azimuthally symmetric mean wave fields (figures A-21f,g,k,l). Different orbital radii may lead to the mean wave fields being out of phase with one another, as evident in figures A-21k,l. The dark centre in figure A-21f indicates that the instantaneous wave field of the droplet executing a small circle displays a node at the origin, as was reported for walker motion in the harmonic potential [104]. The mean wave fields evident in figures A-21h,i,j display different rotational symmetries of order 2, 3, and 4, mirroring the symmetries in the lemniscate, trefoil, and papillon respectively (figures A-21c,d,e). These wave fields resemble the eigenstates of a particle in a quantum circular domain and their radial and azimuthal modulations suggests similar quantisations to the radial and azimuthal quantum numbers [19].

6.2.2 Influence of the outer depth h on Faraday wave modes

Following the treatment of Benjamin and Ursell [7], the amplitude of the Faraday patterns in a circular corral can be expanded in terms of the complete orthogonal set of eigenfunctions u_{mn}. These eigenfunctions are the solutions to the two-dimensional Helmholtz equation in polar coordinates (r, θ):

$$\left(\frac{\partial^2}{\partial r^2} + \frac{1}{r}\frac{\partial}{\partial r} + \frac{1}{r^2}\frac{\partial^2}{\partial \theta^2} + \lambda^2\right) u = 0 \tag{6.1}$$

for $0 \leq r < a$, $0 \leq \theta \leq 2\pi$, where a is the radius of the circular corral. A solution to the above equation, with Dirichlet boundary conditions, $u = 0$, at the corral edges, $r = a$, can be obtained via separation of variables:

$$u_{mn}(r, \theta) = J_m(\lambda_{mn} r)\left(A\cos(m\theta) + B\sin(m\theta)\right) \tag{6.2}$$

where $m \in \mathbb{N}$, $n \in \mathbb{N}^*$, J_m is the Bessel function of the first kind, λ_{mn} is the n-th positive root of J_m divided by a, and A and B are constants. These circular cavity

modes provide the basis for the wave modes observed in our experiments.

We proceed by exploring the effect of outer boundary conditions on the Faraday modes for an aluminium circular corral of diameter $D = 2a = 28.5$ mm and depth $H = 6.28 \pm 0.03$ mm. The dominant Faraday instabilities, at $\gamma = \gamma_F$, are illustrated in figures A-22 and A-23 for the shaker frequency of $f = 65$ Hz and 70 Hz for three values of the thin outer liquid film depth, $h = 0.05, 0.50, 1.00 \pm 0.03$ mm.

Our results demonstrate that the Faraday patterns emerging at $f = 65$ Hz and $f = 70$ Hz converge to the Dirichlet modes (3,6) and (6,0), respectively, as the liquid height h decreases. For the smallest liquid depth considered, $h = 0.05$ mm, shown in figures A-22c and A-23c, we notice a good agreement with the modes given by eq. (6.2) and illustrated in columns d. A comparison of the radial wave profiles in figure A-23 is shown in figure A-24. The differences arise from the Faraday pattern appearing stretched in the radial direction and having a smaller rate of amplitude decay, relative to the analytical solution. The possible reason for this disagreement is the deviation from Dirichlet boundary conditions at the outer-'beach', although Neumann boundary conditions do not lead to a better agreement (see figure A-24).We note that while the boundary conditions significantly influence the Faraday mode present at 65 Hz (see figure A-22), they appear to have limited effect on the azimuthally symmetric mode occurring at 70 Hz (see figures A-23 and A-24).

6.2.3 Wave decomposition in the circular corral

We next compute the instantaneous pilot wave field and decompose it into the cavity's normal modes. The thickness of the outer depth was set to $h = 0.22 \pm 0.03$ mm, the corral's diameter $D = 28.5$ mm, and the driving frequency $f = 70$ Hz. For the range of parameters considered, $\gamma_F = 3.875 \pm 0.004$ g and $\lambda_F = 5.275$ mm. We focus on the high-memory regime, $\gamma/\gamma_F = 0.995$. The system is then effectively closed as the 'memory' time $T_M \sim 3.5$ s, exceeds the droplet's characteristic crossing time $T_c = D/2u \sim 1.7$ s, where $u \sim 8\text{mm s}^{-1}$ is the characteristic speed of the droplet. The instantaneous wave field as well as the particle's position are recorded. In figure A-25a, the droplet's recent trajectory is overlaid on the instantaneous wave

field. Note that the instantaneous wave field is markedly different from both the distinct horseshoe shape arising for a free walker [39] and from the circular corral's most unstable Faraday mode, whose form is evident in figure A-23c. Furthermore, the droplet motion is highly irregular, as is characteristic of the high-memory regime [65, 114, 24].

We developed an in-house mode-decomposition algorithm in order to determine the underlying mode superposition associated with the recorded wave field. The instantaneous wave field, $\eta(r,\theta)$, is decomposed into a weighted sum of the terms like those in eq. (6.2), with the individual weights given by the inner product:

$$w_{mn} = \int_0^{2\pi} \int_0^a \eta(r,\theta) u_{mn}(r,\theta)\, \mathrm{d}r\, \mathrm{d}\theta \tag{6.3}$$

where w_{mn} is the weight of mode u_{mn}. The 5 dominant modes of the instantaneous wave field shown in figure A-25a are plotted in figure A-25b. As the instantaneous wave field is relatively complex, the significance of multiple modes is expected.

As did Sáenz *et al.* [114], we notice that the instantaneous wave fields can sometimes resemble a single cavity mode. We illustrate such occurrences in figures A-26 and A-27. Figure A-26a shows an instantaneous wave field resembling the corral's most unstable Faraday mode (see figure A-23c) as well as the azimuthally symmetric mode $(6,0)$ (see figure A-26b). Figure A-27a depicts an instantaneous wave field arising in the same experiment that is well approximated by the non-azimuthally symmetric mode $(5,2)$ (see figure A-27b). More generally, several modes contribute to the instantaneous pilot-wave field.

We recorded 36,000 instantaneous wave fields, resulting from the droplet's chaotic trajectories, and decomposed them into their dominant modes. The resulted distribution of the cavity-modes obtained is indicated by the blue histogram in figure A-28. The mode number represents the order index of modes with increasing eigenvalue. Notice the dominant peak at the azimuthally symmetric mode $(6,0)$ and the secondary peak at the non-azimuthally symmetric mode $(5,2)$. This suggests that the droplet's motion is dominated by two underlying cavity modes, with time dependent

weights. Furthermore, the $(6, 0)$ mode resembles the mean wave fields of the circular trajectories (see figure A-21k,l), while the $(5, 2)$ mode evokes a superposition of the mean wave fields of the trefoils and papillons (see figure A-21n,o). These observations align with the mechanism originally proposed by Harris *et al.* [65], that the wave-like statistical pattern in the corral reflects the intermittent switching between fundamental trajectories.

6.2.4 The mean wave field

We obtain the evolution of the mean wave field by computing a running average of the strobed FSSS-inferred instantaneous wave field (see figure A-29). Figure A-29a shows that after 5 minutes, a central maximum becomes apparent. The concentric rings begin to appear after 15 minutes (see figure A-29b) and azimuthal asymmetries are diminished after 25 minutes (see figure A-29c). A well-defined mean wave field is revealed after 30 minutes (see figure A-29d) and its features are strikingly similar to those of the cavity's Faraday mode, shown in figure A-23c. We note that the mean wave field converges with time, the exponential decay time being $\sim 150\ T_M$, as can be seen in figure A-29e,f,g,h, with its radial profile displaying, as expected, a decrease in exponential decay time, $\sim 80\ T_M$ (see figure A-29i). We conclude that the convergence time of the mean wave field is 30 minutes $\sim 500\ T_M$.

The azimuthal symmetry of the mean wave field is also apparent in the corresponding mode-decomposition distribution, illustrated by the red histogram in figure A-28. Notice that while the $(6, 0)$ mode is once again evident, the non-azimuthally symmetric mode $(5, 2)$ is absent. The rotational symmetry of the circular corral evidently leads to the destructive interference of non-azimuthally symmetric modes. This mechanism elucidates the resemblance of the mean wave mode to the corral's most unstable Faraday mode, both here and in the original corral experiments of Harris *et al.* [65].

6.2.5 Droplet statistics

We proceed by evaluating the rate of convergence of the walker position histogram and average speed map. Figures A-30a and A-31a show that after 5 minutes, no clear patterns can be distinguished in either. Central features become apparent after 30 minutes (see figures A-30b and A-31b) and pronounced concentric rings occur after 60 minutes (see figures A-30c and A-31c). Azimuthal asymmetries are further diminished after 180 minutes when a converged position histogram and associated speed map emerge (see figures A-30d and A-31d). The statistical convergence is visually manifested via the decreasing amplitude of difference plots shown in figures A-30e,f,g,h and A-31e,f,g,h, respectively. As expected, the radial profiles of the histogram and average speed map show a decrease in exponential decay time, ~ 220 T_M and ~ 450 T_M, respectively, compared to their two-dimensional representations, ~ 310 T_M and ~ 530 T_M, respectively, (see figures A-30i and A-31i, respectively). We thus obtain the statistical steady-state convergence time in the circular corral to be 180 minutes, ~ 3000 T_M, an order of magnitude larger than the convergence time of the mean wave field. We point out that Harris *et al.* [65] computed the walker position histogram over only 30 minutes, ~ 500 T_M, while Sáenz *et al.* [114] used 210 minutes, ~ 3600 T_M, and this study used 195 minutes, ~ 3300 T_M.

The effects of variability in the walker bouncing phase complicate our theoretical understanding of the hydrodynamic corral [35]. The presence of two-mode droplet statistics observed by Sáenz *et al.* [114] suggests that the impact phase of the droplet relative to the liquid's surface might be selectively exciting an *in-* or *out*-of-phase wave field (see figure A-32). This indicates the possibility of the walker's motion giving rise to two very different statistics depending on the wave field's phase at the time of impact. In the high-memory regime, $\gamma/\gamma_F = 0.995$, we observed an even split, $44 - 56\%$, in the distribution of the droplet's impact phase, with phase changes occurring on average every 7 seconds, ~ 2 T_M. However, the two phase-differentiated position histograms were indistinguishable from that reported in figure A-30d.

Just above the Faraday threshold, the corral's background wave field is exter-

nally imposed and so might potentially alter the particle statistics. Nevertheless, the statistics of the corralled walker at $\gamma/\gamma_F = 1.004$ (see figure A-33), showed minimal differences from those observed at $\gamma/\gamma_F = 0.995$ and were similarly independent of the droplet's bouncing phase. Further increasing the memory above $\gamma/\gamma_F = 1.004$ led to the liquid inside the corral spilling onto the outer-'beach', precluding the convergence to a statistically steady state.

6.2.6 Relation between the particle histogram and the mean wave field

Durey *et al.* [37] proved that, for infinite domains, the mean wave field created by a walking droplet is equal to the convolution between the wave field of a stationary bouncing droplet, $B(r)$, and the statistical histogram of the droplet position, $\mathcal{H}(r,\theta)$. The convolution wave field, $C(r,\theta)$, is prescribed by:

$$C(r,\theta) = B(r) * \mathcal{H}(r,\theta) \tag{6.4}$$

We here test relation (6.4) in a circular domain. The bouncer wave field (see figure A-34a) used in the convolution (6.4) has an analytical form [20]:

$$B(r) = AJ_0(k_F r)\left[1 + \left(\xi K_1\left(\xi k_F r\right) k_F r - 1\right) e^{-(k_F r)^{-2}}\right] \tag{6.5}$$

where $A = 1.65$ mm, $k_F = 1.19$ mm^{-1}, $\xi = 1.36 \times 10^{-4}$, J_0 is the Bessel function of the first kind of order zero and K_1 is a spatial damping function [20].

Figure A-34b illustrates the radial dependence of the droplet's position histogram and in figure A-35 we compare the convolution wave field to the mean wave field. We obtain a fair agreement between the two wave fields throughout the corral, despite our geometry being closed. We expect discrepancies near the boundaries because the corral is not an infinite domain and the boundaries will lead to the bouncer wave field being dependent on the droplet's location, $B(r,\theta)$, and damped near the outer boundaries. The agreement could be improved by using the more sophisticated

version of Durey *et al.*'s result that accounts for the corral boundary conditions [35].

6.2.7 A dynamical mechanism for the emergent statistics

Speed modulations occurring along the particle's trajectory were recently found to be significant in understanding the hydrodynamic analogue of Friedel oscillations [115]. They are also apparent in our corral experiments, and may play a key role in the form of the emergent statistics. Figure A-36 shows the trajectory of the walker colour-coded according to speed, for time intervals of increasing duration: 15 and 60 seconds, 2 and 8 minutes, and 3 hours. A well-defined pattern emerges after 3 hours, revealing a correlation between drop position and speed (see figure A-36e), similar to that reported in the original experiments by Harris *et al.* [65]. The average spacing of the speed modulations along the droplet's trajectory is $\sim 0.8\lambda_F$ (see figure A-37) and the circular bands of high droplet speed observed in figure A-36e are spaced at $\sim 0.5\lambda_F$ intervals.

As the droplet approaches the corral's border, it is typically deflected with what appears to be a preferred angle (see figure A-36d). Pucci *et al.* [109] reported that walkers incident on a submerged wall have a tendency to be reflected at $\sim 60°$ independent of their incident angle. This preferred reflection angle leads the radial projection of the speed oscillations along the droplet's trajectory to have wavelength $\sim 0.5\lambda_F$, as is consistent with the speed maps reported by Harris *et al.* [65] and shown in figures A-36e and A-31d. The speed variations necessarily give rise to a signature in the droplet's position histogram, with the same wavelength $\sim 0.5\lambda_F$. Thus the droplet speed modulations along its trajectory combined with the peculiar non-specular reflection of walkers (see figure A-38) may play a significant role in the observed statistical modulations in the corral. [1]

[1] Coincidently, the theoretical treatment of quantum corrals describes the oscillations in the number density of electrons as arising from the constructive interfering of scattered waves from the border [47].

6.3 Discussion

We have reported the results of an experimental investigation of walker motion in a hydrodynamic corral, giving particular attention to a characterisation of the wave dynamics. Specifically, the instantaneous and mean wave fields accompanying periodic and chaotic motion were measured and decomposed into the Faraday modes of the cavity. Our study also allowed us to characterise the influence of boundary conditions on the wave modes of the cavity. As the liquid height decreases, the Faraday modes resemble more closely pure vibration modes of a circular membrane attached at the edge. We demonstrate the negligible influence of a binary bouncing phase on the walker statistics. Finally, our research gave us new insight into the emerging statistics in the hydrodynamic corral.

In the chaotic regime, the droplet's instantaneous wave field typically contains two dominant wave modes: the first closely resembling the most unstable Faraday mode of the corral, and the second being a non-azimuthally symmetric Faraday mode dominant at a lower vibrational frequency. By averaging the strobed walker wave field, we provide the first quantitative measurement of the mean wave field. Its azimuthally symmetric form and its striking resemblance to the cavity's dominant Faraday wave mode, indicate that the influence of non-axially symmetric modes is averaged out. We expect that the emergence of rotationally invariant mean wave fields is a general property of the circular corral, consistent with the statistical form reported by Harris *et al.* [65].

The wave-like statistics in the circular corral shows azimuthal symmetry with radial oscillations of $0.5\lambda_F$ wavelength, a robust result that occurs within 0.005% of the Faraday threshold. We provided the first experimental test of the theoretical link formulated by Durey *et al.* [37] between the mean wave field and the statistically steady state of the droplet position histogram. The observed agreement is fair and the validation of a convolution wave field that incorporates the influence of the corral boundaries will be the subject of further experimental and theoretical inquiries.

In the circular corral, the speed oscillations of wavelength $\sim 0.8\lambda_F$ along the

droplet's trajectory combined with the non-specular reflection law [109], result in radial speed modulations of $\sim 0.5\lambda_F$ spacing. The latter necessarily lead to a signal in the drop histogram with the same wavelength $\sim 0.5\lambda_F$. We thus propose a new dynamical mechanism for the observed statistical modulations in the corral that may find broader applications in hydrodynamic quantum analogues.

We conclude by reviewing the physical analogy between the hydrodynamic and quantum corrals that has emerged from this and prior studies. The bouncing timescale, $T_F \sim 0.02\ T_M \sim 0.03$ seconds, plays the role of the vibration period of the Compton timescale, τ_C, in de Broglie's mechanics, as outlined in chapter 2. The instantaneous pilot-wave field is similar to that envisioned by de Broglie [14]. The crossing time, $T_c \sim D/v \sim 0.5\ T_M$, describing the period between consecutive walker-wall interactions is analogous to the classical period the τ_p in semi-classical quantum mechanics [112]. Similarly, the statistical convergence timescale, $T_s \sim 3000\ T_M \sim 180$ minutes parallels the statistical relaxation timescale τ_s [112]. The convergence timescales of the mean wave field, $\sim 500\ T_M$, does not have an evident counterpart in quantum mechanics. We expect the value of the convergence time scales to be of interest to experimentalists working in the field of hydrodynamic quantum analogues.

Chapter 7

Conclusions

It seems a little paradoxical to construct a configuration space with the coordinates of points which do not exist. - Louis de Broglie [5]

In this thesis, we have explored walking droplets in both closed and open geometries through consideration of hydrodynamic analogues of the quantum corral and Friedel oscillations. A one-sentence summary of this thesis would be the following:

The notion of particle trajectories is not inconsistent with the statistical behaviour evident in quantum corrals and Friedel oscillations, if one adopts a pilot-wave dynamics of the form proposed by de Broglie in conjunction with the Ensemble Interpretation of quantum mechanics.

We started by investigating the walking droplets confined to elliptical cavities. Building upon the earlier work of Harris *et al.* [65], we characterised the emergence of coherent walker statistical forms that can be characterised in terms of a small number of normal modes of the cavity. We also reported a new statistical projection effect due to a submerged well placed at one of the foci. Specifically, we demonstrate that bottom topography may lead to preferential mode selection: when the well is placed at one of the foci of the cavity, the particle position distribution displays overdensities perpendicular to the major axis of the ellipse, an effect reminiscent of the quantum mirage effect [87, 94]. We also presented a qualitative measure of a mean

wave field, and noted the similarity between its form and that of the statistical wave form describing the drop position. We further demonstrated that this mean wave field may be decomposed into two cavity modes, one being the cavity's dominant Faraday pattern and the other being a mode prevalent at a nearby frequency. The instantaneous wave field switches between two dominant cavity-modes, reminiscent of a time-dependent superposition of two quantum states [19]. A similar switching of dynamical states was reported previously in orbital pilot-wave hydrodynamics, for example, walker motion in a rotating frame [49, 62, 100, 102] or walker motion in a simple harmonic potential [104, 103, 82, 36, 81], where a walker would switch chaotically between periodic and quasi-periodic trajectories.

In chapter 4, we characterised the emergence of periodic and quasi-periodic trajectories of walkers confined to circular corrals. In the low and intermediate memory regimes, the droplet executes simple periodic trajectories such as circles, lemniscates, trefoils, and papillons. Each such path has distinct speed modulations and an associated mean wave field, the form of which was measured quantitatively in chapter 6. Associated with the periodic orbits is a double quantisation in orbital radius and angular momentum resembling that arising for walking droplets confined by a harmonic potential [104, 36, 81]. This similarity suggests a common origin of the quantum-like behaviour emerging in all closed hydrodynamic quantum analogues.

In chapter 5, we explored the first successful open hydrodynamic quantum analogue, that of Friedel oscillation from a topographical defect. Specifically, we considered the interaction of a walker with a submerged well. If the droplet's spatially extended wave field has a sufficiently large amplitude above the well, it triggers a self-excited wave beam, spanning the droplet and the well, that guides the particle towards the well along an Archimedean spiral. As the walker passes over the well, it generates a standing wave field centred on the well that leads to speed modulations in the droplet's outgoing rectilinear trajectory. These speed modulations have a characteristic wavelength of λ_F, the result being a particle position histogram with radial modulations with the same wavelength. In the quantum equivalent, the electron sea around an electrically charge impurity has a statistical distribution of the

same form, with spacing given by half the Fermi wavelength. Our analysis shows that a rational dynamics underlying the statistical Friedel-like oscillations is indeed possible. Ongoing research has suggested that, in the high memory regime, perturbed free walkers display decaying oscillations in droplet speed, with characteristic wavelength of λ_F [127]. Thus, speed modulations might be a generic mechanism for the emergent quantum-like statistics in pilot-wave hydrodynamics. The possibility of particle trajectories underlying quantum mechanics would seem far less distant.

In chapter 6, we explored the high-memory regime for the circular corral, where chaotic walker dynamics arises. The droplet's position histogram and complementary speed map are circularly symmetric, showing radial oscillations of wavelength $0.5\lambda_F$. The former bears a strong resemblance to the particle density function of an electron inside a circular quantum corral, where statistical modulations arise on the de Broglie length scale. We performed a direct measurement of the mean wave field and were thus able to provide the first experimental test of the convolution result derived by Durey *et al.* [37]. The chaotic motion of the corralled droplet shows speed modulations with average spacing $\sim 0.8\lambda_F$, arising from the walker-wall interaction. Following the reflection off the border, the droplet's trajectory follows preferred angles that are roughly consistent with the $\sim 60^\circ$ non-specular reflection angle reported by Pucci *et al.* [109]. The combination of these two wall-mediated effects give rise to the radial speed oscillations of wavelength $\sim 0.5\lambda_F$, consistent with our speed map. The alternating regions of slow and fast speeds produce the emergent wave-like statistics in the droplet's position histogram, with characteristic spacing $0.5\lambda_F$. This represents a new potential dynamical mechanism underlying the quantum-like statistics in the hydrodynamic corral, one that may find wider relevance in hydrodynamic quantum analogues.

There is no dynamical explanation for the emergent wave patterns in the electron sea observed in quantum corrals, only a statistical description. Our work suggests three possibilities for the dynamical roots of the wave-like statistical pattern emerging in the hydrodynamical corrals. The first treats the cavity as an effective harmonic potential for the droplets, which move along periodic and quasi-period partial tra-

jectories, switching intermittently between them [65]. This mechanism mirrors the description provided in the semi-classical periodic-orbit theory [58] of quantum corrals, where the electrons are modelled as wave-packets moving along a multitude of classical billiard trajectories. The second candidate views the mean wave field inside the hydrodynamic corral as an effective potential felt by the droplets. Notably, the convolution law of Durey *et al.* [37] provides a direct link between this wave field and the droplet's position statistics, suggesting that the mean wave field plays a role similar to the quantum potential in Bohmian mechanics. The third possibility considers the border reflection as inducing a Friedel-like speed modulation and preferred outgoing trajectory angle, leading to a modulation in the particle histogram that propagates inwards from the walls of the corral. Notably, these three dynamical scenarios for the origins of quantum-like statistics in the hydrodynamic corral are not mutually exclusive, and may all be significant.

7.1 Future directions

Our work motivates several further studies of open pilot-wave systems, such as Friedel-like oscillations from a submerged border (see figures A-39a,b) and a submerged pillar. The first would represent the analogue for the Friedel oscillation from a wall. Preliminary results depict a $\sim$60° non-specular reflection angle and speed modulations of wavelength $\sim \lambda_F$ (see figure A-39c) along the droplet's outgoing trajectory. Following $\sim$ 300 walker-wall interactions, we notice the emergence of speed modulations with $\sim 0.5\lambda_F$ spacing (see figure A-39d), showing a striking resemblance to its quantum counterpart. The submerged pillar could lead to speed modulations of Faraday wavelength [127] along the droplet's outgoing spiral trajectory [60]. This behaviour could then give rise to *gallery modes* [96, 111] in the walker's statistics, as the oscillations would occur azimuthally, rather than radially as was the case in the Friedel analogue reported in chapter 5.

This thesis also suggests a revisitation of the notorious walker diffraction experiment [21, 3, 108], however, with the following modifications. First, as the walk-

ing droplet system is dissipative, something negligible in typical optical or quantum diffraction experiments, we propose an investigation of the equivalent of the near-field Fresnel diffraction [13] instead of the previously explored far-field Fraunhofer diffraction [21, 3, 108]. Second, the slits used should reinforce rather than damp the coherent wave field of the walker, and hence act as exciters. We propose the use of submerged wells, on the grounds that the beaming wave field observed in our analogue to the Friedel oscillations had a relatively large radial extent and a slow decay time. We would also like to encourage the use of a *physical* experimental set-up when performing this investigation in favour of a *Gedankenlaboratorium* [3]. The fundamental appeal of the hydrodynamic quantum analogue system is that it represents a new experimental platform for exploring quantum like behaviour. Hence, predictions can be checked experimentally, precluding the need for *thought experiments*.

Appendix A

Figures

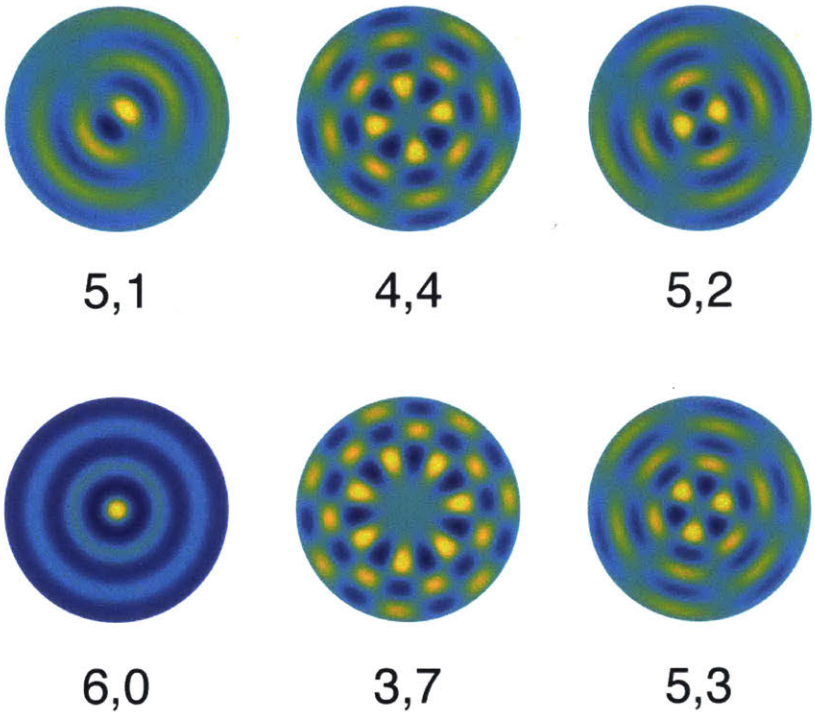

Figure A-1: Examples of quantum eigenmodes of the two-dimensional circular box. The modes are identified by the their associated quantum numbers n_r, n_θ and listed in order of increasing energy levels, as defined in eq. (2.9), left to right and top to bottom.

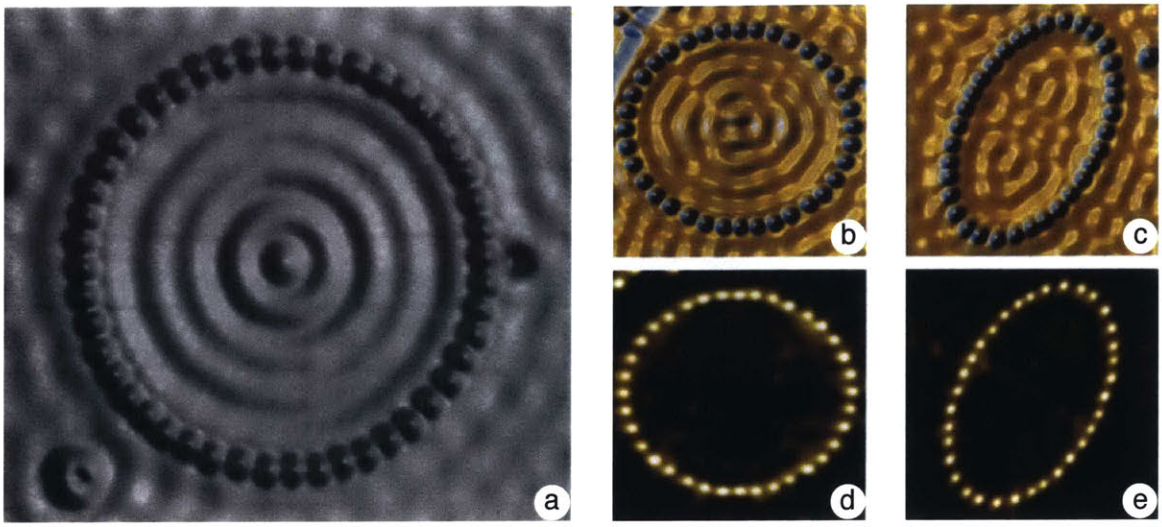

Figure A-2: (a) STM topographic image of the electron sea density in and around a quantum corral made up of 48 Fe atoms in a ring assembled on Cu(111) surface. Notice the eigenstate pattern inside the corral. The diameter of the ring is 142.6 Å and the ring encloses a defect-free region of the surface [25]. (Copyright 1993 by AAAS) Elliptical electron resonators built using Co atoms to corral two-dimensional electrons on Cu(111). (b-c) Topographic measurements of the standing wave patterns in the electron sea. (d-e) Differential conductance maps acquired simultaneously [87]. (Copyright 2000 by Nature Research)

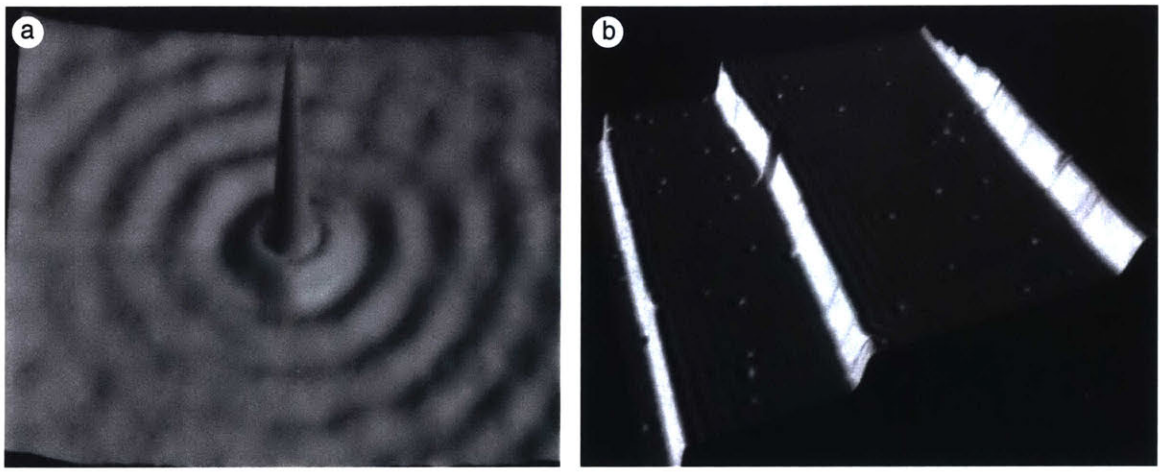

Figure A-3: (a) STM topographic 130 Å × 130 Å image of an electron sea density in the vicinity of an Fe adatom on the Cu(111) surface. The concentric rings, called Friedel oscillations, around the impurity are standing waves generated by the scattering of the surface state electrons by the Fe adatom [25]. (Copyright 1993 by AAAS) (b) STM topographic 500 Å × 500 Å image of an electron sea density at the Cu(111) surface. Three mono-atomic steps are visible along with $\sim$ 50 point defects. Spatial oscillations, Fridel oscillations, with a wavelength of $\sim$ 15 Å are apparent near the steps and in the vicinity of impurities [26]. (Copyright 1993 by Nature Research)

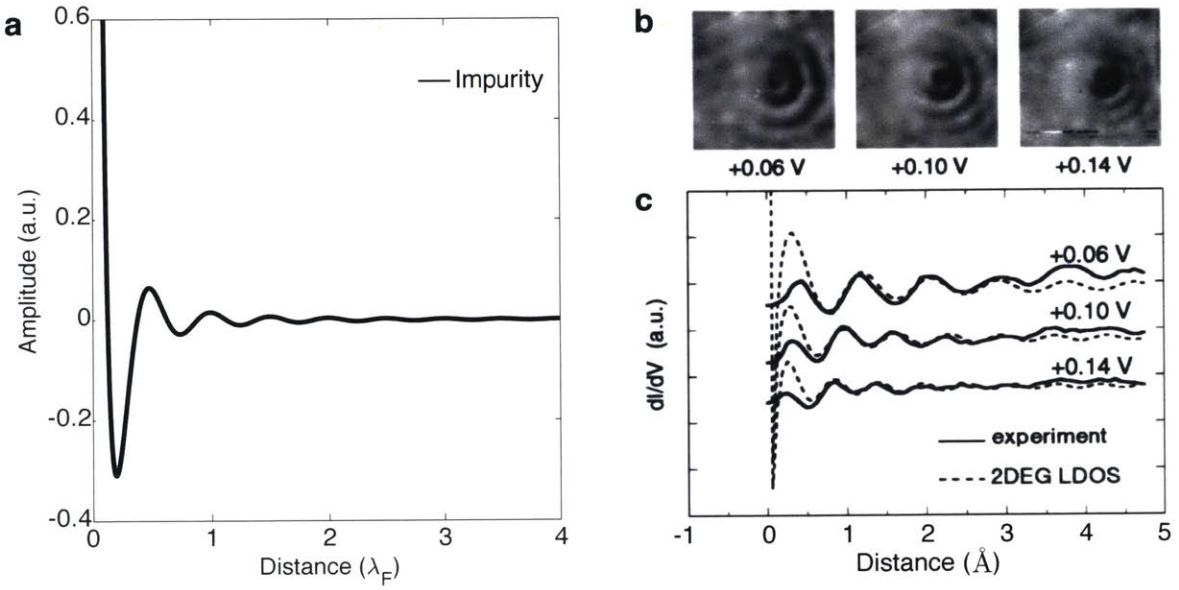

Figure A-4: (a) Theoretical computations of Friedel oscillations arising in a two dimensional electron gas due to a localised impurity. Notice the half Fermi wavelength characterising both modulations. (b) dI/dV images of the Friedel oscillation around a point scatterer in a 67 nm $\times$ 67 nm area as a function of energy (bias voltage). Notice the different wavelengths of the oscillations. (c) The experimentally obtained oscillations in (b) compared to the theoretical two-dimensional electron gas from (a)) [77]. (Copyright 2001 by American Physical Society)

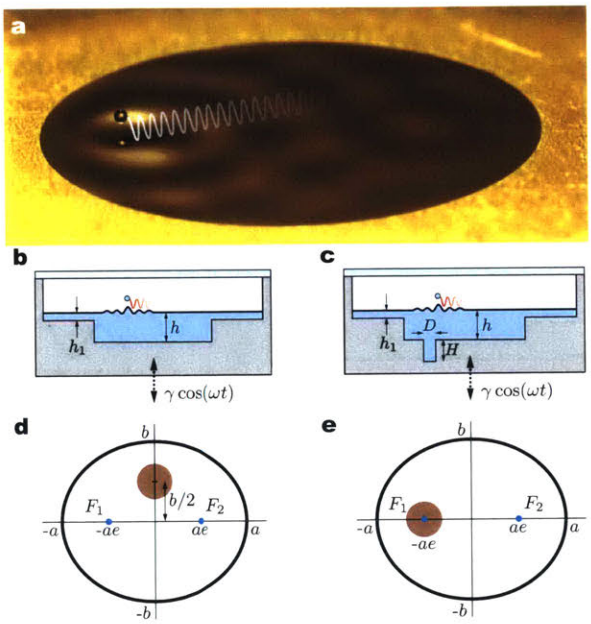

Figure A-5: Schematic of the experimental set-up. **a**, Oblique view of a droplet and its pilot wave exploring an elliptical corral. **b**,**c**, Cross-section of the topologically homogeneous elliptical corral (**b**) and the elliptical corral with a submerged circular well of depth $H = 4.5$ mm and diameter $D = 5.5$mm (**c**). The liquid depth in the corral and in the wave damper is $h = 1.70$ mm and $h_1 = 0.05$ mm, respectively. **d**,**e**, Location of the circular well corresponding to the results presented in the left and right columns of Fig. A-9. The length of the semi-major axis and eccentricity of the ellipse are $a = 14.25$ mm and $e = \sqrt{1 - b^2/a^2} = 0.5$, respectively.

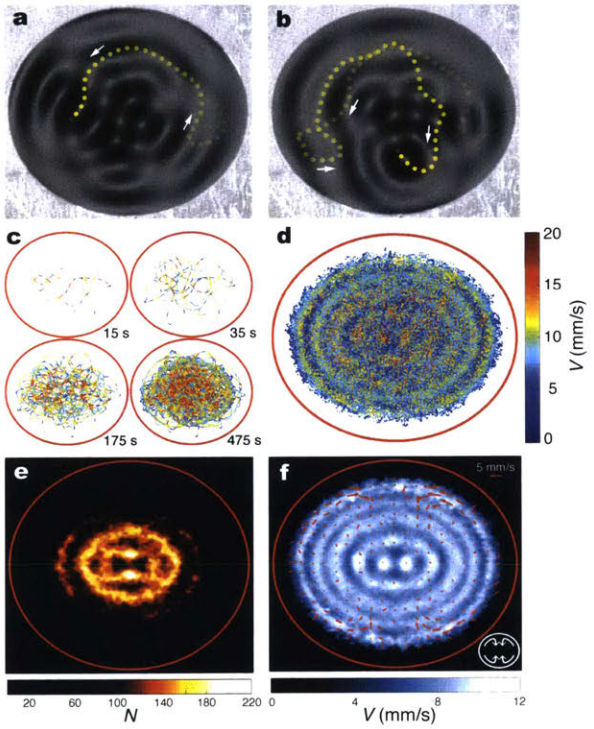

Figure A-6: Droplet statistics in an elliptical corral. **a**,**b**, Top views illustrating the complex instantaneous wave field excited by the drop's motion along the yellow dashed trajectory. **c**, Chaotic droplet trajectory, coloured according to the instantaneous speed, for increasing time intervals. **d**, Emergent pattern after 3.5 h. **e**, Histogram of the walker's position (90×90 bins). **f**, Local average speed (contour plot) and velocity (arrows) for the data shown in **d**. The absolute average speed is $< u > 8.68$ mm s^{-1}. Here, $f = 72$ Hz, $\gamma/\gamma_F = 0.998$ and $d = 0.79 \pm 0.01$ mm, for which the most unstable Faraday wave mode is the $(1, 5)$ mode illustrated in Fig. A-7c,d.

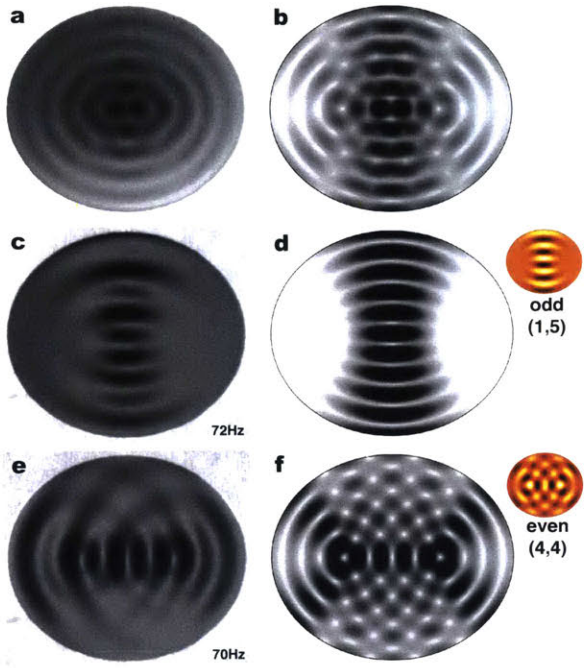

Figure A-7: Mean pilot-wave field. **a**, Mean pilot-wave field obtained by averaging the instantaneous waves, such as those shown in Fig. A-6a,b, over 30 min. Note that at the prescribed acceleration ($\gamma < \gamma_F$), no waves would exist in the absence of the drop. **b**, Superposition of the analytical gradient maps presented in **d** and **f**, showing good agreement with the mean wave pattern (**a**) and so the walker's statistical response (A-6e,f). **c**,**e**, Faraday waves observed at threshold $\gamma = \gamma_F$ with $f = 72$ Hz (**c**) and 70 Hz (**e**). **d**,**f**, The patterns in **c** and **e** are well approximated by the two analytical eigenfunctions in **d** and **f**, respectively, which correspond to solutions of the Helmholtz equation in an elliptical domain with Dirichlet boundary conditions. In **d** and **f**, right, the eigenmodes are depicted in bright colours, while the greyscale figures show the magnitude of their spatial gradients, with white corresponding to zeros in slope (extrema or saddle points) and black corresponding to extrema in slope. This depiction allows for a direct comparison between the analytical modes and experimental visualisation of the waves [34].

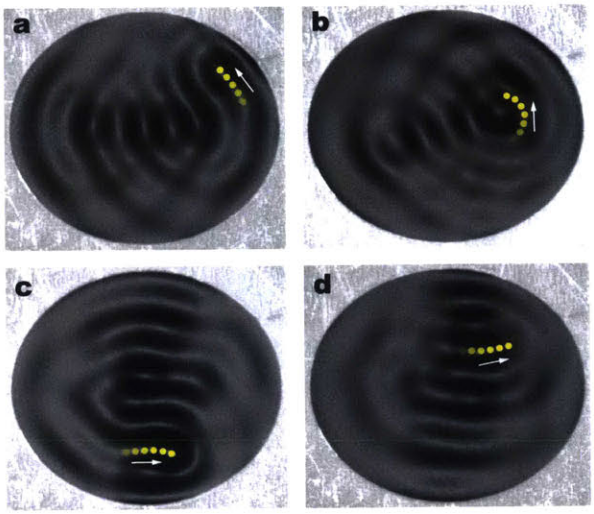

Figure A-8: Fundamental modes of the elliptical corral transiently excited by the walker. On rare occasions when the walker's trajectory coincides with one of the crests or troughs of the fundamental Faraday modes for an extended period, a pilot-wave form resembling the corral's fundamental Faraday modes may briefly appear. **a**,**b**, The $(4, 4)$ Faraday mode dominant at 70 Hz emerges in the bath. **c**,**d**, The $(1, 5)$ Faraday mode dominant at 72 Hz becomes apparent. The yellow dotted line illustrates the droplet's trajectory. Here, $\gamma/\gamma_F = 0.998$ and $f = 72$ Hz.

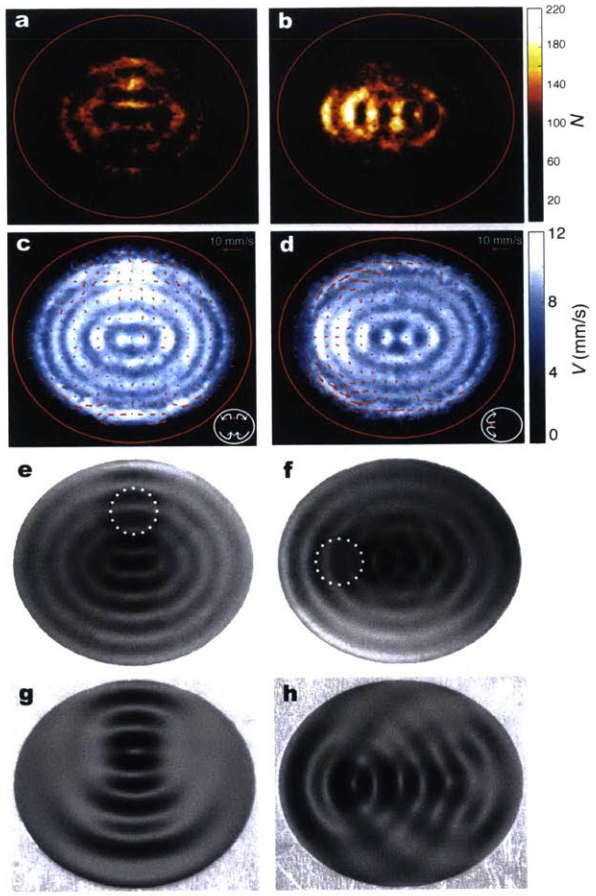

Figure A-9: Resonant projection effects. **a-f**, Walker's histogram (**a**,**b**), average speed (colour map) and average velocity (arrows) (**c**,**d**) and mean wave field (**e**,**f**), arising when a submerged circular well is placed at the midpoint of the upper semi-minor axis (left column) or the left focus (right column). The well's diameter and depth are $D = 5.5$ mm and $H = 4.5$ mm, respectively, and its specific locations are indicated in **e** and **f**. The experimental parameters are as in Fig. A-6. When the well is off focus (**a**), the resonance of the fundamental modes is notably obstructed: the histogram only shows traces of the statistical signature observed within a homogeneous corral (Fig. A-6e). Conversely, when the well is at the focus (**b**), the resonance of the $(4, 4)$ mode is drastically enhanced, leading to a radical change in the walker's statistical behaviour, now characterised by high-density vertical bands projected towards the empty focus. This resonant effect is also evident in the corresponding average speed and average velocity maps (**c**,**d**), which show the emergence of substantially stronger mean velocities when the well is at the focus. In **e** and **f**, the mean pilot-wave field is shown averaged over 30 min, showing reinforced horizontal (**e**) and vertical (**f**) bands with respect to Fig. A-7a due to the effects of the well. **g**,**h**, Faraday waves observed at threshold $\gamma = \gamma_F$ with $f = 72$ Hz when a submerged well is placed as in **e** and **f**. In both cases, the well induces waves markedly different from those observed at the same f with homogeneous topography (Fig. A-7c). Specifically, the well at the focus enhances the $(4, 4)$ mode observed at 70 Hz in the absence of the well (Fig. A-7e).

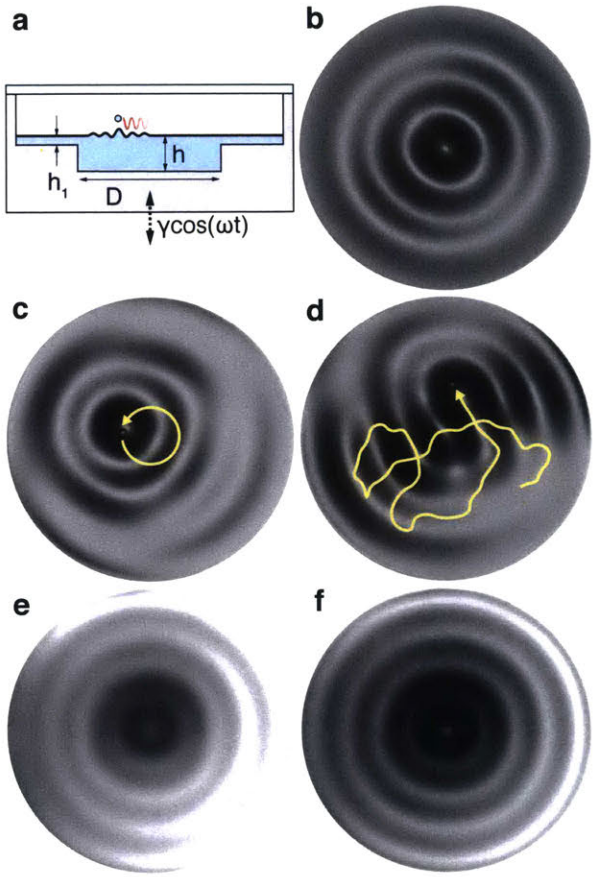

Figure A-10: Experimental setup [65]. **(a)** Cross-sectional view of the circular corral filled with silicon oil. **(b)** Faraday wave pattern obtained for the circular corral driven at $f = 80$ Hz and $\gamma = 1.01\gamma_F$. Examples of the walker trajectory (of duration ~ 8 s) and instantaneous waveform at **(c)** $\gamma/\gamma_F = 0.91$ and **(d)** $\gamma/\gamma_F = 0.99$. The corresponding mean waveform (obtained over ~ 60 s) at **(e)** $\gamma/\gamma_F = 0.91$ and **(f)** 0.99, respectively.

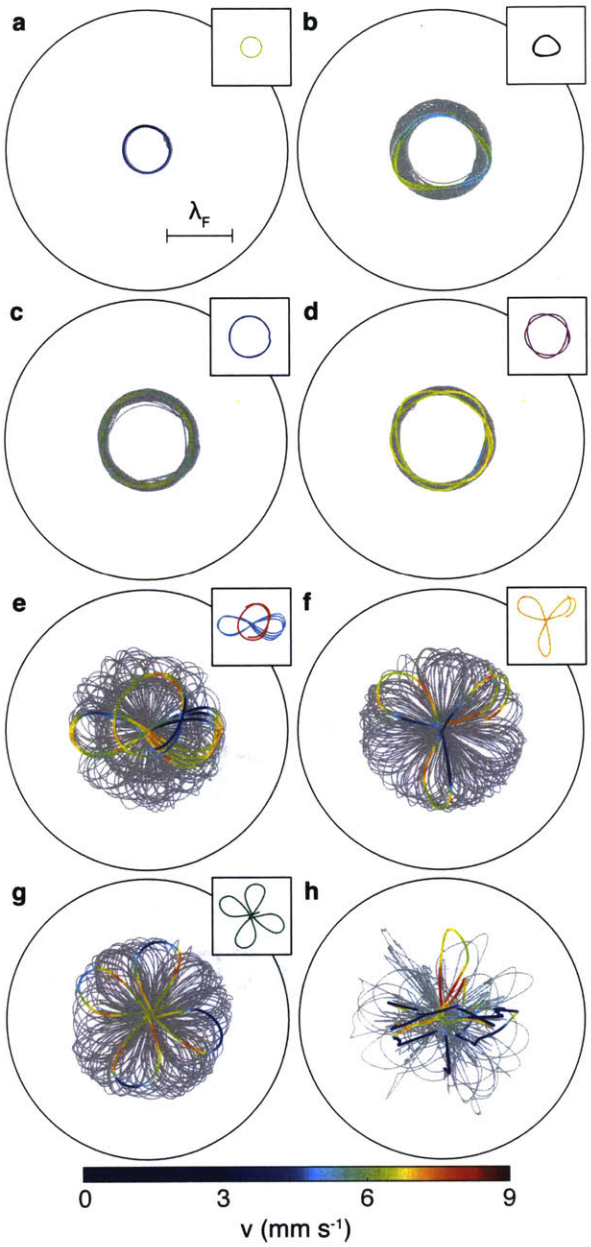

Figure A-11: Fundamental trajectories in a circular corral of diameter $D = 20.2$ mm. **(a)** Small circle at $\gamma/\gamma_F = 0.88$. **(b)** Deformed circle at $\gamma/\gamma_F = 0.91$ **(c)** Large circle at $\gamma/\gamma_F = 0.92$. **(d)** Large wobbling circle at $\gamma/\gamma_F = 0.93$. **(e)** Oval and lemniscate embedded within a complex trajectory at $\gamma/\gamma_F = 0.935$. **(f)** Trefoil at $\gamma/\gamma_F = 0.94$. **(g)** Papillon at $\gamma/\gamma_F = 0.95$. **(h)** Erratic motion punctuated by intermittent trapping at $\gamma/\gamma_F = 0.98$. Wave-induced trapping locations correspond to the deep blue portions of the trajectories. The fundamental trajectories are colour-coded according to instantaneous speed. The grey trajectories represent 5 minute long series. $\lambda_F = 4.75$ mm indicates the Faraday wavelength.

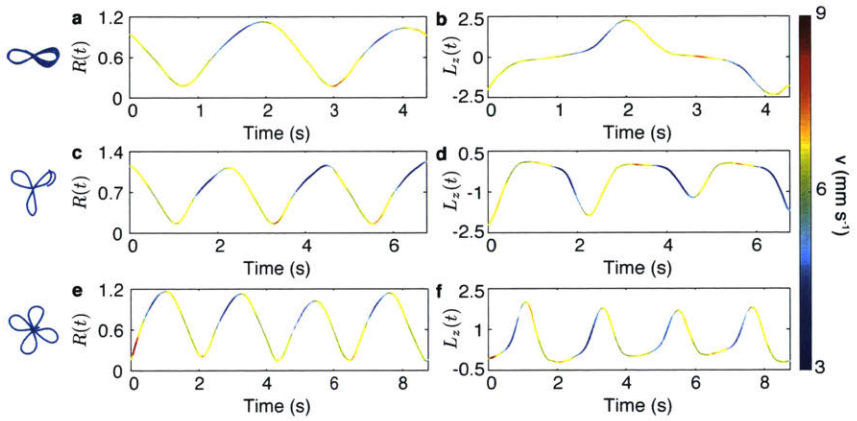

Figure A-12: Time series of radial orbit and angular momentum, colour-coded according to instantaneous drop speed, over one orbital period for **(a,b)** a lemniscate, **(c,d)** a trefoil, and **(e,f)** a papillon. The trajectories analysed are those highlighted in figures A-11e,f,g.

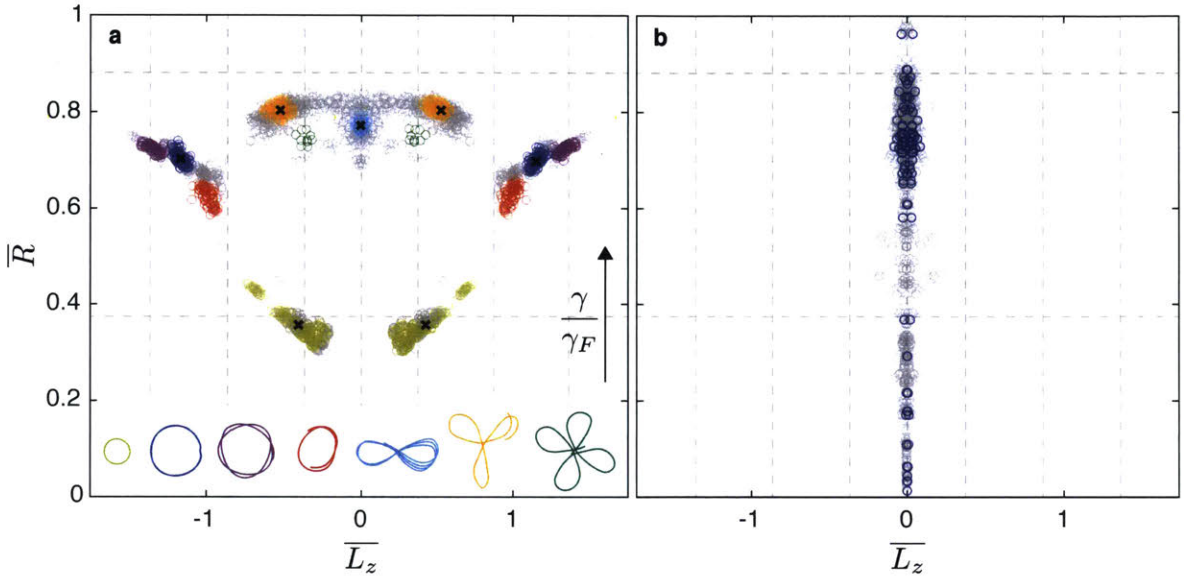

Figure A-13: The double quantisation of angular momentum and orbital radius evident in the circular corral. The axes are the non-dimensional mean angular momentum, $\overline{L_z}$ and the non-dimensional mean radius, $\overline{R}$. Each grey circle represents a separate sub-trajectory. Fundamental trajectories are colour coded to correspond to those shown in figure A-11. The black crosses are the centroids found via K-means clustering [36]. The data has been symmetrised with respect to $L_z = 0$. The dashed grid has the same spacing as the one used by Perrard *et al.* [104, 103]. **(a)** In the intermediate memory regime ($\gamma/\gamma_F = 0.87 - 0.95$), the individual clusters are representative of the stable trajectories identified in figure A-11. **(b)** In the high memory regime ($\gamma/\gamma_F = 0.98 - 0.99$), where trajectories are similar to that in figure A-11h, the scarcity of clusters with $\overline{L_z} \neq 0$ indicates the dissolution of the double quantisation apparent at lower memory. The blue circles denote walkers in trapped states.

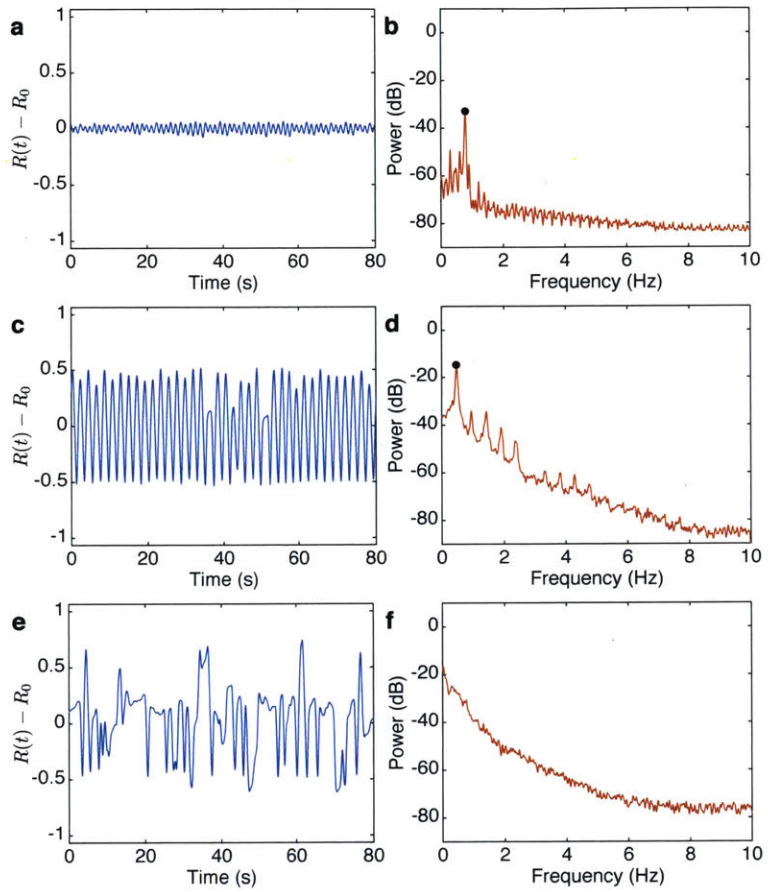

Figure A-14: Walker radial position time series (left column) and associated power spectra (right column) at different memories. The black circles highlight the frequency peaks. **(a)** − **(b)** $\gamma/\gamma_F = 0.93$, corresponding to the large wobbling circular trajectory shown in figure A-11c. **(c)** − **(d)** $\gamma/\gamma_F = 0.95$, corresponding to the trajectory shown in figure A-11f. **(e)** − **(f)** $\gamma/\gamma_F = 0.98$, corresponding to the trajectory shown in figure A-11h.

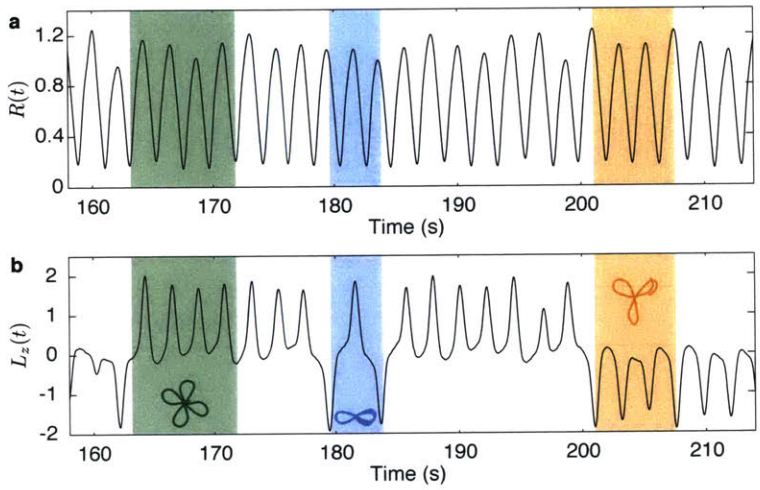

Figure A-15: Time series of **(a)** orbital radius and **(b)** angular momentum illustrating chaotic switching between fundamental orbits at $\gamma/\gamma_F = 0.95$. The green shaded area corresponds to a papillon, the blue to a lemniscate, and the orange to a trefoil.

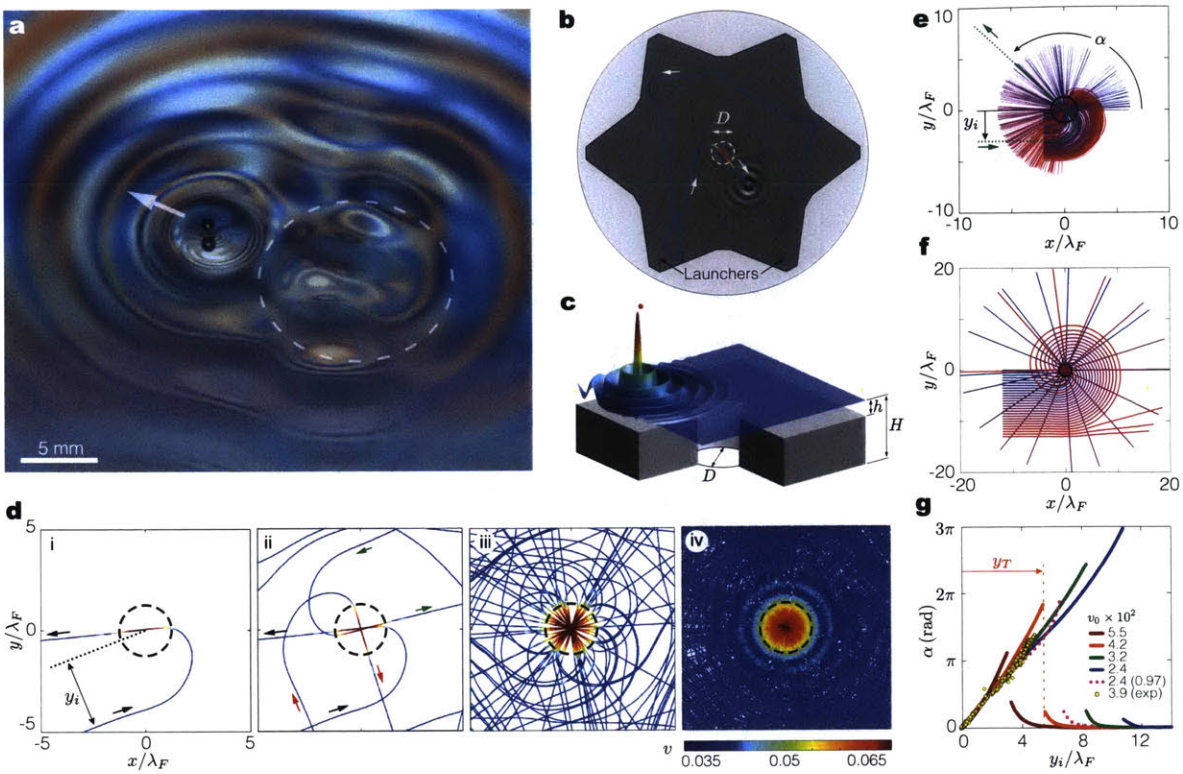

Figure A-16: Walker dynamics in the vicinity of a circular well. **(a)** Oblique view of a walking drop self-propelling above a submerged circular well (dashed line). Supplementary Movie 1. **(b)** Top view of the experimental setup. A submerged well of diameter $D = 13 \pm 0.1$ mm is located at the centre of a circular liquid bath vibrated vertically at frequency $f = 70$ Hz and maximum acceleration $\gamma/\gamma_F = 0.990 \pm 0.002$. The corner geometry serves to automatically redirect the walker towards the well. **(c)** Schematic cross section. The submerged well of depth $H = 6.2 \pm 0.03$ mm is located at the bottom of a relatively shallow liquid layer of depth $h = 1.6 \pm 0.03$ mm. **(d)** Walker trajectories with $\gamma/\gamma_F = 0.990$, drop radius $R = 0.39 \pm 0.01$ mm and free-walking speed $v_0 = 0.039$. The arrows denote the direction of motion and trajectories are colour-coded according to speed. A total of 449 trajectories were collected. **(e)** Experimental trajectories coloured according to their impact parameter y_i. These trajectories are obtained by rotating those shown in **d-iv** until the drop's initial motion is parallel to the x-axis. α then denotes the scattering angle at which the walker exits the well. **(f)** Simulated trajectories with uniformly-distributed impact parameters y_i for a drop with $v_0 = 0.024$ at $\gamma/\gamma_F = 0.990$. **(g)** Scattering angle versus impact parameters y_i for experimental (yellow dots) and simulated (solid lines) trajectories with walkers of different size (speed) at $\gamma/\gamma_F = 0.990$. The dotted magenta line corresponds to the same drop as the blue solid line but at a lower memory, $\gamma/\gamma_F = 0.970$. Space is non-dimensionalised by the Faraday wavelength $X_0 = \lambda_F$ in the shallow region and speed by $V_0 = X_0/T_F$, where $T_F = 2/f$ is the Faraday period.

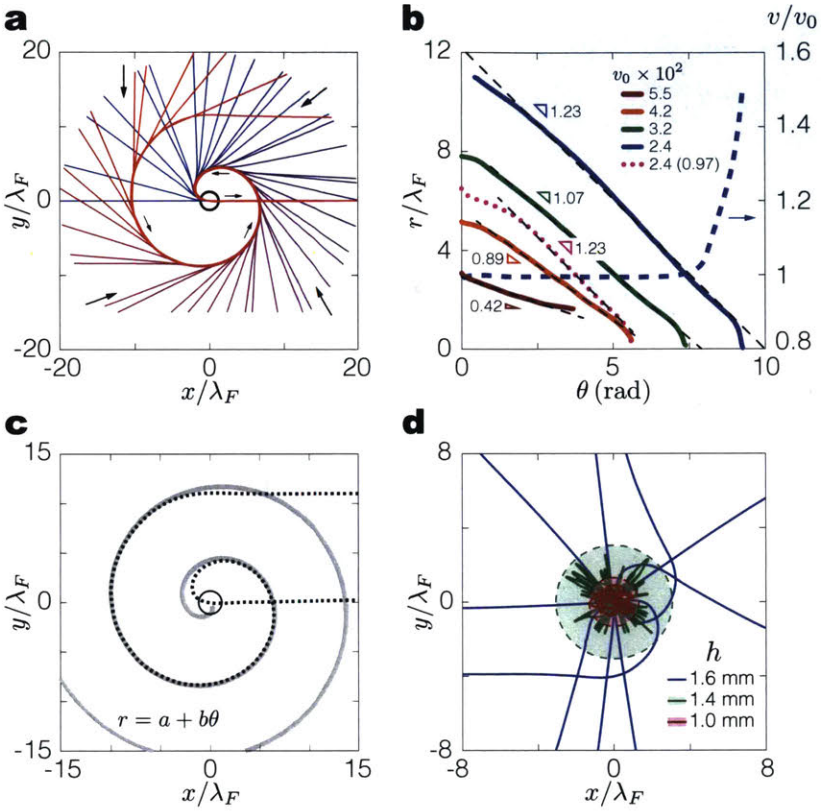

Figure A-17: Spiral trajectory and effective force. **(a)** Unique spiral resulting from suitable rotation of the trajectories shown in Fig. A-16f. Only walkers trapped by the well are considered. **(b)** Dependence of the radial coordinate r (solid and dotted lines) on the azimuthal angle θ for the longest spirals achieved with walkers of different size (speed), as previously shown in Fig. A-16g. The nearly linear relation between r and θ demonstrates that the incoming drop trajectory is well approximated by an Archimedean spiral. The dashed blue line shows the normalised instantaneous speed v/v_0 corresponding to the drop with $v_0 = 0.024$ at $\gamma/\gamma_F = 0.990$ (solid blue line). **(c)** Comparison between the drop trajectory (dashed line) and the Archimedean spiral (solid) obtained with the fit shown in **b** for $v_0 = 0.024$ at $\gamma/\gamma_F = 0.990$. **(d)** Experimental dependence of walker trajectories at $\gamma/\gamma_F = 0.990$ on depth h illustrates heightened trapping states at small h. The red-shaded area corresponds to the extent of the well. The drop size is the same as in Fig. A-16d.

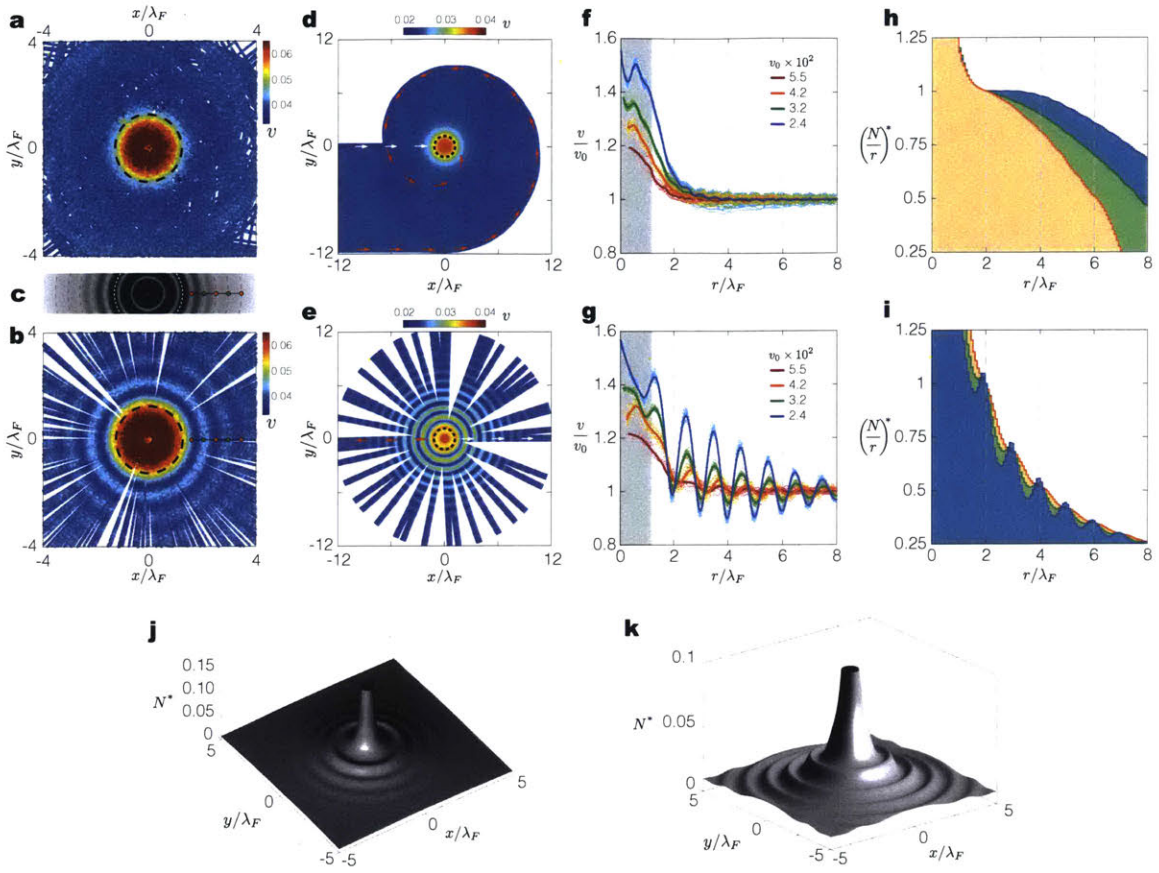

Figure A-18: Emergent statistical behaviour. Top view illustrating the experimental **(a)** incoming, and **(b)** outgoing drop trajectories coloured according to speed v. Trajectories are obtained by splitting those shown in Fig. A-16d at the point nearest to the centre of the well (dashed line). Concentric speed modulations appear in the outgoing phase. **(c)** Faraday waves observed above the well at threshold $\gamma = \gamma_F$. Note the spatial correspondence between the Faraday wave extrema and the speed modulations observed in the outgoing trajectories shown in **b**. **(d, e)** Incoming (top) and outgoing (bottom) speed-coloured trajectories corresponding to the slowest walker in Fig. A-16g, as presented in Fig. A-16f. White and red arrows identify the outermost trajectories crossing the well. **(f, g)** Dependence of the normalised speed v on radius r for incoming (top) and outgoing (bottom) walkers of different size (speed). The grey area denotes the well's extent. **(h, i)** Histogram of the drop's radial position corresponding to the data shown in **f** and **g**. The bin size is $\lambda_F/13$. The histograms have been normalised by their respective height at $r/\lambda_F = 2$, corresponding to the first speed minimum outside the well observed in **e**. **(j, k)** Two-dimensional histograms (normalised by the histogram height at the centre of the well) resulting from the experimental **b**, and simulated **e** outgoing trajectories, respectively.

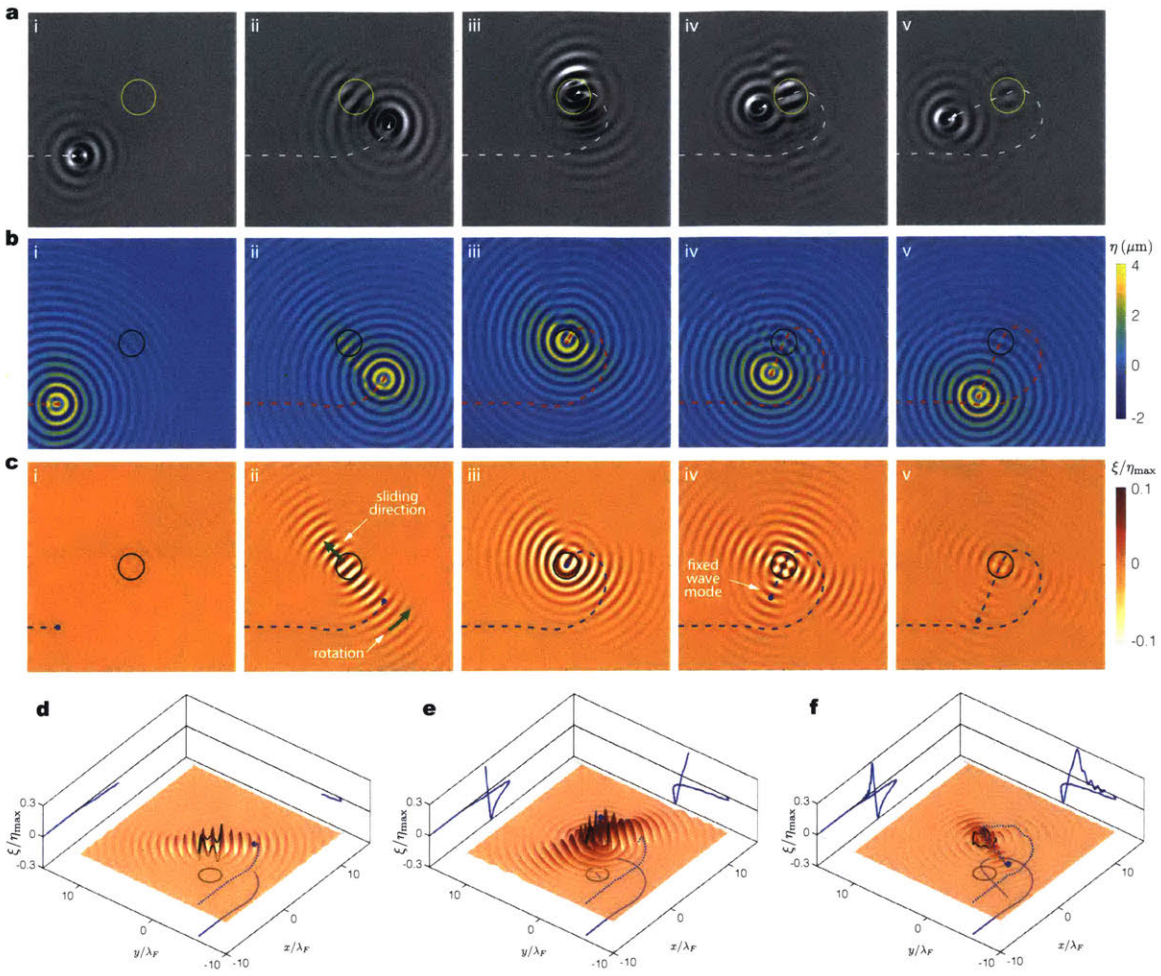

Figure A-19: Wave-mediated interaction. **(a)** Experimental and **(b)** simulated walker wave field ηat different stages during its interaction with a submerged well (solid circle). Snapshots illustrate the walker **(i)** approaching the well in straight-line motion, **(ii)** spiralling inwards, **(iii)** exciting localised large-amplitude waves as it crosses the well, **(iv,v)** exiting the well along a straight trajectory. **(c)** Well-induced wave perturbation $\zeta = \eta - \bar{\eta}$ (normalised by the instantaneous maximum wave amplitude$\eta_{max} = \max|\eta|$) obtained by subtracting from the wave field η shown in **b** the computed wave field $\bar{\eta}$ of a drop following the same trajectory in the absence of the well. A sliding beam-like wave mode emerges as the drop spirals inwards **(ii)**. Conversely the drop crosses a spatially fixed wave mode entered at the well in the outgoing trajectory **(iv)**, giving rise to the wavelike statistics evident in Fig. A-18. **(d-f)** 3D visualisation of the well-induced wave perturbation as the drop spirals inwards, crosses the well and exits in straight-line motion, respectively. Solid lines illustrate the time series of the perturbation at the drop position. The simulated walker corresponds to $\gamma/\gamma_F = 0.990$, $v_0 = 0.024$ and $y_i/\lambda_F = 6$.

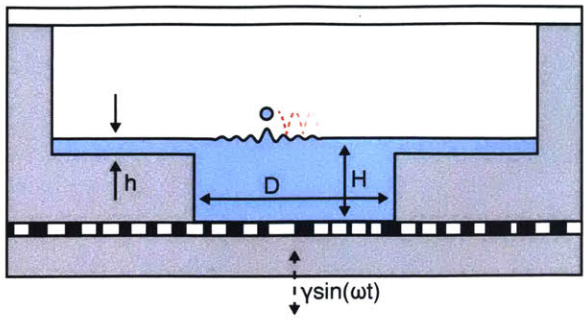

Figure A-20: The experimental set-up, showing the cross-sectional view of the corral filled with silicon oil and indicating the dotted-pattern beneath it used for free-surface synthetic Schlieren.

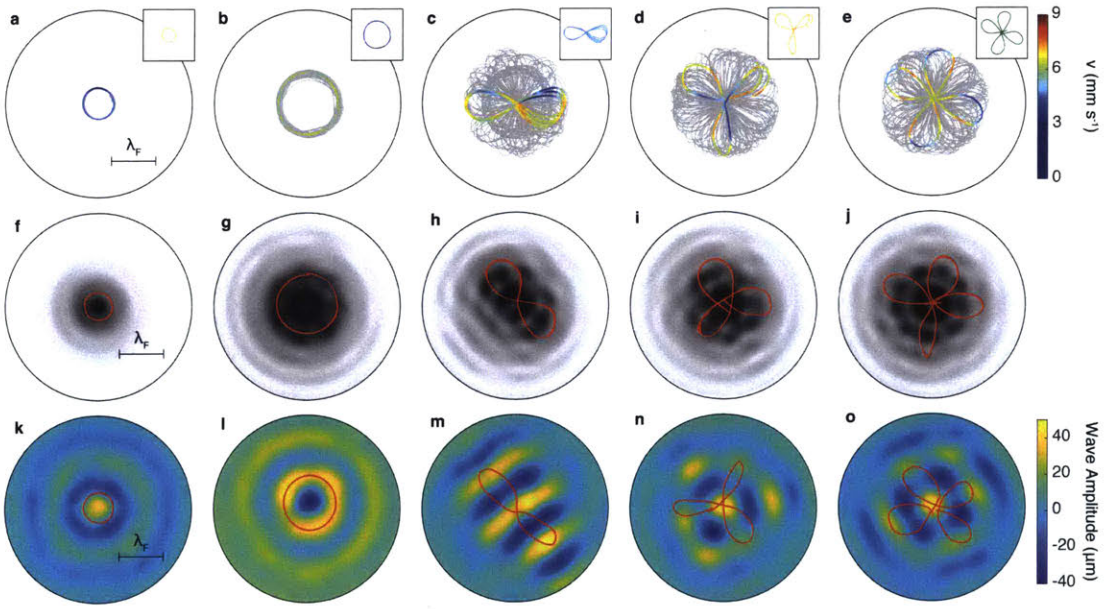

Figure A-21: Fundamental trajectories with their associated mean wave fields in a circular corral of diameter $D = 20.2$ mm. Top row represents the droplet's trajectories colour coded by speed. The grey trajectories represent 5 minute long series. Middle row illustrates the mean wave fields using the grey-scale image technique used by [114]. Bottom row represents the associated mean wave fields obtained using the free-surface synthetic Schlieren, [91]. **(a,f,k)** Small circle at $\gamma/\gamma_F = 0.88$. **(b,g,l)** Large circle at $\gamma/\gamma_F = 0.92$. **(c,h,m)** Lemniscate embedded within a complex trajectory at $\gamma/\gamma_F = 0.935$. **(d,i,n)** Trefoil at $\gamma/\gamma_F = 0.94$. **(e,j,o)** Papillon at $\gamma/\gamma_F = 0.95$. The trajectories coloured in red and their associated mean wave fields were recorded over one orbital period. $\lambda_F = 4.75$ mm indicates the Faraday wavelength.

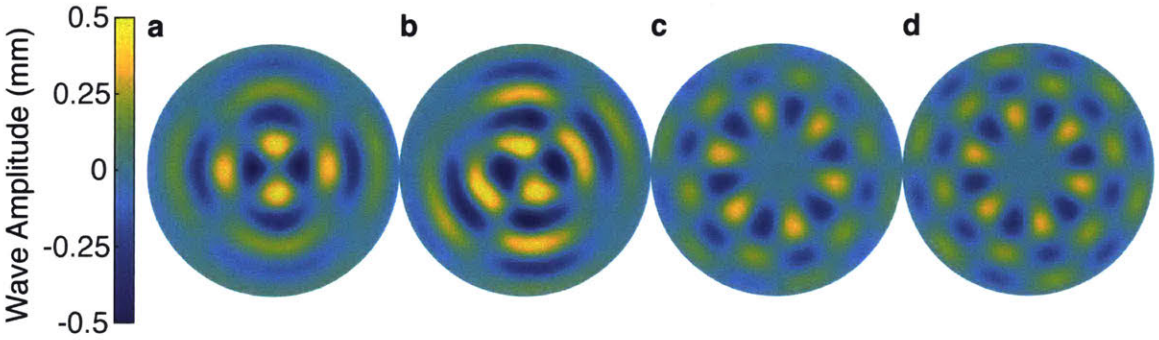

Figure A-22: Experimentally obtained Faraday waves modes for a circular corral of diameter $D = 28.5$ mm, driven at 65 Hz with **a** $h = 1.00 \pm 0.03$ mm. **b** $h = 0.50 \pm 0.03$ mm. **c** $h = 0.05 \pm 0.03$ mm. **d** The (3,6) mode given by equation (6.2).

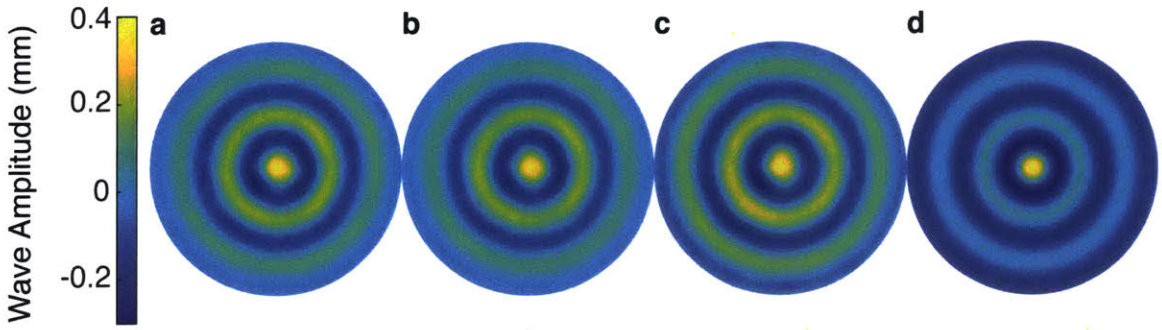

Figure A-23: Experimentally obtained Faraday waves modes for a circular corral of diameter $D = 28.5$ mm, driven at 70 Hz with **a** $h = 1.00 \pm 0.03$ mm. **b** $h = 0.50 \pm 0.03$ mm. **c** $h = 0.05 \pm 0.03$ mm. **d** The (6,0) mode given by equation (6.2).

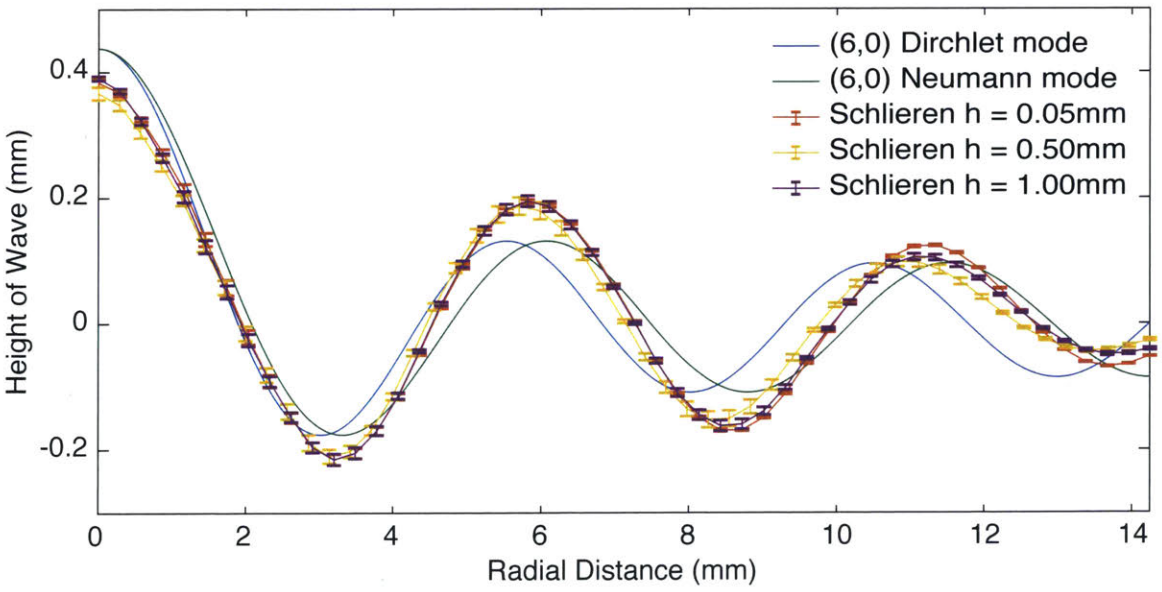

Figure A-24: Comparison between the azimuthally symmetric $(6, 0)$ Dirichlet and Neumann modes and the Faraday wave mode obtained for the circular corral of diameter $D = 28.5$ mm, driven at 70 Hz with $h = 0.05 \pm 0.03$ mm, $h = 0.50 \pm 0.03$ mm, and $h = 1.00 \pm 0.03$ mm.

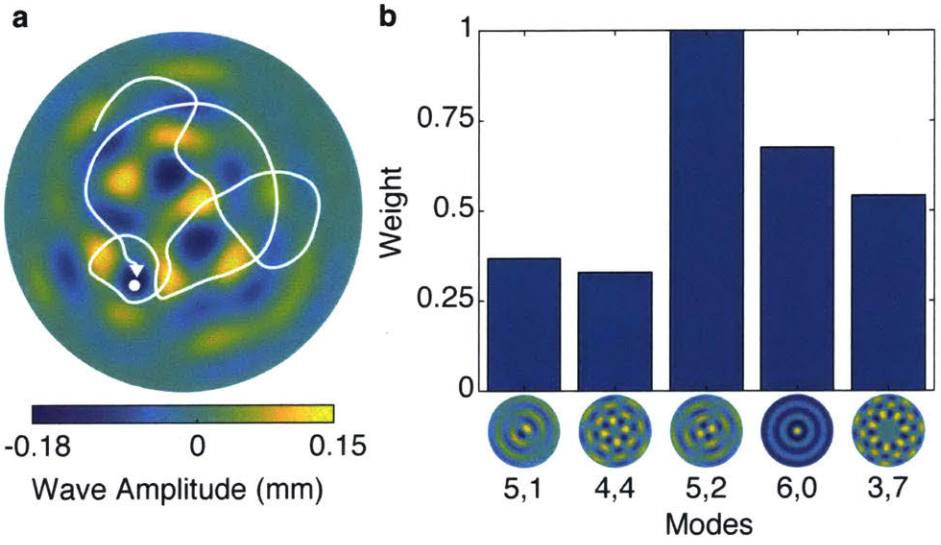

Figure A-25: Instantaneous wave field when the droplet is exploring the circular corral of diameter $D = 28.5$ mm, vibrated vertically at $f = 70$ Hz. **a** An arbitrary selected instantaneous wave field. Overlaid in white is an example of the walker trajectory (of duration ~ 10 s). **b** The weights of the five most dominant modes present in the reconstruction of an arbitrary selected instantaneous wave field.

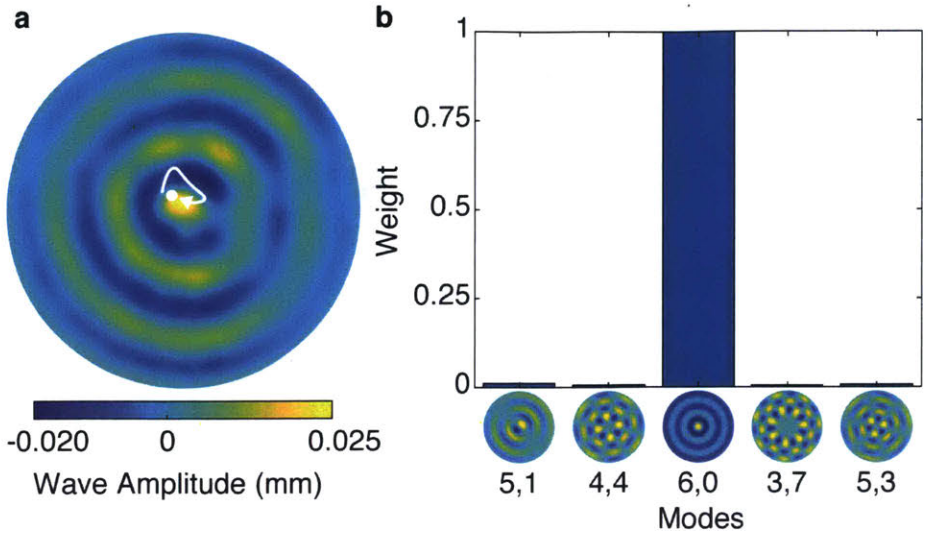

Figure A-26: Azimuthally symmetric instantaneous wave field when the droplet is exploring the circular corral of diameter $D = 28.5$ mm, vibrated vertically at $f = 70$ Hz. **a** Instantaneous wave field displaying the dominantly described by one azimuthally symmetric mode. Overlaid in white is an example of the walker trajectory (of duration ~ 1 s). **b** The weights of the five most prominent modes present in the reconstruction of the mean wave field.

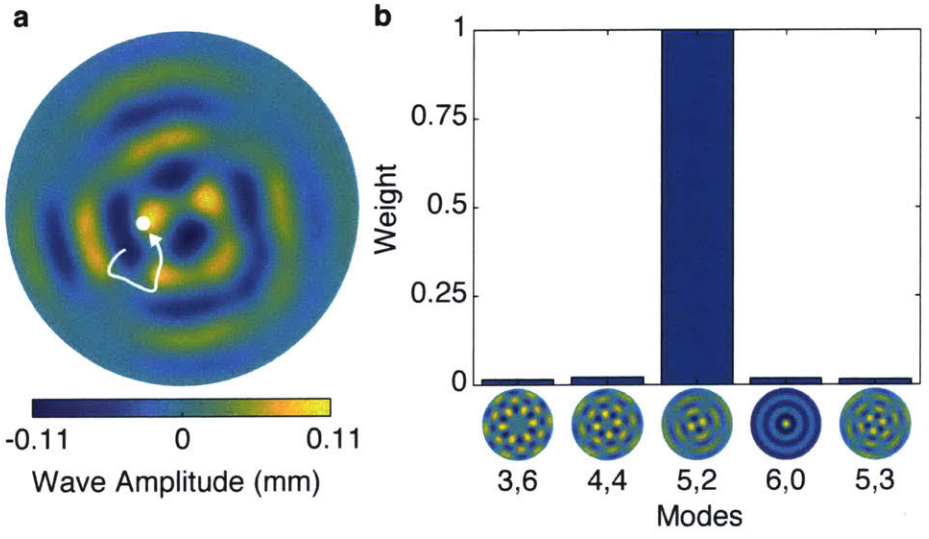

Figure A-27: Non-azimuthally symmetric instantaneous wave field when the droplet is exploring the circular corral of diameter $D = 28.5$ mm, vibrated vertically at $f = 70$ Hz. **a** Instantaneous wave field displaying the dominantly described by one non-azimuthally symmetric mode. Overlaid in white is an example of the walker trajectory (of duration ~ 1 s). **b** The weights of the five most prominent modes present in the reconstruction of the mean wave field.

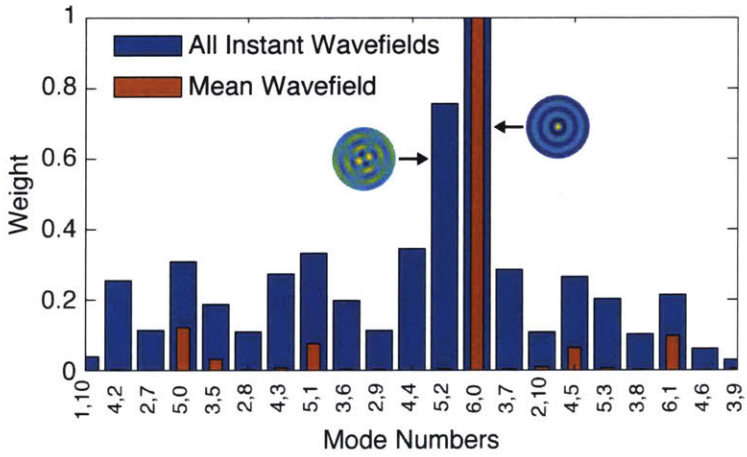

Figure A-28: Distribution of the mode decomposition weights for the instantaneous wave fields and mean wave field, shown in blue and red, respectively. The modes are ordered by increasing eigenvalue, λ_{mn}, and labeled as (n, m). The weights are normalised with respect to that of the dominant mode. No significant modes were present outside the $(1, 10) - (3, 9)$ range.

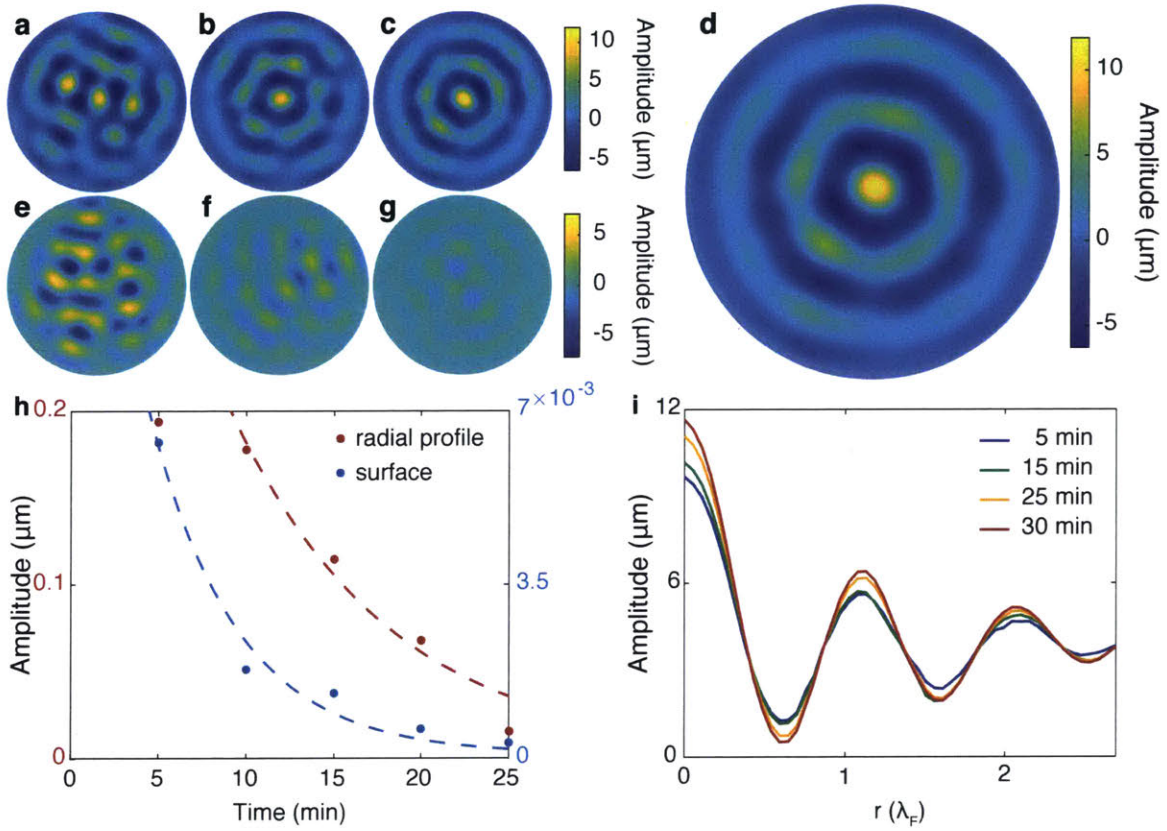

Figure A-29: The mean wave field is computed over increasing periods of time **a** 5 minutes, **b** 15 minutes, **c** 25 minutes, **d** 30 minutes. The difference between the mean wave field obtained after 30 minutes and after **e** 5 minutes, **f** 15 minutes, **g** 25 minutes. The differences between the converged mean wave field in **d** and the mean wave fields in **a**, **b**, and **c**, are shown in **e**, **f**, and **g**, respectively. The convergences of the mean wave field and of its radial profile as a function of time are illustrated in **h**, where the l^2-norm was utilised to characterise the differences between the wave fields. The dotted lines represent the fitted exponential decays. The mean wave field's radial profiles for increasing periods of time are shown in **i**. The corral of diameter $D = 28.5$ mm is vibrated vertically at $f = 70$ Hz for $\gamma/\gamma_F = 0.995$.

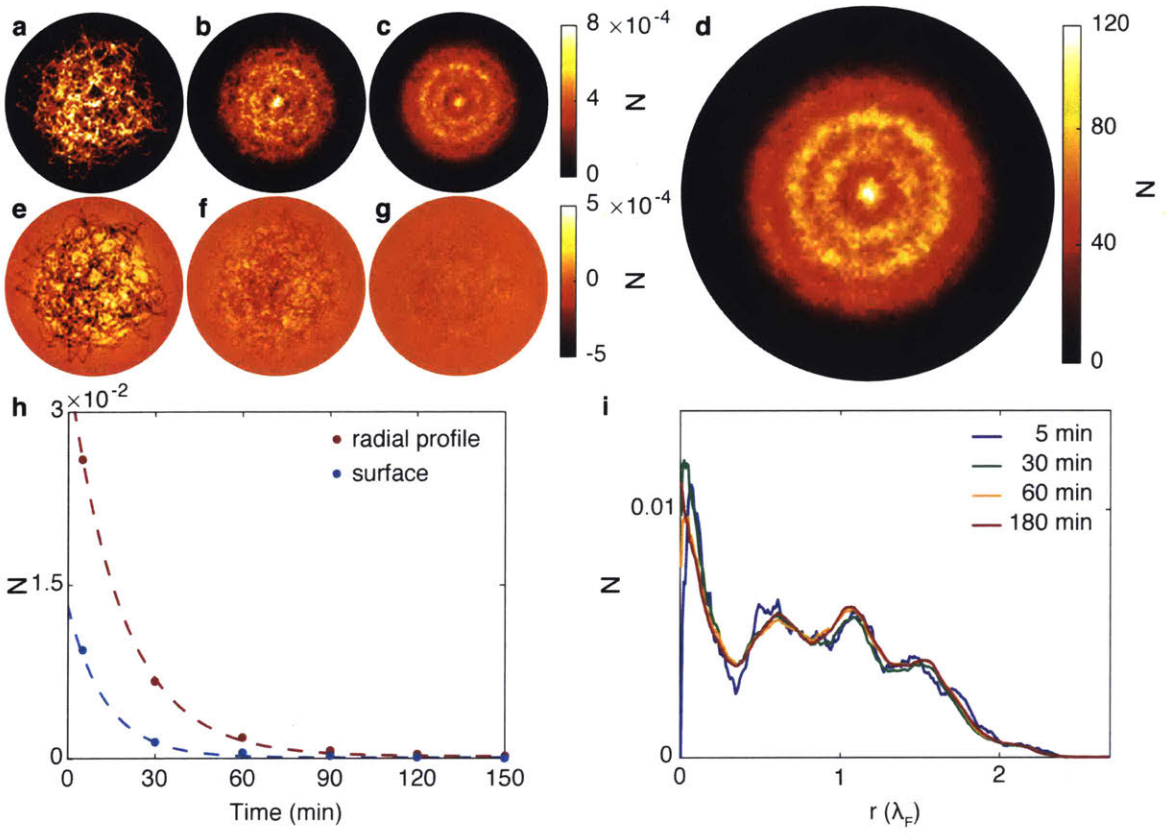

Figure A-30: Evolution of the walker's position histogram, after **a)** 5 minutes, **b)** 30 minute, **c)** 60 minutes, and **d)** 180 minutes. The differences between the converged walker histogram in **d** and the walker histograms in **a**, **b**, and **c**, are shown in **e**, **f**, and **g**, respectively. Note that we normalise the histograms, expect for the one in **d)**, by dividing the individual bin counts by the total count. The colour axis represents the bin count. The convergences of the histogram and of its radial profile as a function of time are illustrated in **h**, where the l^2-norm was utilised to characterise the differences between the histograms. The dotted lines represent the fitted exponential decays. The histogram's radial profiles for increasing periods of time are shown in **i**. The corral of diameter $D = 28.5$ mm is vibrated vertically at $f = 70$ Hz for $\gamma/\gamma_F = 0.995$.

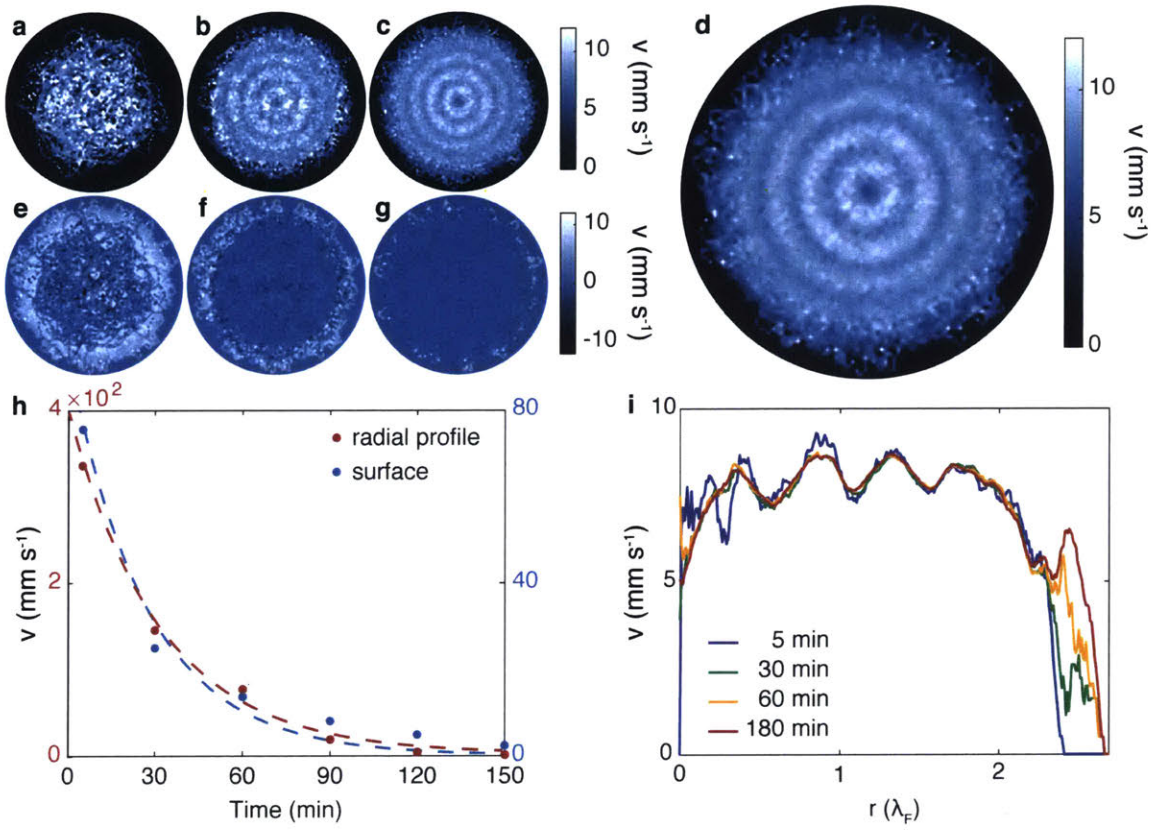

Figure A-31: Evolution of the walker's average speed map, after **a)** 5 minutes, **b)** 30 minute, **c)** 60 minutes, and **d)** 180 minutes. The differences between the converged average speed map in **d** and the average speed maps in **a**, **b**, and **c**, are shown in **e**, **f**, and **g**, respectively. The colour axis represents the droplet's speed. The convergences of the average speed map and of its radial profile as a function of time are illustrated in **h**, where the l^2-norm was utilised to characterise the differences between the speed maps. The dotted lines represent the fitted exponential decays. The average speed map's radial profiles for increasing periods of time are shown in **i**. The corral of diameter $D = 28.5$ mm is vibrated vertically at $f = 70$ Hz for $\gamma/\gamma_F = 0.995$.

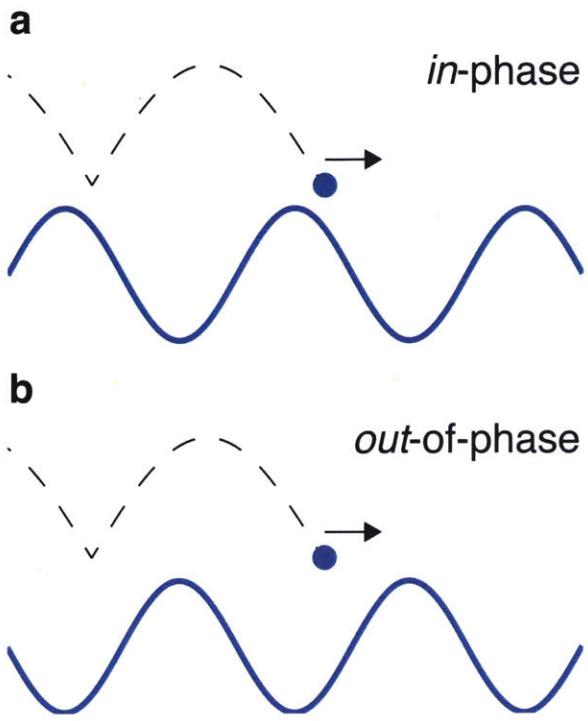

Figure A-32: Schematic of the droplet's impact phase relative to the liquid's surface illustrating the **a** *in*-phase and **b** *out*-of-phase cases. The droplet's previous vertical motion is indicated by the dotted line and its future horizontal direction by the arrow.

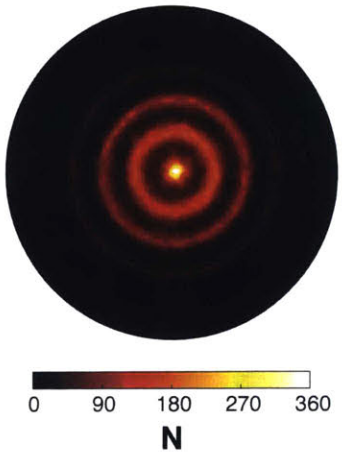

Figure A-33: The walker position histogram obtained after 180 minutes for $\gamma/\gamma_F = 1.004$. The corral of diameter $D = 28.5$ mm is vibrated vertically at $f = 70$ Hz.

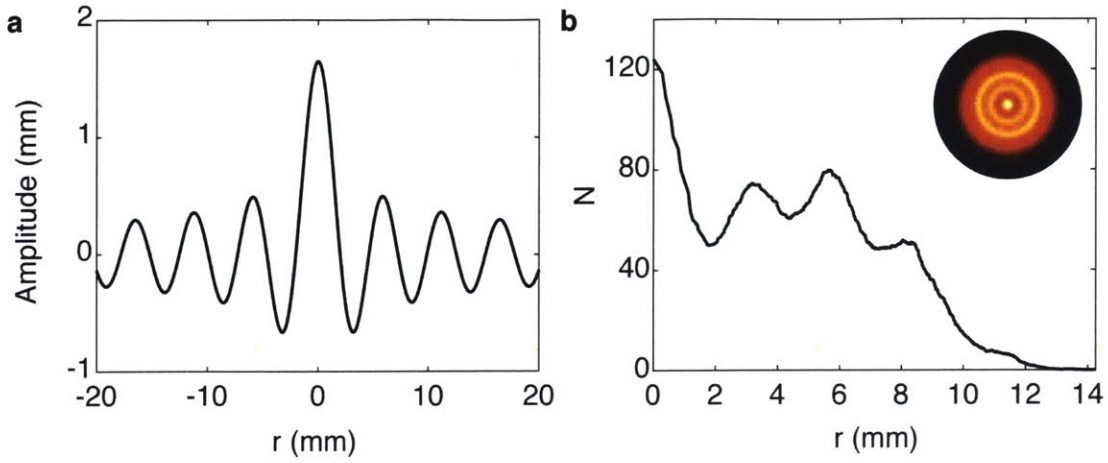

Figure A-34: **a** Wave profile of a free bouncer at $\gamma/\gamma_F = 0.995$. **b** The position histogram of the droplet as a function of distance from the corral's origin. Inset: Azimuthally symmetrised position histogram.

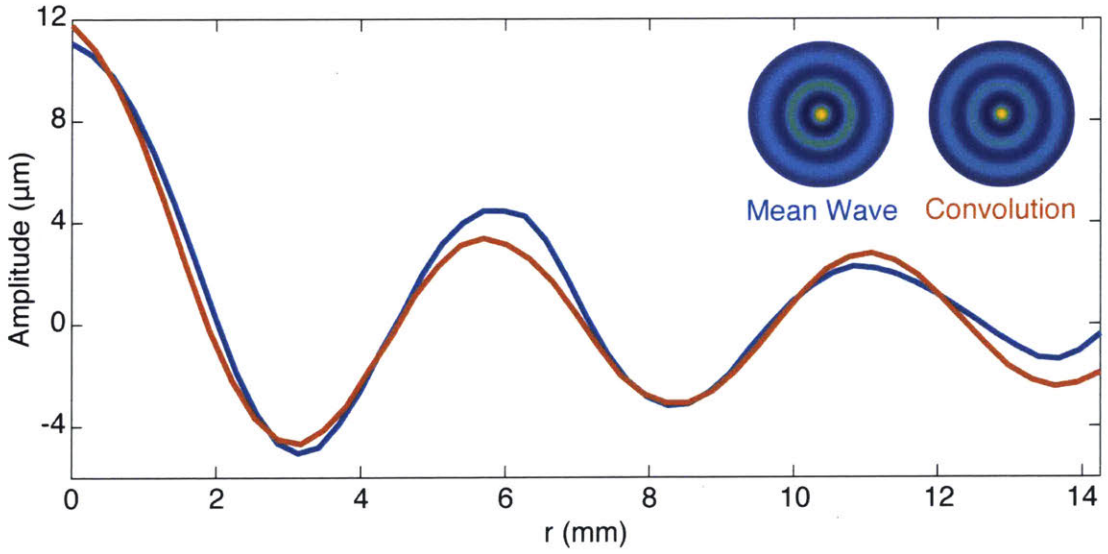

Figure A-35: Comparison plot showing the radial dependence of the mean wave field and the convolution of the bouncer wave field with the position histogram of the droplet. Inset - Azimuthally symmetrised mean and convolution wave fields.

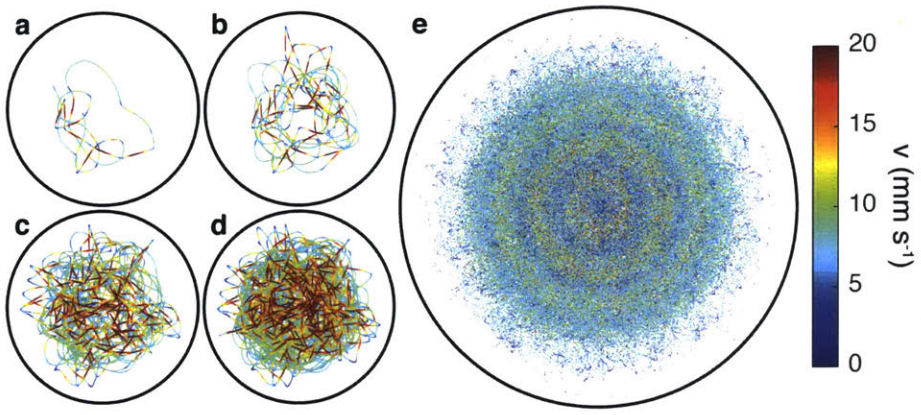

Figure A-36: The walker trajectories are colour coded by speed for increasing time intervals of **a** 15 seconds, **b** 60 seconds, **c** 120 seconds, **d** 480 seconds. **e** Emergent pattern after 3 hours. The corral of diameter $D = 28.5$ mm is vibrated vertically at $f = 70$ Hz for $\gamma/\gamma_F = 0.995$.

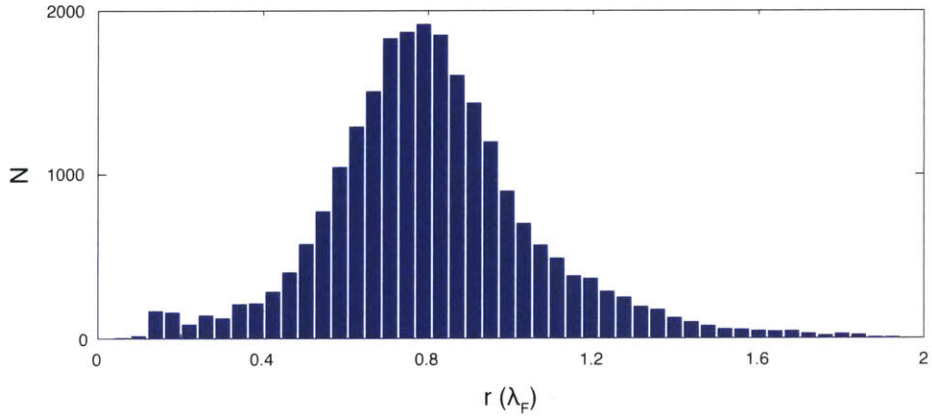

Figure A-37: Histogram illustrating the spacing of the walker speed oscillations along its trajectory. The corral of diameter $D = 28.5$ mm is vibrated vertically at $f = 70$ Hz for $\gamma/\gamma_F = 0.995$.

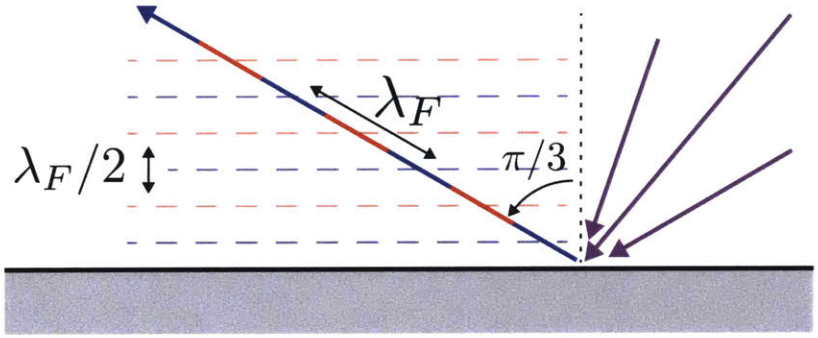

Figure A-38: Droplets reflected from a wall show a preferred reflection angle of ~60°, regardless of their incident angle. The incoming walker trajectories are coloured in purple. The outgoing walker trajectory is colour coded by speed, blue being slow, red being fast. The speed oscillations along the outgoing trajectory have spacing λ_F. Their normal projections lead to a speed map with oscillations of wavelength $\lambda_F/2$.

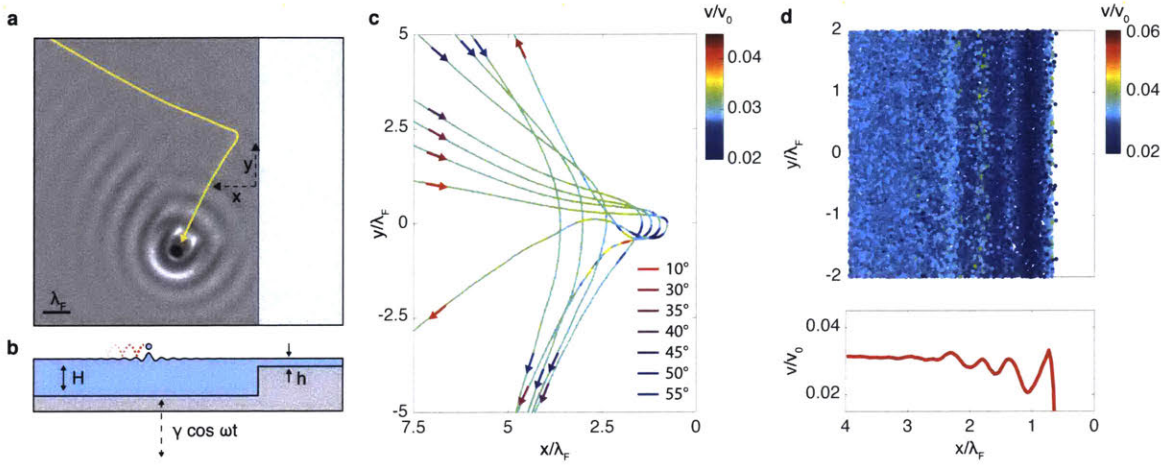

Figure A-39: The walker interacting with a submerged boundary. **a** The droplet's outgoing trajectory and grey scale wave-field. **b** Experimental schematic. **c** The walker's incoming and reflected trajectory are coloured by the droplet's speed, with arrows indicating the incidence angle. The speed oscillations along the outgoing trajectory have spacing λ_F. **d** Speed map emerging from ~ 350 walker trajectories reflected by a submerged wall, showing speed modulations of wavelength $\lambda_F/2$. The deeper fluid region has a thickness of 6.20 ± 0.05 mm and the think film above the barrier is 0.25 ± 0.05 mm. The bath is vibrated vertically at $f = 70$ Hz for $\gamma/\gamma_F = 0.990$.

Appendix B

Friedel Oscillations from a submerged well

B.1 Numerical Simulations

Our simulations are performed with the model developed by Faria [44] to account for variable bottom topography, which builds on the linearized quasi-potential, weakly-viscous flow model developed by Milewski *et al.* [89] and Dias *et al.* [33]. Faria [44] reduces the problem to the free surface $\eta(\boldsymbol{x}, t)$ by treating changes in topography as regions where the local wave speed changes. Specifically, the wave problem becomes

$$\phi_t = -G(t)\eta + \frac{\sigma}{\rho}\nabla^2\eta + 2\nu_e\nabla^2\phi - \frac{1}{\rho}P_D(\boldsymbol{x} - \boldsymbol{x}_p(t), t) \tag{B.1}$$

$$\eta_t = -\nabla\cdot[b(\boldsymbol{x})\nabla\phi] + 2\nu_e\nabla^2\eta \tag{B.2}$$

where $\phi(\boldsymbol{x}, t)$ denotes the velocity potential $\boldsymbol{u} = \nabla\phi$ in the bath, $G(t) = g + \gamma\cos(2\pi ft - \varphi)$ the effective gravity in the bath's frame of reference, φ the drop's impact phase, $\nu_e = 0.861\nu$ the effective kinematic viscosity (chosen to match the experimental stability threshold γ_F), and $\boldsymbol{x}_p(t)$ the drop's horizontal position. The wave-drop coupling is modeled by treating the drop as an instantaneous excess point-pressure P_D on the dynamic surface condition[93, 89]. Changes in bottom topography are modeled by approximating the vertical gradient of the velocity potential as

$\phi_z \approx -\nabla \cdot [b(\boldsymbol{x})\nabla\phi]$, where $b(\boldsymbol{x})$ is an effective depth chosen to ensure the correct the dispersion relation of Faraday waves in both the shallow and deep regions, according to

$$b(\boldsymbol{x}) = \begin{cases} \tanh(k_{F_H}H)/k_{F_H}, & \text{for } \boldsymbol{x} \in \mathcal{W} \\ \tanh(k_{F_h}h)/k_{F_h}, & \text{for } \boldsymbol{x} \notin \mathcal{W} \end{cases} \tag{B.3}$$

where $\mathcal{W}$ denotes the well region, and k_{F_H} and k_{F_h} the most unstable wavenumbers in the deep and shallow region, respectively, computed as detailed by Milewski *et al.* [89].

The local gradient of the resulting wave field $\nabla\eta|_{\boldsymbol{x}=\boldsymbol{x}_p}$ determines the lateral force exerted on the drop at impact. The drop's trajectory is thus described through

$$m\frac{\mathrm{d}^2\boldsymbol{x}_p}{\mathrm{d}t^2} + \left(c_4\sqrt{\frac{\rho R}{\sigma}}F(t) + 6\pi R\mu_{\text{air}}\right)\frac{\mathrm{d}\boldsymbol{x}_p}{\mathrm{d}t} = -F(t)\nabla\eta|_{\boldsymbol{x}=\boldsymbol{x}_p} \tag{B.4}$$

where $\mu_{\text{air}} = 1.8\times10^{-5}$ Pa s is the dynamic viscosity of air, and $c_4 = 0.17$ the coefficient of tangential restitution [93]. The drop bounces periodically with the Faraday waves, the impacts thus take place at $t = nT_F$, where $T_F = 2/f$ is the Faraday period. Assuming instantaneous contacts, the force becomes $F(t) = mg\sum_{n=0}^{\infty}\delta(t/T_F - n)$, where δ is the delta function. Finally, the penetration depth of the drop is assumed to be infinitesimally small relative to the Faraday wavelength. The drop pressure thus becomes $P_D(\boldsymbol{x} - \boldsymbol{x}_p, t) = (F(t)/\lambda_F^2)\delta((\boldsymbol{x} - \boldsymbol{x}_p)/\lambda_F)$ which vanishes when the drop is not in contact with the bath [44].

The model is solved numerically using a pseudo-spectral method in space and periodic boundary conditions, and fourth-order Runge-Kutta scheme for the time integration [44]. The simulations are performed on a square domain of size $48\lambda_F^h \times 48\lambda_F^h$, discretized with 512×512 points. Numerical tests were performed to ensure that the domain size and spatial resolution were adequate to render discretization-independent results. Simulations with a larger domain size but the same resolution ($64\lambda_F^h \times 64\lambda_F^h$, 682×682) and same domain size but a finer resolution ($48\lambda_F^h \times 48\lambda_F^h$, 768×768) produced virtually indistinguishable results to those included in the main text.

R(mm)	γ/γ_F	v_0(mm/s)	$\varphi/2\pi$
0.355	0.990	4.4	0.259
0.375		5.8	0.266
0.390		7.1	0.269
0.400		7.6	0.277
0.425		10.0	0.286
0.355	0.970	4.4	0.268

Table B.1: Range of drops considered in this study. All the $R - v_0$ combinations are experimental observations with $h = 1.6\,\text{mm}$, except for the case with $\gamma/\gamma_F = 0.970$, where the impact phase φ has been readjusted in the simulations in order to maintain a constant v_0 with the smallest drop. This allows us to assess the role of memory independently from inertial effects, as illustrated in Fig. A-17g.

B.2 Effective Force

The drop is drawn into the well through an intricate wave-mediated interaction. However, an analytical expression for the effective well-induced force $\mathbf{F}_w$ may be inferred by exploiting two key observations from both experiments and simulations. Specifically, (i) the incoming trajectories are Archimedean spirals centred on the well to a good approximation, and (ii) the drop speed remains constant along the spiral trajectories.

The drop trajectory may thus be written as

$$r(\theta) = a + b\theta, \tag{B.5}$$

where $(r,\, \theta)$ are the polar coordinates on the horizontal plane, and a and b constants which may be determined from the initial conditions. Given the trajectory, one may infer the effective force $\mathbf{F}_w$ acting of the drop of mass m starting from the equation of motion $m\mathrm{d}\mathbf{v}/\mathrm{d}t = \mathbf{F}_w$, with $\mathbf{v} = \dot{r}\hat{\mathbf{e}}_\mathbf{r} + r\dot{\theta}\hat{\mathbf{e}}_\theta$ in polar coordinates. The force may thus be written as

$$\mathbf{F}_w = m\left[\left(\ddot{r} - r\dot{\theta}^2\right)\hat{\mathbf{e}}_\mathbf{r} + \left(r\ddot{\theta} + 2\dot{r}\dot{\theta}\right)\hat{\mathbf{e}}_\theta\right] \tag{B.6}$$

Since the drop speed $v = |\mathbf{v}|$ is constant along the incoming spiral trajectory, it follows

that

$$v^2 = v_r^2 + v_\theta^2 = \dot{r}^2 + (r\dot{\theta})^2 = \text{const}, \tag{B.7}$$

expression whose time derivative leads to

$$2\dot{r}\ddot{r} + 2r\dot{r}\dot{\theta}^2 + 2r^2\dot{\theta}\ddot{\theta} = 0. \tag{B.8}$$

Noting that $\dot{r} = b\dot{\theta}$ and $\ddot{r} = b\ddot{\theta}$ from (B.5), and that $\dot{r} \neq 0$ from (B.7), we may write

$$\ddot{r} = -\frac{r\dot{\theta}^2}{\left(1 + \frac{r^2}{b^2}\right)}, \quad \text{and} \quad \ddot{\theta} = -\frac{r\dot{\theta}^2}{b\left(1 + \frac{r^2}{b^2}\right)}. \tag{B.9}$$

By substituting (B.9) in (B.6), the force becomes

$$\mathbf{F}_w = m\frac{\left(2 + \frac{r^2}{b^2}\right)}{\left(1 + \frac{r^2}{b^2}\right)}\dot{\theta}^2\left(-r\hat{\mathbf{e}}_\mathbf{r} + b\hat{\mathbf{e}}_\theta\right) \tag{B.10}$$

Using $\dot{r} = b\dot{\theta}$ in (B.7), it follows that

$$v^2 = \dot{r}^2\left(1 + \frac{r^2}{b^2}\right). \tag{B.11}$$

We thus obtain the components of the effective well-induced force acting on the drop by substituting (B.11) and $\dot{r} = b\dot{\theta}$ in (B.10), which leads to

$$\mathbf{F}_w = m\left(1 + \frac{\dot{r}^2}{v^2}\right)\left(-r\dot{\theta}^2\hat{\mathbf{e}}_\mathbf{r} + \dot{r}\dot{\theta}\hat{\mathbf{e}}_\theta\right) \tag{B.12}$$

Denoting $v_r = \dot{r}$ and $v_\theta = r\dot{\theta}$, (B.12) may be written as

$$\mathbf{F}_w = m\frac{v_\theta}{r}\left(1 + \frac{\dot{r}^2}{v^2}\right)\left(-v_\theta\hat{\mathbf{e}}_\mathbf{r} + v_r\hat{\mathbf{e}}_\theta\right) \tag{B.13}$$

$$= m\left(1 + \frac{\dot{r}^2}{v^2}\right)\dot{\mathbf{\Theta}} \times \mathbf{v} \tag{B.14}$$

where $\dot{\mathbf{\Theta}} = (v_\theta/r)\hat{\mathbf{e}}_\mathbf{z}$.

We conclude by noting that the spiral parameters a and b may be determined

from the initial conditions. Denoting the initial position and velocity as (r_0, θ_0) and $(v_{r0}, v_{\theta 0})$, respectively, simple manipulations of the previous equations lead to

$$a = r_0 \left(1 - \frac{v_{r0}}{v_{\theta 0}} \theta_0\right), \quad \text{and} \quad b = r_0 \frac{v_{r0}}{v_{\theta 0}}. \tag{B.15}$$

Bibliography

[1] S. K. Adhikari. Quantum scattering in 2 dimensions. *Am. J. Phys.*, 54(4):362–367, 1986.

[2] D. Albert and B. Loewer. Interpreting the many-worlds interpretation. *Synthese*, 77:195–213, 1988.

[3] A. Andersen, J. Madsen, C. Reichelt, S. R. Ahl, B. Lautrup, C. Ellegaard, M. T. Levinsen, and T. Bohr. Double-slit experiment with single wave-driven particles and its relation to quantum mechanics. *Physical Review E*, 92(1), 2015.

[4] P. W. Anderson. Absence of diffusion in certain random lattices. *Phys. Rev. A*, 109:1492, 1958.

[5] G. Bacciagaluppi and A. Valentini. *Quantum Mechanics at the Crossroads. Reconsidering the 1927 Solvay Conference.* Cambridge University Press, 2009.

[6] L. E. Ballentine. *Quantum Mechanics: A Modern Development.* World Scientific Publishing Company, 2 edition, 2014.

[7] T. B. Benjamin and F. Ursell. The stability of the plane free surface of a liquid in vertical periodic motion. *Proceedings of the Royal Society of London A: Mathematical, Physical and Engineering Sciences*, 225(1163):505–515, 1954.

[8] F. Blanchette. Modeling the vertical motion of drops bouncing on a bounded fluid reservoir. *Physics of Fluids*, 28(3), 2016.

[9] D. Bohm. A suggested interpretation of the quantum theory in terms of "hidden variables" i. *Physical Review*, 85:166–179, 1952.

[10] D. Bohm. A suggested interpretation of the quantum theory in terms of "hidden variables" ii. *Physical Review*, 85:180–193, 1952.

[11] L. Boltzmann. Zur theorie der elastichen nachwirkung. *Wiener Berichte*, 70:275–306, 1874.

[12] M. Born. Quantenmechanik der kräftefreien teilchens. *Z. Phys.*, 38(11-12):803–827, 1926.

[13] M. Born and E. Wolf. *Principles of Optics: Electromagnetic Theory of Propagation, Interference and Diffraction of Light.* Cambridge University Press, 7 edition, 1999.

[14] J. W. M. Bush. Pilot-Wave Hydrodynamics. *Annual Review of Fluid Mechanics*, 47(1):269–292, 2015.

[15] J. W. M. Bush, Y. Couder, T. Gilet, P. A. Milewski, and A. Nachbin. Introduction to focus issue on hydrodynamic quantum analogs. *Chaos: An Interdisciplinary Journal of Nonlinear Science*, 28(9):096001, 2018.

[16] John W. M. Bush. The new wave of pilot-wave theory. *Physics Today*, 68(8):47–53, 2015.

[17] D. Chattopadhyay and H. J. Queisser. Electron scattering by ionized impurities in semiconductor. *Rev. Mod. Phys.*, 53(4):745–768, 1981.

[18] S. Ciliberto and J. P. Gollub. Phenomenological model of chaotic mode competition in surface waves. *Il Nuovo Cimento D*, 6(4):309–316, 1985.

[19] C. Cohen-Tannoudji, B. Diu, and F. Laloë. *Quantum Mechanics, Volumes 1 and 2.* Wiley, 1977.

[20] M. M. P. Couchman, S. E. Turton, and J. W. M. Bush. Bouncing phase variations in pilot-wave hydrodynamics and the stability of droplet phase. *J. Fluid Mech.*, Accepted, 2019.

[21] Y. Couder and E. Fort. Single-particle diffraction and interference at a macroscopic scale. *Physical Review Letters*, 97(15), 2006.

[22] Y. Couder, E. Fort, C. H. Gautier, and A. Boudaoud. From bouncing to floating: Noncoalescence of drops on a fluid bath. *Physical Review Letters*, 94(17), 2005.

[23] Y. Couder, S. Protière, E. Fort, and A. Boudaoud. Dynamical phenomena: Walking and orbiting droplets. *Nature*, 437(7056):208, 2005.

[24] T. Cristea-Platon, P. J. Sáenz, and J. W. M. Bush. Walking droplets in a circular corral: Quantisation and chaos. *Chaos: An Interdisciplinary Journal of Nonlinear Science*, 28(096116), 2018.

[25] M. F. Crommie, C. P. Lutz, and D. M. Eigler. Confinement of Electrons to Quantum Corrals on a Metal Surface. *Science*, 262(5131):218–220, 1993.

[26] M. F. Crommie, C. P. Lutz, and D. M. Eigler. Imaging standing waves in a two-dimensional electron gas. *Nature*, 363(6429):524–527, 1993.

[27] M. F. Crommie, C. P. Lutz, D. M. Eigler, and E. J. Heller. Quantum corral. *Physica D: Nonlinear Phenomena*, 83(1-3):98–108, 1995.

[28] M. F. Crommie, C. P. Lutz, D. M. Eigler, and E. J. Heller. Quantum interference in 2d atomic-scale structures. *Surface Science*, 361-362:864–869, 1996.

[29] A. P. Damiano, P.-T. Brun, D. M. Harris, C. A. Galeano-Rios, and J. W.M. Bush. Surface topography measurements of the bouncing droplet experiment. *Experiments in Fluids*, 57(10), 2016.

[30] O. F. de Alcantara Bonfim, J. Florencio, and F. C. Sá Barreto. Chaotic dynamics in billiards using bohm's quantum mechanics. *Phys. Rev. E*, 58(3), 1998.

[31] L. de Broglie. *Recherches sur la théorie des quanta ("Research on Quantum Theory").* PhD thesis, University of Paris, 1924.

[32] L. de Broglie. Interpretation of quantum mechanics by the double solution theory. *Ann. Fond. Louis Broglie*, 12:1–23, 1987.

[33] F. Dias, A. I. Dyachenko, and V. E. Zakharov. Theory of weakly damped free-surface flows: A new formulation based on potential flow solutions. *Phys. Rev. A*, 372:1297–1302, 2008.

[34] S. Douady. Experimental study of the Faraday instability. *Journal of Fluid Mechanics*, 221(5):383–409, 1990.

[35] M. Durey. *Doctoral Thesis.* PhD thesis, University of Bath, 2018.

[36] M. Durey and P. A. Milewski. Faraday wave-droplet dynamics: discrete-time analysis. *Journal of Fluid Mechanics*, 821:296–329, 2017.

[37] M. Durey, P. A. Milewski, and J. W. M. Bush. Dynamics, emergent statistics and the mean-pilot-wave potential of walking droplets. *Chaos: An Interdisciplinary Journal of Nonlinear Science*, 28(096108), 2018.

[38] A. Eddi, J. Moukhtar, S. Perrard, E. Fort, and Y. Couder. Level splitting at macroscopic scale. *Phys. Rev. Lett.*, 108(26):264503, 2012.

[39] A. Eddi, E. Sultan, J. Moukhtar, E. Fort, M. Rossi, and Y. Couder. Information stored in Faraday waves: The origin of a path memory. *Journal of Fluid Mechanics*, 674:433–463, 2011.

[40] D. M. Eigler and E. K. Schweizer. Positioning single atoms with a scanning tunnelling microscope. *Nature*, 344:524–526, 1990.

[41] A. Einstein, B. Podolsky, and N. Rosen. Can quantum-mechanical description of physical reality be considered complete? *Physical Review*, 47(10):777–780, 1935.

[42] H. Everett. Relative state formulation of quantum mechanics. *Rev. Mod. Phys.*, 29:454–462, 1957.

[43] M. Faraday. On a peculiar class of acoustical figures; and on certain forms assumed by groups of particles upon vibrating elastic surfaces. *Philosophical Transactions of the Royal Society of London*, 121:299–340, 1831.

[44] L. M. Faria. A model for faraday pilot waves over variable topography. *Journal of Fluid Mechanics*, 811:51–66, 2017.

[45] D. Farmer. Spectral broadening of period-doubling bifurcation sequences. *Phys. Rev. Lett.*, 47:179–182, 1981.

[46] D. Farmer, J. Crutchfield, H. Froehling, N. Packard, and R. Shaw. Power spectra and mixing properties of strange attractors. *Annals of the New York Academy of Sciences*, 357(1):453–471, 1980.

[47] G. A. Fiete and E. J. Heller. Colloquium: Theory of quantum corrals and quantum mirages. *Reviews of Modern Physics*, 75(3):933–948, 2003.

[48] G. A. Fiete, J. S. Hersch, E. J. Heller, H. C. Manoharan, C. P. Lutz, and D. M. Eigler. Scattering theory of kondo mirages and observation of single kondo atom phase shift. *Phys. Rev. Lett.*, 86(2392), 2001.

[49] E. Fort, A. Eddi, A. Boudaoud, J. Moukhtar, and Y. Couder. Path-memory induced quantization of classical orbits. *PNAS*, 107(41):17515–17520, 2010.

[50] J. Friedel. Electronic structure of primary solid solutions in metlas. *Advances in Physics*, 3(12):446–507, 1954.

[51] J. Friedel. Metallic alloys. *Del Nuovo Cimento*, 7(Suppl 2)(287), 1958.

[52] T. Gilet. Dynamics and statistics of wave-particle interactions in a confined geometry. *Physical Review E - Statistical, Nonlinear, and Soft Matter Physics*, 90(5), 2014.

[53] T. Gilet. Quantumlike statistics of deterministic wave-particle interactions in a circular cavity. *Physical Review E*, 93(4), 2016.

[54] B. J. Gluckman, C. B. Arnold, and J. P. Gollub. Statistical studies of chaotic wave patterns. *Physical Review E*, 51(2):1128–1147, 1995.

[55] H. Goldstein, C. P. Poole, and J. L. Safko. *Classical Mechanics.* Pearson, 3 edition, 2001.

[56] D. J. Griffiths and D. F. Schroeter. *Introduction to Quantum Mechanics.* Cambridge University Press, 3 edition, 2018.

[57] J. C. Gutierrez-Vega, R. M. Rodriguez-Dagnino, M. A. Meneses-Nava, and S. Chavez-Cerda. Mathieu functions, a visual approach. *Am. J. Phys.*, 71:233–242, 2003.

[58] M. C. Gutzwiller. *Chaos in Classical and Quantum Mechanics.* Springer, 1991.

[59] J. Hadamard. Les surfaces à courbures opposéees et leurs lignes géodesiques. *J. Mathématiques*, 4(5):27–73, 1898.

[60] D. M. Harris, P.-T. Brun, A. Damiano, L. M. Faria, and J. W. M. Bush. The interaction of a walking droplet and a submerged pillar: From scattering to the logarithmic spiral. *Chaos*, 28(096105), 2018.

[61] D. M. Harris and J. W. M. Bush. The pilot-wave dynamics of walking droplets. *Phys. Fluids*, 25(091112), 2013.

[62] D. M. Harris and J. W. M. Bush. Droplets walking in a rotating frame: from quantized orbits to multimodal statistics. *J. Fluid Mech.*, 739:444–464, 2014.

[63] D. M. Harris and J. W. M. Bush. Generating uniaxial vibration with an electrodynamic shaker and external air bearing. *Journal of Sound and Vibration*, 334:255–269, 2015.

[64] D. M. Harris, T. Liu, and J. W. M. Bush. A low-cost, precise piezoelectric droplet-on-demand generator. *Experiments in Fluids*, 56(4), 2015.

[65] D. M. Harris, J. Moukhtar, E. Fort, Y. Couder, and J. W. M. Bush. Wavelike statistics from pilot-wave dynamics in a circular corral. *Physical Review E - Statistical, Nonlinear, and Soft Matter Physics*, 88(1), 2013.

[66] Y. Hasegawa and P. Avouris. Direct observation of standing wave formation at surface steps using scanning tunneling spectroscopy. *Phys. Rev. Lett.*, 71(7):1071–1074, 1993.

[67] E. J. Heller. Bound-state eigenfunctions of classically chaotic hamiltonian systems: Scars of periodic orbits. *Physical Review Letters*, 53(16):1515–1518, 1984.

[68] E. J. Heller. Quantum chaos for real. *Nature*, 380:583–584, 1994.

[69] E. J. Heller, M. F. Crommie, C. P. Lutz, and D. Eigler. Mesoscopic systems and quantum corrals. *AIP Conference Proceedings*, 360:3, 1995.

[70] D. M. Henderson and J. W. Miles. Single-mode faraday waves in small cylinders. *Journal of Fluid Mechanics*, 213:95–109, 1990.

[71] D. M. Henderson and J. W. Miles. Faraday waves in 2:1 internal resonance. *Journal of Fluid Mechanics*, 222:429–470, 1991.

[72] J. Hogan, A. R. Krauskopf, M. di Bernando, R. Eddie Wilson, H. M. Osinga, M. E. Homer, and A. R. Champneys, editors. *Nonlinear Dynamics and Chaos: Where do we go from here?* CRC Press, 2002.

[73] P. R. Holland. *The Quantum Theory of Motion: An Account of the de Broglie-Bohm Casual Interpretation of Quantum Mechanics.* Cambridge University Press, 1995.

[74] M. Imada, A. Fujimori, and Y. Tokura. Metal-insulator transitions. *Rev. Mod. Phys.*, 70(4):1039–1263, 1998.

[75] J. D. Jackson. *Classical Electrodynamics.* Wiley, 3 edition, 1998.

[76] W. Jones and N. H. March. *Theoretical Solid State Physics, Vol 1 and 2.* Dover Publications, 1985.

[77] K. Kanisawa, M. J. Butcher, H. Yamaguchi, and Y. Hirayama. Imaging of friedel oscillation patterns of two-dimensionally accumulated electrons at epitaxially grown inas(111)a surfaces. *Phys. Rev. Lett.*, 86(15):3384–3387, 2001.

[78] J. Kondo. Resistance minimum in dilute magnetic alloys. *Prog. Theor. Phys.*, 32(37), 1964.

[79] V. V. Kozlov and D. V. Treshchĕv. *Billiards: A Genetic Introduction to the Dynamics of Systems with Impacts.* American Mathematical Society, 1991.

[80] K. Kumar. Linear Theory of Faraday Instability in Viscous Liquids. *Proceedings of the Royal Society A: Mathematical, Physical and Engineering Sciences*, 452(1948):1113–1126, 1996.

[81] K. M. Kurianski, A. U. Oza, and J. W. M. Bush. Simulations of pilot-wave dynamics in a simple harmonic potential. *Physical Review Fluids*, 2(11), 2017.

[82] M. Labousse, A. U. Oza, S. Perrard, and J. W. M. Bush. Pilot-wave dynamics in a harmonic potential: Quantization and stability of circular orbits. *Physical Review E*, 93(3), 2016.

[83] M. Labousse, S. Perrard, Y. Couder, and E. Fort. Build-up of macroscopic eigenstates in a memory- based constrained system. *New J. Phys.*, 16, 2014.

[84] E. N. Lorenz. Predictability: Does the flap of a butterfly's wings in brazil set off a tornado in texas? *American Association for the Advancement of Science*, 1972.

[85] E. Madelung. Eine anschauliche deutung der gleichung von schrödinge. *Naturwissenschaften*, 14(45):1004–1004, 1926.

[86] E. Madelung. Quantentheorie in hydrodynamischer form. *Z. Phys.*, 40(3-4):322–326, 1927.

[87] H. C. Manoharan, C. P. Lutz, and D. M. Eigler. Quantum mirages formed by coherent projection of electronic structure. *Nature*, 403(6769):512–515, 2000.

[88] J. Miles. Parametrically excited standing edge waves. *Journal of Fluid Mechanics*, 214:43–57, 1990.

[89] P. A. Milewski, C. A. Galeano-Rios, A. Nachbin, and J. W. M. Bush. Faraday pilot-wave dynamics: modelling and computation. *Journal of Fluid Mechanics*, 778:361–388, 2015.

[90] P. W. Milonni and J. H. Eberly. *Laser Phsycis.* Wiley, 2010.

[91] F. Moisy, M. Rabaud, and K. Salsac. A synthetic schlieren method for the measurement of the topography of a liquid interface. *Experiments in Fluids*, 46(6):1021–1036, 2009.

[92] J. Moláček and J. W. M. Bush. Drops bouncing on a vibrating bath. *Journal of Fluid Mechanics*, 727:582–611, 2013.

[93] J. Moláček and J. W. M. Bush. Drops walking on a vibrating bath: Towards a hydrodynamic pilot-wave theory. *Journal of Fluid Mechanics*, 727:612–647, 2013.

[94] C. R. Moon., C. P. Lut., and H. C. Manoharan. Single-atom gating of quantum-state superpositions. *Nature Physics*, 4(6):454–458, 2008.

[95] N. F. Mott. Metal-insulator transitions. *Rev. Mod. Phys.*, 40(4):677–683, 1968.

[96] V. V. Nesvizhevsky, A. Y. Voronin, R. Cubitt, and K. V. Protasov. Neutron whispering gallery. *Nature Physics*, 6:114–117, 2010.

[97] S. Newhouse, D. Ruelle, and F. Takens. Occurrence of strange axioma attractors near quasi periodic flows ont m ,mâ‰§3. *Communications in Mathematical Physics*, 64(1):35–40, 1978.

[98] R. G. Newton. *Scattering Theory of Waves and Particles.* Springer-Verlag New York, 2 edition, 1982.

[99] M. Nielsen and I. Chuang. *Quantum Computation and Quantum Information.* Cambridge University Press, 10 edition, 2011.

[100] A. U. Oza, D. M. Harris, R. R. Rosales, and J. W. M. Bush. Pilot-wave dynamics in a rotating frame: on the emergence of orbital quantization. *Journal of Fluid Mechanics*, 744:404–429, 2014.

[101] A. U. Oza, R. R. Rosales, and J. W. M. Bush. A trajectory equation for walking droplets: hydrodynamic pilot-wave theory. *Journal of Fluid Mechanics*, 737:552–570, 2013.

[102] A. U. Oza, Ø. Wind-Willassen, D. M. Harris, R. R. Rosales, and J. W. M. Bush. Pilot-wave dynamics in a rotating frame: Exotic orbits. *Phys. Fluids*, 26(082101), 2014.

[103] S. Perrard, M. Labousse, E. Fort, and Y. Couder. Chaos driven by interfering memory. *Physical Review Letters*, 113(10):104101, 2014.

[104] S. Perrard, M. Labousse, M. Miskin, E. Fort, and Y. Couder. Self-organization into quantized eigenstates of a classical wave-driven particle. *Nature Communications*, 5:3219, 2014.

[105] P. Pierański. Jumping particle model. period doubling cascade in an experimental system. *J. Phys. France*, 44(5):573–578, 1983.

[106] J. H. Poincaré. Sur le problème des trois corps et les équations de la dynamique. divergence des séries de m. lindstedt. *Acta Mathematica*, 13(1-2):1–270, 1890.

[107] S. Protière, A. Boudaoud, and Y. Couder. Particle-wave association on a fluid interface. *Journal of Fluid Mechanics*, 554:85–108, 2006.

[108] G. Pucci, D. M. Harris, L. M. Faria, and J. W. M. Bush. Walking droplets interacting with single and double slits. *Journal of Fluid Mechanics*, 835:1136–1156, 2018.

[109] G. Pucci, P. J. Sáenz, L. M. Faria, and J. W. M. Bush. Non-specular reflection of walking droplets. *Journal of Fluid Mechanics*, 804(R3), 2016.

[110] A. Rahman and D. Blackmore. Neimark-sacker bifurcations and evidence of chaos in a discrete dynamical model of walkers. *Chaos, Solitons & Fractals*, 91(s):339–349, 2016.

[111] G. Reecht, H. Bulou, F. Scheurer, V. Speisser, B. Carrière, F. Mathevet, and G. Schull. Oligothiophene nanorings as electron resonators for whispering gallery modes. *Phys. Rev. Lett.*, 110(056802), 2013.

[112] R. W. Robinett. *Quantum Mechanics: classical results, modern systems, and visualized examples.* Oxford University Press, 2005.

[113] D. Ruelle and F. Takens. On the nature of turbulence. *Communications in Mathematical Physics*, 20(3):167–192s, 1971.

[114] P. J. Sáenz, T. Cristea-Platon, and J. W. M. Bush. Statistical projection effects in a hydrodynamic pilot-wave system. *Nature Physics*, 2017.

[115] P. J. Sáenz, T. Cristea-Platon, and J. W. M. Bush. Localized hydrodynamic pilot-wave statistics around a defect. *In review*, 2019.

[116] E. Schrödinger. An undulatory theory of the mechanics of atoms and molecules. *Physical Review*, 28(6):1049–1070, 1926.

[117] E. Schrödinger. Die gegenwärtige situation in der quantenmechanik. *Naturwissenschaften*, 23(48):807–812, 1935.

[118] D. V. Schroeder. *An Introduction to Thermal Physics.* Pearson, 1 edition, 1999.

[119] H. G. Schuster. *Deterministic Chaos.* Physik-Verlag Weinheim, 1984.

[120] B. Schutz. *Gravity from the Ground Up.* Cambridge University Press, 1 edition, 2004.

[121] D. Shirokoff. Bouncing droplets on a billiard table. *Chaos*, 23:013115, 2013.

[122] S. H. Strogatz. *Nonlinear dynamics and Chaos.* Westview Press, 2014.

[123] N. Sungar, L. D. Tambasco, G. Pucci, P. J. Sáenz, and J. W. M. Bush. Hydrodynamic analog of particle trapping with the talbot effect. *Phys. Rev. Fluids*, 2:103602, 2017.

[124] L. D. Tambasco and J. W. M. Bush. Exploring orbital dynamics and trapping with a generalized pilot-wave framework. *Chaos: An Interdisciplinary Journal of Nonlinear Science*, 28(096115), 2018.

[125] L. D. Tambasco, D. M. Harris, A. U. Oza, R. R. Rosales, and J. W. M. Bush. The onset of chaos in orbital pilot-wave dynamics. *Chaos: An Interdisciplinary Journal of Nonlinear Science*, 26(10):103107, 2016.

[126] L. D. Tambasco, J. J. Pilgram, and John W. M. Bush. Bouncing droplet dynamics above the faraday threshold. *Chaos: An Interdisciplinary Journal of Nonlinear Science*, 28(096107), 2018.

[127] S. E. Turton. Private communication, 2019.

[128] T. Vialar. *Handbook of Mathematics.* Books on Demand, 2015.

[129] V. Volterra. L'applicazione del calcolo ai fenomeni di eredità. *Opere Matematiche*, 3:554–568, 1913.

[130] R. M. Wald. *General Relativity.* University of Chicago Press, 1 edition, 1984.

[131] E. Wigner and H. Margenau. Remarks on the mind body question, in symmetries and reflections, scientific essays. *Am. J. Phys.*, 35(12):1169–1170, 1967.

[132] Ø. Wind-Willassen, J. Moláček, D. M. Harris, and J. W. M. Bush. Exotic states of bouncing and walking droplets. *Physics of Fluids*, 25(8):082002, 2013.